Ultraschnelle Magnetisierungsdynamik ferromagnetischer Schichtsysteme

Dissertation

zur Erlangung des Grades eines
Doktors der Naturwissenschaften
(Dr. rer. nat.)

am Fachbereich Physik
der Freien Universität Berlin

vorgelegt von
Dominic Lawrenz

Berlin, 2024

Erstgutachter:	Prof. Dr. Martin Weinelt
Zweitgutachter:	Prof. Dr. Tobias Kampfrath
Tag der Disputation:	11.10.2024

Contents

Chapter 1

Introduction

When Beaurepaire *et al.* observed the ultrafast demagnetization of nickel in 1996 [1], their discovery laid the foundation of the research field of femtomagnetism. That the microscopic mechanisms that allowed the ultrafast transfer of angular momenta were unclear, showed that our understanding of magnetism was fundamentally lacking. And that, through understanding ultrafast magnetization dynamics, we could be able to expand our knowledge of magnetism as a whole.
Chapter 2 gives an introduction into some of the insights that the magnetism community has gained so far. Before we can contribute to these insights, we will first explore the experimental techniques that are used in this work in Ch. 3.

Apart from Ni, as Beaurepaire investigated it, gadolinium is a suitable system for studies. Because of it's half filled $4f$ shell, it possesses a large magnetic moment per atom. And because the $4f$ electrons are localized to their parent atom, interactions are sparse and Gd can be viewed as a Heisenberg magnet, where the magnetic moments are located at fixed positions. But research has shown that the situation is not quite as simple. A small part of the magnetic moments of Gd atoms is carried by the itinerant $5d6s$ electrons, which are spin polarized by the $4f$s and can interact amongst each other, leading to an indirect Ruderman-Kittel-Kasuya-Yosida (RKKY) interaction of the $4f$ electrons.
In time-resolved ARPES experiments, these $5d6s$ electrons exhibited an ultrafast change of their exchange splitting on a timescale of 0.8 ps. The magnetic linear dichroism of the localized 4f electrons, however reacted only on a timescale of 14 ps to the initial stimulus [2]. These distinct dynamics are already remarkable, because the $5d6s$ and $4f$ electrons have a rather strong exchange interaction of 130 meV [3]. To add to the puzzle, time resolved X-ray magnetic circular dichroism (XMCD) experiments in reflection revealed that the 4f electrons can show both a fast and a slow time constant of demagnetization. That means the $4f$ electrons exhibit a footprint of the $5d6s$ dynamics, contrary to the ARPES result. In Ch. 4 we will unravel what makes the difference in these two experiments and present an explanation for the puzzling observations.

The fundamental understanding of magnetism is one reason to investigate

magnetization dynamics. The technological potential of femtomagnetism is another one. Magnetic materials are of crucial importance to modern information technology. If it is possible to quench the magnetization of a material with nothing more than a laser pulse, are other optical manipulations possible as well? Like switching the magnetization of a material in a controlled way. This process is called all-optical switching (AOS) and has been thought about already in 2003 by Gomez-Abal *et al.* [4]. In 2007 Stanciu *et al.* could indeed demonstrate AOS in ferrimagnetic GdFeCo alloys [5]. Since then there have been many follow-up investigations both theoretical and experimental. One promising approach is the growth of synthetic ferrimagnets in the form of antiferromagnetically coupled bilayers. A pioneering work was done by Lalieu *et al.* in 2017 [6], who show that the contrast in the magneto-optical Kerr effect (MOKE) of a Co/Gd bilayer can be switched with an IR laser pulse. The fact that this switching is mostly independent of the ratio of the two magnetic species shows that synthetic ferrimagnets are different from ferrimagnetic alloys. In following works, the group laid a theoretical foundation to explain their findings [7, 8]. But the microscopic processes are still debatable and the MOKE technique only provides a measure of the overall magnetization, with a larger sensitivity for the transition metal component. Element specific information is lost in that setup.
Radu *et al.* [9] have shown in their element-specific XMCD experiments that the different magnetization dynamics of Fe and Gd are the reason for AOS in GdFeCo alloys. Thus it seems imperative to undertake an element-specific investigation of synthetic ferrimagnets to gain a more detailed understanding of the magnetization dynamics in these systems. We have applied XMCD in reflection to the synthetic ferrimagnet Fe/Gd. Our findings are detailed in Ch. 6.

The experiments by Lalieu *et al.* [6] where performed at room temperature, where Gd is only magnetized due to its proximity to Co. In the current work we have expanded the temperature window down to 100 K and find that another effect is of crucial importance when dealing with synthetic ferrimagnets: the so called twisted state. It was theoretically proposed by Camley and Tilley [10, 11] and describes a magnetic structure akin to a Bloch domain wall in both layers, if an external magnetic field is applied. Since this is the case in our experimental setup, we have characterized the bilayer structure in a static XMCD setup to support our analysis of the magnetization dynamics. Both the magnetic hysteresis as well as the results of a magnetic depth profiling through X-ray resonant magnetic reflectivity (XRMR) are presented in Ch. 5 and clearly show that the Fe/Gd bilayer is in a twisted state over a large temperature range.

Chapter 2

Fundamentals of magnetic switching

In this first chapter we will discuss some fundamental concepts that are necessary for the further understanding of the work at hand. At first we will look into the transient dynamics of magnets and how the responses of magnetic systems to ultrafast stimuli can be understood in Sec. 2.1. We will look into the magnetization dynamics of both Fe and Gd, because both Gd and Fe/Gd bilayers are at the center of this work. Especially the latter combination warrants further preparation. In Sec. 2.2, we will present previous works on the magnetic ground state of layered Fe/Gd systems and learn about the twisted magnetic ground state of that system, which will prove very useful for our later understanding.
The current work is inspired by the fact that Fe and Gd have an antiferromagnetic exchange coupling. And because such systems have been shown to exhibit all-optical switching, a scientifically interesting and technologically promising phenomenon. We will therefore discuss all-optical switching in more detail in Sec. 2.3.

2.1 Ultrafast demagnetization

The macroscopic quantum phenomenon of magnetism has been known since antiquity. And understanding of the working principles of magnetism has lead to profound applications: Compasses[1], electromagnets (e.g. in motors and generators), magnetic data storages and so on and so forth. The modern age of highly technologized societies is indeed unthinkable without an advanced understanding of the fundamental principles of magnets and a mastery in manufacturing them with diverse shapes and properties.
Still a complete and undisputed picture of the underlying physics has not been agreed upon in the scientific community and the technological potential of magnetic phenomena has most likely not been realized.
Numerous experimental methods and phenomena can be employed to investigate magnetic materials. Among those are the magneto-optic Kerr effect (MOKE)

[1]The first recorded compass was already used 100 a.d. in China. [12]

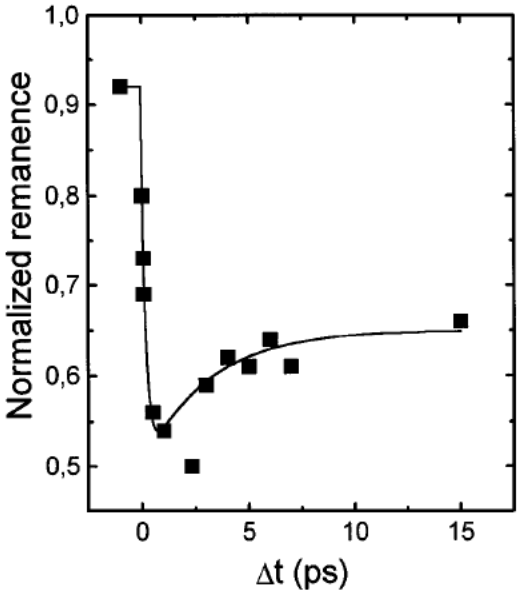

Figure 2.1: *Magnetization dynamics of the Ni film investigated by Beaurepaire et al. [1]. The magnetization is taken from the remanence of the magnetic hysteresis.*

and Faraday effect [13, 14], spin-resolved photoemission spectroscopy [15–18], magnetic linear dichroism (MLD) [2], X-ray circular magnetic dichroism (XMCD) [19, 20], neutron scattering [21] and second-harmonic generation (SHG) [22]. All of these and more methods have been used to study the equilibrium properties of magnetic materials. The advent of ultrafast laser sources in the 1990s however has opened a completely new field of research that constitutes one of the modern frontiers in the field: ultrafast magnetization dynamics or femto magnetism.

The ground breaking work of Beaurepaire *et al.* [1] set the stage for this active field. In their MOKE experiments they employed a 60 fs laser pulse to pump a 20 nm Ni film and observed a drop of the magnetization within the first picosecond. Figure 2.1 shows the dynamics of the magnetic remanence which they recorded. This observation was both a novelty and a challenge, as will be explained shortly. What the discovery means in the larger technological picture is the promise of drastically reduced response times (i.e. increased rate of data manipulation[2]) and energy consumption (cf. Sec. 2.3).

But why did the result by Beaurepaire *et al.* cause such an uproar in the relevant scientific community?
The basic microscopic proceeding of the experiment is agreed upon well enough: The laser pulse, in Beaurepaire's case containing 2 eV photons, is absorbed mainly by electrons close to the Fermi energy in the first step. The dominant interaction takes place between the electric field of the pulse and the electrons.
In the second step the hot electrons undergo scattering processes amongst themselves, with lattice phonons and magnons. Due to angular momentum conservation, the overall magnetization can only decrease if the magnetic moment of the electronic

[2]A classical hard drive writes data by applying a magnetic field pulse. The speed is determined mainly by the velocity of domain wall motions on the order of nanoseconds.

system is transferred to somewhere else. Up to the experiments by Beaurepaire *et al.*, it seemed to be clear that the lattice serves as the angular-momentum sink and that the bottleneck of the demagnetization timescale was the electron-phonon interaction time on the order of several picoseconds [23][24].
The fast timescale observed by Beaurepaire opened the discussion and search for further mechanisms of angular-momentum transfer.

2.1.1 Angular-momentum transfer mechanisms via spins

The following two mechanisms are pathways for angular momentum dissipation. They are opposed in two ways. Firstly in their range: Elliott-Yafet spin flip scattering does not require the excited electrons to move away from the probing region and can thus be considered a local process. In a superdiffusive spin current, the electrons leave the probing region. And secondly in the involved angular momentum reservoirs: While Elliot-Yafet spin flip scattering involves a transfer between electronic and phononic reservoir, superdiffusive spin currents conserve the angular momentum in the electronic reservoir.

Elliott-Yafet spin flip scattering

This mechanism was described by Elliott [25] in 1954 and Yafet [26] in 1963. An electron changes it's spin by transferring it to a phonon in a scattering event, thereby emitting or absorbing the phonon.
Elliott-Yafet spin flip scattering was used as the transfer mechanism for angular momentum when Koopmans refined the phenomenological three-temperature model of Beaurepaire *et al.* [1] to the microscopic three-temperature model (M3TM) [27].

Superdiffusive spin currents

This mechanism was described by Battiato *et al.* as a theoretical explanation for ultrafast demagnetization in ferromagnets [28]. In the first step, the femtosecond laser pulse excites electrons from d states to sp-like states. This process is assumed to be spin conserving, which differentiates it from spin-flip processes. The direction of movement of the excited carriers is random, both initially and after each scattering event. We know from statistics that such a random walk may lead to directional movement. The mean free path of the electrons is characterized by the lifetime, the average time until scattering occurs.
The property that leads to demagnetization is the spin-dependence of the lifetime. A simple argument to explain this is the different density of states of majority and minority spin electrons. The larger number of unoccupied minority spin states as compared to majority spin states leads to a smaller lifetime of excited minority spin electrons. As a consequence, the majority spin electrons will move farther away from the pump region, which leads to demagnetization.
Exchange scattering, in which an electron in one spin channel relaxes by exciting

an electron in the opposite spin channel, leads to a partial equilibration of the lifetimes.
The full numerical treatment of the model by Battiato *et al.* successfully explained the magnetization dynamics of Ni.

2.1.2 Transition metal dynamics: Iron

While Ni was the first material in which ultrafast demagnetization was observed by Beaurepaire *et al.* [1], other transition metals were investigated soon after. We will focus on Fe, one of the components of GdFeCo alloy. We will see in Sec. 2.3 why this compound plays such an important role for this work.
The group of transition metals is filling up the 3d shell. For the purposes of our experiments, 3d electrons are itinerant, i.e. non-localized with an overlapping probability density between electrons of adjacent atomic sites. In the case of Fe the atomic electron configuration is $[Ar]3d^64s^2$. Since the 3d shell can hold 10 electrons, Fe has 4 unpaired spins and one additional electron, resulting in the maximum orbital angular momentum for the 3d shell of $L = 2$ for Fe atoms. In crystals we need to consider the formation of electronic energy bands and hybridization effects between the wave functions of different electronic orbitals. The resulting magnetic moment per atom in bulk Fe is about 2.2 μ_B [29] and is dominated by the spin magnetic moment, stemming from 3d electrons [30]. With a Curie temperature of $T_C = 1043$ K [31] the magnetization of Fe is extremely stable over most experimentally accessible temperature ranges.

The magnetization dynamics of Fe were investigated by Zheng, Strüber *et al.* in angle-resolved photoemission (ARPES) experiments. In these experiments it was shown that the magnetization is mostly decreased through spin mixing. This means the dominance of one spin character (majority or minority) in a spin-split band reduces due to an increase of the electron population with opposite spin in the same state. This is believed to be mostly caused by magnon emission.
Previous work by Gort *et al.* has shown that the spin dynamics are non-uniform across the band structure [32]. While electrons close to the Fermi energy exhibit a timescale of 60 fs, those 2 eV below react much more slowly within 450 fs.

2.1.3 Rare-earth dynamics: Gadolinium

In addition to the transition metal Fe, we are interested in the rare-earth metal Gd. It belongs to the lanthanide group, in which the 4f shell, which may hold 14 electrons, is being filled. For Gd the shell is exactly half filled and we get an orbital angular momentum of $L = 0$. This leads to a very weak spin-orbit coupling. Most of the magnetic moment of a Gd atom stems from the 7 unpaired $4f$ electrons (7 μ_B). In addition to this, a magnetic moment of 0.55 μ_B is induced in the 5d6s electrons via a strong intra-atomic exchange interaction with an exchange energy of $J_{5d,4f} = 130$ meV [3]. The total angular momentum is thus $7.55\mu_B$ [33]. The 4f

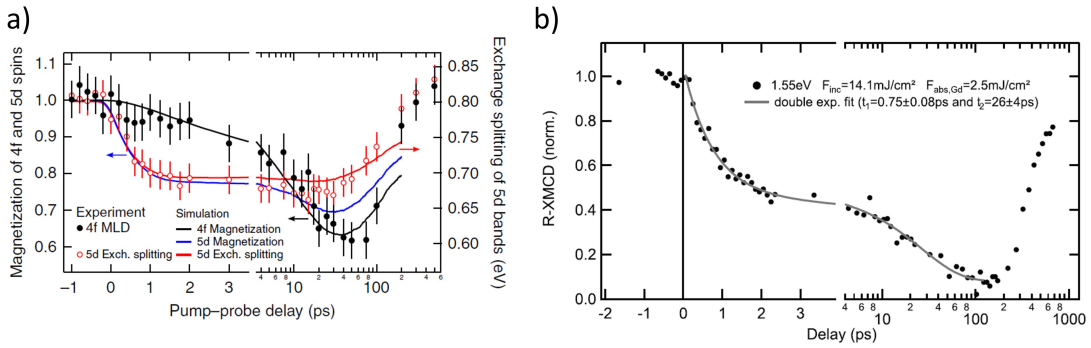

Figure 2.2: a) *ARPES data from Frietsch et al. [2]. The red dots show the dynamics of the 5d exchange splitting as a measure of the 5d magnetization. It is inferred from the binding energy of the state. The dynamics have a time constant of* 0.8 ps. *The black dots show the dynamics of the MLD contrast as a measure of the 4f magnetization. It exhibits a time constant of* 14 ps. ***b)*** *Normalized XMCD contrast recorded at the M_5 edge of Gd by Bobowski et al. [20]. A double exponential decay with an ultrafast time constant of* 0.75 ps *and a slower time constant of* 26 ps *is observed.*

electrons are highly localized to one lattice site. Inter-atomic exchange interaction between the 4f electrons is therefore negligible. Long range order is instead mediated via the $5d6s$ electrons by an indirect Ruderman-Kittel-Kasuya-Yosida [34][35][36] interaction (RKKY interaction). The exchange energy between nearest neighbors is $J_{5d,5d} = 5.9$ meV [2]. With a Curie temperature of $T_C = 293$ K [37], the Gd magnetization exhibits a strong temperature dependence compared to Fe. There have been numerous experiments concerning the laser-induced ultrafast dynamics of Gd [2, 20, 38, 39]. A key question that came up in these studies is whether the strong intra-atomic exchange between the $5d6s$ and $4f$ electrons leads to a synchronous response of both spin systems or is broken up on the ultrafast timescale. The latter notion is corroborated by ARPES results of Carley *et al.* and Frietsch *et al.* [2, 39]. The dynamics of the exchange splitting of the $5d6s$ state was observed in the change of binding energy of the occupied majority and minority spin bands. The magnetization of the $4f$ electrons was determined using magnetic linear dichroism. The results are shown in Fig. 2.2. Both electronic subsystems exhibited disparate dynamics on this ultrafast timescale, despite the intra-atomic exchange interaction between them. While the exchange splitting of the $5d6s$ electrons decayed with a fast time constant of 0.8 ps, the $4f$ magnetization showed a slow time constant of 14 ps.
In a MOKE experiment by Sultan *et al.* [38], the demagnetization time constant was found to be in the range of $0.5 - 0.8$ ps, depending on the pump fluence. This is in line with the aforementioned ARPES results and fits the interpretation of independent dynamics, because the MOKE signal is usually assumed to be mostly sensitive to the itinerant $5d6s$ electrons.

The notion of a synchronous response of $5d6s$ and $4f$ electrons appears to be supported by dynamic XMCD experiments conducted both by Wietstruk *et al.* on

a Y/Gd/Y/Al sample in transmission geometry [40], as well as by Bobowski *et al.* on an *in situ* grown Gd/W(110) sample in reflection geometry [20]. In both experiments it was observed that Gd demagnetizes with a fast and a slow timescale. This behavior could be well described by the phenomenological extended M3TM [27]. It is important to note that XMCD at the M-edges is sensitive to the $4f$ and not the $5d6s$ magnetization. The occurrence of a fast timescale seemed to indicate that the $5d6s$ electron dynamics were imprinted on the $4f$ dynamics quasi instantaneously, for the purposes of the experiment.
In Ch. 4 we will explore this conundrum further and attempt to solve it.

2.2 Transition metal/ rare-earth metal bilayers

In this work we investigate the combination of both Fe and Gd in the form of epitaxially grown bilayers. The composition of such bilayers is easily controlled by the thicknesses of the layers. In contrast to an alloyed system where a direct interaction between both species may take place all over the sample, it is restricted to the interface in a bilayer. This is a significant observation, which will become useful later on.
Fe and Gd exhibit a negative exchange constant, i.e. they couple antiferromagnetically. Since both elements have a significantly different Curie temperature, the net magnetization of a Fe/Gd bilayer is generally non-zero so that the film is a ferrimagnet instead of an antiferromagnet.

Bilayers of transition metal and rare-earth metal magnets have already been investigated in the 90's ([10, 11, 41–43]). To improve the signal to noise ratio these experiments made use of multilayers in which a unit cell of Fe/Gd was repeated multiple times. If such multilayers are put into an external magnetic field, two energy contributions compete with each other: The Zeeman energy of the magnetic moments in the external field and the exchange energy, which favors antiferromagnetic alignment between Fe and Gd moments at the interface and ferromagnetic alignment of magnetic moments within each layer. The former favors a ground state in which all moments are aligned in field direction. The latter favors a ground state in which Fe and Gd are antiparallel to each other. Both cannot be fulfilled at the same time. What is the ground state of such a system?

In 1987 R.E. Camley had already investigated thin Gd films on an Fe substrate using mean-field theory [41] and found a spin-flop state where both magnetizations twist towards the external field. He substantiated his findings in a second paper with D.R. Tilley [10] in which they attempted to give an answer to the above question. They calculated stable ground states of the layer resolved magnetization vectors as a function of temperature for layers with varying Fe and Gd thicknesses within the unit cell of a multilayer. To achieve this, Camley and Tilley used a combination of microscopic, macroscopic and Landau-Ginzburg approaches.

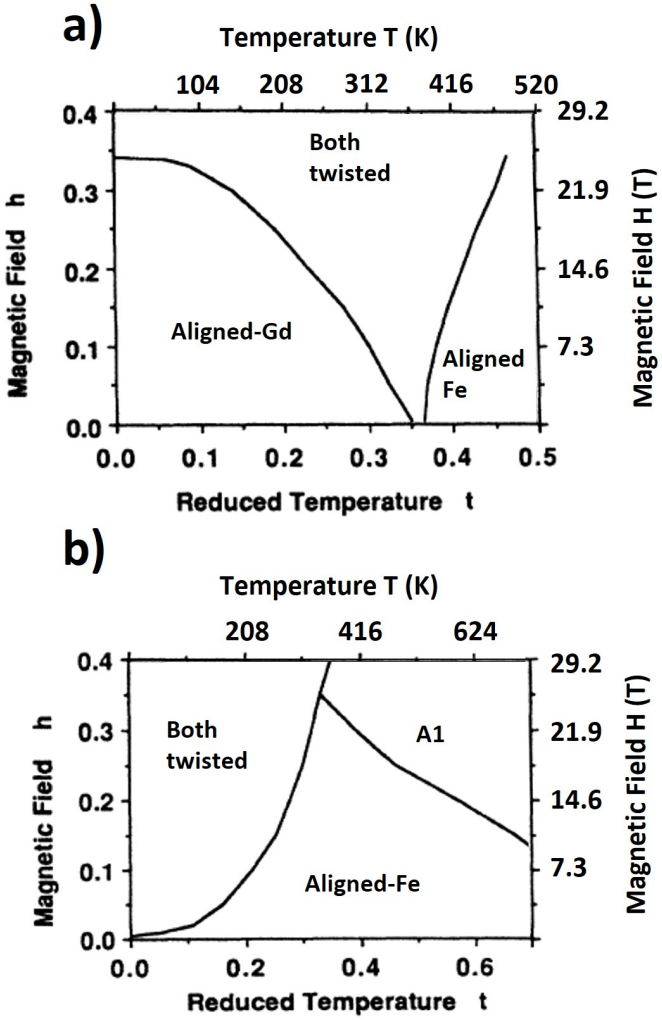

Figure 2.3: ***a)*** *Phase diagram of the magnetic ground state for a Fe/Gd superlattice with four Fe and four Gd layers in the unit cell.* ***b)*** *Phase diagram for a Fe/Gd superlattice with seven Fe layers and five Gd layers in the unit cell. The magnetic field and temperature in both graphs are given in reduced, dimensionless units in Ref. [10]. The values with units were added here using information given in Refs. [10, 11]. (figures taken from [10])*

The result of [10] is summarized in a phase diagram like those in Fig. 2.3. The authors identify 4 possible phases: the aligned Gd phase, the aligned Fe phase, the A1 phase and the twisted state.
The aligned phases correspond to states in which either of the elemental layers has a larger total magnetic moment than the other and dominates the Zeeman energy. The Zeeman energy of the entire film is still significantly smaller than the sum of all inter-atomic exchange energies of the film. Thus each layer is uniformly aligned and the two elemental species are aligned antiferromagnetically. Because of the temperature dependence of the average magnetic moment (as described by the Brillouin function), this balance changes with temperature. If the Gd layer is thin enough to possess an inferior total magnetic moment even at low temperatures,

there is no Gd-aligned phase. This is due to the relatively low Curie temperature of Gd and the resulting steep temperature dependence of it's magnetization within the investigated temperature window. Fe in comparison has a Curie temperature of $T_C = 1043$ K and does not significantly demagnetize in the temperature window we investigate.

The A1 phase can only be observed in multilayers. It is a result of the presence of Fe layers on both sides of each Gd layer. For certain combinations of temperature and magnetic field, the magnetic moments in the center of each Gd layer are influenced to the same extent by the exchange with neighboring moments and by the external field. They behave paramagnetically. In the current work we will consider films with only one layer of each species so that this phenomenon can be excluded.

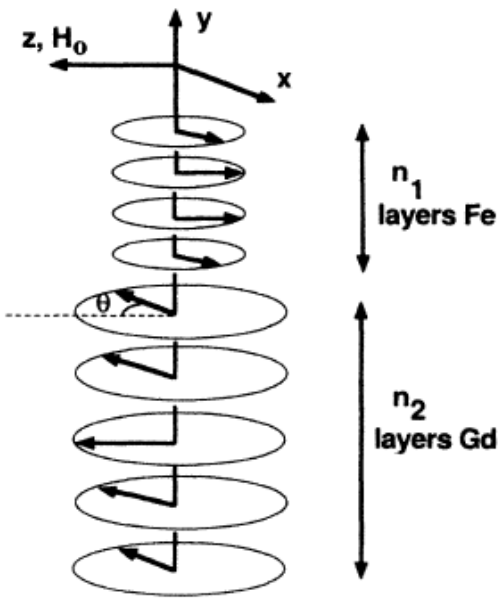

Figure 2.4: *Schematic illustration of the layer dependent magnetization of a unit cell of the superlattice. There are n_1 layers of Fe and n_2 layers of Gd. The angle of the magnetization vector changes as a function of distance from the Fe-Gd interface. Figure taken from [10].*

The most interesting phase for us to consider is the twisted state depicted in Fig. 2.4. Camley describes two scenarios of the twisted state in a follow-up paper [11]. In the first scenario, the magnetic field is strong enough that Zeeman and exchange energy are on the same order. We can see in Fig. 2.3 that considerable field strengths are necessary for this, which we cannot reach with the available magnets in our experiments. The second scenario takes place when the Zeeman contribution from both layers is almost equal, which is more feasible in our experimental setup. There is no clearly favored orientation relative to the external field. Camley describes the resulting structure as "similar to a spin-flop state" [11]. It is unclear, though,

what the microscopic configuration of magnetic moments is in that case so we will treat it on equal footing and apply the model presented by Camley and Tilley in Ref. [10].
In the twisted state, the magnetic moments of both layers will attempt to align to the field. As a result, for moderate field strengths both Fe and Gd moments can be found to align almost perpendicularly to the external field. The magnetic moments of Fe and Gd at the interface are assumed to align almost perfectly antiparallel to each other due to the strong antiferromagnetic exchange coupling. Every atomic step away from the interface, however, introduces a small angle. In this fashion the magnetic moments would align with the external field over a large enough distance from the interface. This is akin to a magnon, where a spin flip is distributed over many atomic distances, which reduces the total exchange energy that is paid for the spin flip. In the multilayer, that Camley and Tilley modeled, the presence of an interface on the other side of the layer tilts the orientation of the magnetic moments back. In addition, Camley and Tilley modeled a layer in which Fe and Gd are semi infinite and have only one interface. From this the distance over which turning to field-alignment occurs can be estimated as $4.3 - 8.5$ μm depending on the field strength. In Ref. [11] an estimate was made for the length scale of a twist by 180° using the formula

$$n_0 = \sqrt{z\pi J_i S_i / 2g\mu_B H_0} \tag{2.1}$$

for domain wall thicknesses. Here n_0 is the number of atomic layers, z is the number of nearest neighbors (8 for bcc Fe, 12 for hcp Gd), J_i, S_i are the exchange constant and spin quantum numbers for $i = Gd, Fe$ and H_0 is the external magnetic field. We will use $S_{Gd} = 7/2$ and $S_{Fe} = 2$ as well as $J_{Gd} = 5.9$ meV [2] and $J_{Fe} = 32.5$ meV [3]. By setting a field strength of 0.1 T and using the layer thicknesses 2.05 Å for Fe(110) and 2.9 Å for Gd(0001), we obtain a twist length of about 964 Å in Fe and 942 Å in Gd. These values hold at a temperature of 0 K. For higher temperatures, the effective spin S_{Gd} and S_{Fe} shrinks and the twist length reduces. Due to the large Curie temperature of Fe at 1043 K, this mostly concerns Gd.
For our finite bilayer the twisting is schematically shown in Fig. 2.5. In this picture, we neglect the influence of the interfaces between Gd and the W substrate, as well as between Fe and the Y capping layer (not shown), because both adjacent materials are paramagnetic. We cannot rule out that they have an influence on the magnetization in the vicinity of the interfaces, though.
All angles with the external field are in-plane rotations, as favored by the shape-anisotropy energy of thin films.

To put their results into perspective we note that the limits of the model lie in the microscopic parameters it assumes. Camley and Tilley use dimensionless parameters. We can therefore only consider the ratio $J_{Fe,Fe}/J_{Gd,Gd} = 6.5$ in Ref. [10] and $J_{Fe,Fe}/J_{Gd,Gd} = 28.2$ in Ref. [11] and compare it to more recent values. We can extract $J_{Fe,Fe}/J_{Gd,Gd} = 4.2$ from Wienholdt *et al.* [3][3], or use the value

[3]Albeit Wienholdt *et al.* modelled FeGd alloys in which rare earth atoms are only next nearest

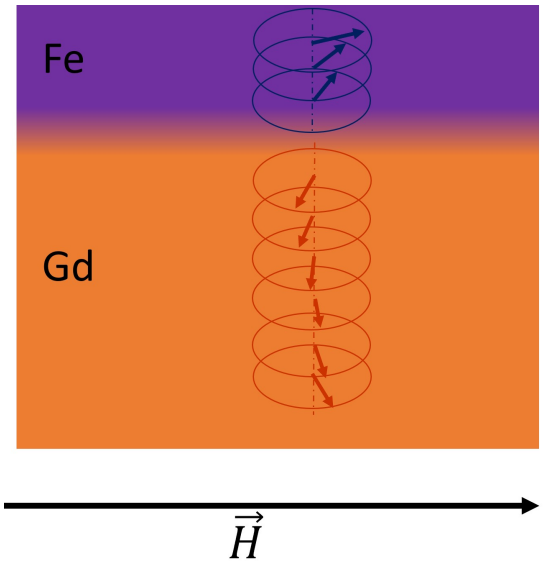

Figure 2.5: *Schematic illustration of the layer dependent magnetization of a finite bilayer of Fe and Gd close to the compensation temperature.*

$J_{Gd,Gd} = 5.9$ meV from Frietsch *et al.* [2] to similarly receive $J_{Fe,Fe}/J_{Gd,Gd} = 5.6$. The ratios all indicate that the inter-atomic exchange in the Fe layer is significantly stronger than that in the Gd layer. As a consequence we can expect a stronger tilting, and thus a smaller angle of the magnetization with the external magnetic field, in the Gd layer. The exchange parameter between Fe and Gd atoms $J_{Fe,Gd}$ only acts directly at the interface. Tilting is negligible over such small distances, i.e. Fe and Gd magnetic moments are antiparallel.
The numerical values of the exchange parameters are naturally relevant for the quantitative statements made by Camley and Tilley. The qualitative result of the twisted state, which we will see shortly, remains untouched, though. The prediction of the twisted state was corroborated by several authors that have made experimental observations, which they interpret explicitly with reference to Camley's and Tilley's work [42–45]. Others describe their findings in the very similar picture of a spin-flop state [46, 47], without refering to Camley and Tilley.

2.3 Magnetization switching

In the following, combinations of transition and rare earth metals will play a central role as well. But to place our work on Fe/Gd bilayers in this context, it is better to start by considering amorphous alloys.
Such compounds were already under investigation in the late 70s (see a survey by Buschow from 1977 [48]). In the case of Fe, Co and Gd the atoms couple antiferromagnetically. Because their atomic magnetic moments and Curie

neighbors to each other. They assume $J_{Gd,Gd} = 7.8$ meV.

temperatures are different, the magnetizations of the Fe and Gd sublattices generally do not compensate as in an antiferromagnet. Instead GdFeCo has a temperature dependent net magnetization. As we mentioned before such materials are called ferrimagnets.
The GdFeCo compound in particular has opened the experimental field of all-optical magnetization switching (AOS), i.e. changing the magnetization state of a material purely with photons. A key motivation for the study of this phenomenon is it's potential for data storage applications. To understand the groundbreaking potential it is helpful to first take a look at the switching procedure in state-of-the art data storage technology. Once we have done that we will explore AOS in more detail.

2.3.1 Switching with magnetic fields

A hard disk drive stores bits of information as magnetic domains with two possible magnetization directions to encode zero and one. Such domains exhibit sizes on the order of several 10 nm in each dimension.[4] The encoded information (i.e. the magnetization direction) is recognized by the difference in electric resistivity through the domain, caused by the giant magnetoresistance effect.
To change the state of a domain, the write head applies a magnetic field opposite to its magnetization direction. For sufficiently strong fields, the bit will switch.[5] The speed of this writing process is on the order of $0.1 - 1$ ns, limited by the angular momentum transfer rate between spins and lattice. We can convert this timescale to a frequency in line with the clock rates of modern CPUs on the 1 GHz scale. But if processor speeds increase, the CPU will eventually need to wait for the memory and read-write speeds become a bottleneck.

2.3.2 All-optical switching: Switching with photons

What do we mean by all-optical magnetization switching and how did the concept emerge?
After it was established that photons can reduce the magnetization of a system [1], the question arose whether they could manipulate it in other ways. Coming from magnetic field switching, we know that it is useful to turn the magnetization vector around to encode information in it. AOS does just that through the illumination with photons, without the influence of an external magnetic field.
Theoretical predictions of the possibility of AOS in semiconductors and insulators date back to Gomez-Abal *et al.* in 2003 and 2004 [4, 49]. They described an intricate switching mechanism including transitions between discrete energy levels

[4] https://www.computerhistory.org/storageengine/hdd-areal-density-reaches-1-terabit-sq-in/

[5] Note that this is a simplified picture. A more detailed discussion is found in [30]. There is also the method of heat-assisted magnetic recording (HAMR), where domains are first heated to lower the required field strength for switching. An implementation of HAMR from *Seagate* was due for commercial availability by the end of 2020.

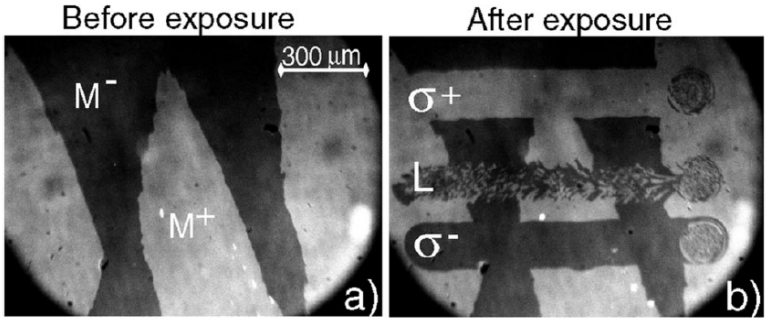

Figure 2.6: a) *Kerr microscopy image of a* $Gd_{22}Fe_{74.6}Co_{3.4}$ *sample with up (white) and down (black) oriented magnetic domains.* ***b)*** *Upon sweeping a laser with a fluence of about* 11.4 mJ/cm^2 *across the sample, polarization dependent results are found. For right-handed circular polarization, an up-domain forms, while left-handed circular polarization creates a down domain. Linear polarization leaves an area of small randomly oriented domains. The random orientation is also observed at the end of each sweep, irrespective of the polarization. Figure taken from [5].*

and a delicate dependency on the pump pulse length and excited state lifetime. This model has not found application in explaining experimental observations, however.

Helicity dependent switching

The first experimental observation of all-optical switching was made by Stanciu *et al.* in 2007 [5]. They investigated amorphous GdFeCo samples[6] by means of Kerr microscopy. The pump pulses had a wavelength in the near-infrared and were circularly polarized.
Figure 2.6 shows the resulting Kerr microscopy images. Stanciu *et al.* noted that the area which the pump beam had illuminated would either exhibit a reversed or unchanged magnetization with respect to the area that had not been illuminated, depending on the polarization direction of the pump beam. A linearly polarized pump beam, on the other hand, created areas of small randomly oriented domains, effectively destroying the long range magnetization.

The results were interpreted in two steps. Firstly, the pump beam heats up the sample close to the Curie temperature. Secondly, the circularly polarized pulse exerts an effective magnetic field via the inverse Faraday effect. For a fluence of 10 mJ/cm^2 a field strength of 20 T is expected. The field vector points parallel or antiparallel to the wave vector, depending on the light helicity.

A follow-up investigation by Vahaplar *et al.* [50] in 2009 combined a time-resolved

[6]The alloy investigated by Stanciu *et al.* has a typical constitution of $Gd_{22}Fe_{74.6}Co_{3.4}$. The other investigators mentioned in this chapter made use of only slightly deviating compositions.

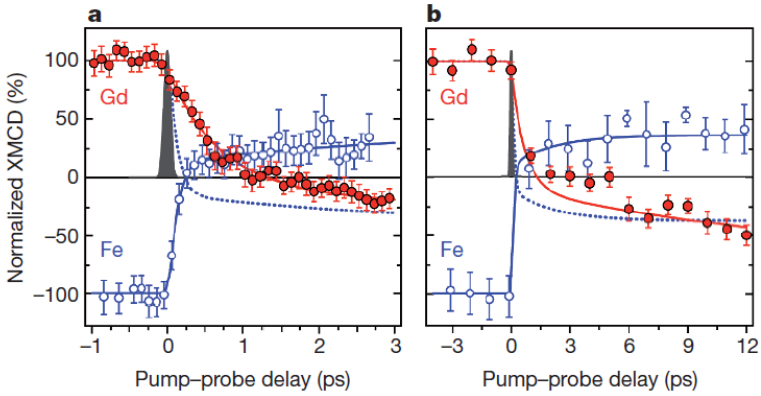

Figure 2.7: a) *Normalized dynamical XMCD signal of the Gd (red) and Fe (blue) sublattices. The sample was held at a temperature of* 83 K*. The laser pump pulse had an energy of* 1.55 eV*, a fluence of* 4.4 mJ/cm^2 *and a pulse duration of* 100 fs *as indicated by the grey Gaussian profile. The dashed blue line shows the Fe demagnetization plotted with opposite sign. We can clearly see the transient ferromagnetic state up to a delay of about* 1 ps*.* ***b)*** *The same results on a longer timescale. Figure taken from [9].*

magneto-optic Kerr effect (MOKE) experiment with theory on the basis of the Landau-Lifshitz-Gilbert (LLG) equation. Stanciu's interpretation of the underlying physics remains and is further corroborated by a phase diagram for the pulse parameters that may lead to AOS.

"Thermally" induced magnetic switching

The deterministic writing of magnetic domains through the helicity of light was seen as a major breakthrough. Until 2011, when Radu *et al.* revealed with element specific time-resolved XMCD experiments that the underlying mechanism was quite different [9]. Up to now we have not considered the sublattices of GdFeCo independently. Due to the small percentage of only 9.4% of Co, we can put the focus on Gd (25%) and Fe (65.6%). As mentioned before, the exchange coupling between Gd and Fe leads to an antiferromagnetic alignment. Because the magnetizations of the sublattices do not fully compensate, the alloy exhibits a net magnetization.

Let us focus on the magnetization dynamics of the sublattices shown in Fig. 2.7. We can see that both sublattices demagnetize due to the heating of the electronic system by the laser pulse. As in single elemental samples, the transition metal demagnetization occurs on a timescale of 100 fs, while the lanthanide demagnetization shows a time constant of 430 fs. This independent behavior is remarkable, as it runs counter to the earlier stated coupling between the chemical species, which are in close proximity on atomic length scales after all. It shows the distinctly non-equilibrium state that is reached on these timescales.

The second point of note is that the Fe magnetization crosses, rather than approaches, zero after 300 fs and grows in the opposite direction. This leads to a so called transient ferromagnetic-like state. After 1.5 ps the Gd magnetization likewise crosses zero, which completes the AOS.
What finally refuted the earlier interpretations of AOS by Stanciu *et al.* and Vahaplar *et al.* is the fact that Radu *et al.* used a linearly polarized pump pulse and could therefore exclude the inverse Faraday effect. In fact it was shown by Khorsand *et al.* in 2012, that the helicity dependence of these early observations is caused by circular magnetic dichroism [51]. There is a threshold pump intensity for all-optical switching. Depending on the magnetization direction, light of left or right circularity is absorbed with a higher probability. Within an intensity window around the threshold, the switching is only triggered by one helicity. Instead of the inverse Faraday effect, the main cause of AOS turned out to be simply heating of the electronic system [52]. The effect is sometimes abbreviated as TIMS (thermally-induced magnetic switching). It should be stressed that this wording can be misleading, because the sample is not being heated while in thermal equilibrium. It is in a highly non-equilibrium state, where initially only the electrons are excited.
From a technological point of view, the toggle switching nature of single-pulse AOS was seen as a setback, because the magnetic state of a domain after switching depends on the state before and the number of absorbed pulses, instead of purely on the light polarization.[7] It shall be noted that helicity dependent all-optical switching is possible, but requires multiple laser pulses. A recent study by Cheng *et al.* can be found in [54]. When we speak of AOS in the following, we will always refer to single-pulse all-optical toggle switching without helicity dependence.

In 2013 Graves *et al.* investigated the stoichometry of GdFeCo alloy in X-ray diffractometry [55]. If we compare the Gd and Fe maps in Fig. 2.8, we can see clusters of Gd that are depleted of Fe and vice versa. The Co map shows a much more homogeneous distribution. Such inhomogeneities may have important consequences for the dyamics of a GdFeCo sample, because the switching behavior is strongly dependent on Gd concentration [56]. Furthermore Graves *et al.* concluded, that a non-local transfer of spin angular momentum between Gd and Fe rich clusters may be a dominant process in AOS.

Avoiding inhomogeneities can exclude their overall effect on the magnetization dynamics of the ferrimagnet and also local variations of the dynamics. This motivates the study of layered systems.

Lalieu *et al.* investigated the first ferrimagnetic bilayers with the goal to observe AOS in MOKE [6]. Their functional bilayers consisted of Co with varying thickness and 3 nm of Gd. Indeed, all-optical switching occured in the same deterministic and repeatable manner as before in alloyed samples. This may not seem surprising at first, but further studies revealed that the new system is not equivalent to the

[7] This flaw can be overcome with clever pulse patterns, as presented by Hees *et al.* [53].

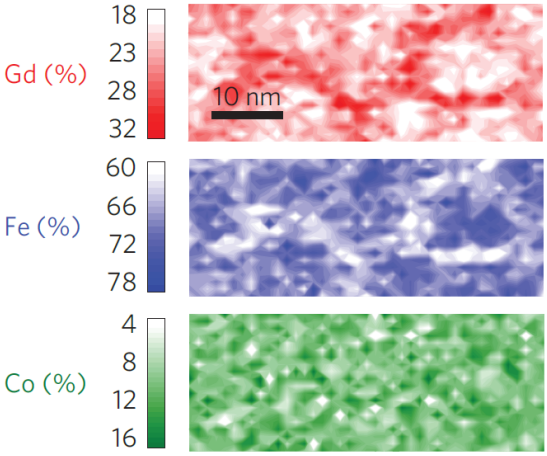

Figure 2.8: *Element-selective STEM-EDX measurements showing thrice the same sample region, tuned to different elements. We can clearly see enriched (darker) and depleted (lighter) regions for each element. The stoichiometry of the sample is inhomogeneous.*

alloy we considered before.

In Subsec. 2.3.3 we will go on to make a survey of the theoretical works that model single-pulse all-optical toggle switching for both amorphous alloys as well as synthetic ferrimagnets.

Technological potential

To close the circle of our initial discussion, we may ask how AOS can improve on the limitations that switching in storage devices faces? Each AOS experiment to date has made use of a pump-laser pulse in the near-infrared wavelength range. The diffraction limit thus allows for minimum spot (and thus bit) sizes of around 400 nm at most.[8] But there are attempts to focus laser beams further down with the help of lithographically patterned nano-antennas ([57], [58]). Another approach has been pioneered by Le Guyader *et al.* [59], who follow an aimed nanostructuring approach. The sample is engineered in such a way that interference and refraction effects focus the laser light on a specific spot on the nanoscale. These experiments show that while state-of-the-art AOS experiments do not have nanoscale resolution, it is still possible to achieve nanoscale control with AOS.
But there is another aspect to the miniaturization topic in which AOS shows clear advantages. As Evans *et al.* state [60], the field strength in magnetic field switching must overcome thermally driven back-switching.[9] This drives the necessary field strength higher with increasing bit density. In AOS the effective field is given by the exchange interaction between the species of the ferrimagnet, which is much stronger than inductive fields. This makes further miniaturization actually easier with AOS. As a sidenote, the production costs of magnetic write heads could be reduced if there is no necessity for magnetic transducers [61].

[8] Experimental spot sizes are typically on the order of 100 μm.
[9] The effect is called "thermal writability" and is more important than the "thermal stability" of the magnetic bits.

When we discussed the pioneering experiment by Beaurepaire *et al.* [1], we already noted the promise of increased data manipulation speeds. All-optical switching is indeed capable of turning the net magnetization around on a timescale of less than 1 ps [52], 2-3 orders of magnitude faster than a magnetic field.
The necessary pulse energy per unit area is on the order of 1 $\mathrm{mJ/cm^{-2}}$ [52].

Given a stable realization of nanoscale manipulation and an energy efficient way of generating the necessary pump pulses, we may conclude that AOS holds great potential for ultrafast data storage.

2.3.3 Theoretical models

All-optical switching has been treated in several theoretical works. There are two main approaches. On the one hand we find the Landau-Lifshitz-Gilbert (LLG) and Landau-Lifshitz-Bloch (LLB) equations. While the LLG equation only considers precessional motion of the magnetization vector, i.e. transversal relaxations, the LLB equation includes also length changes, i.e. longitudinal relaxations.
On the other hand we have the microscopic three temperature model (M3TM), which aims to describe the interaction between the electronic, phononic and spin subsystems in order to model magnetization dynamics.
Most experimental investigations of AOS are focused on the amorphous ferrimagnetic alloy GdFeCo, in which AOS was first encountered. This material was likewise the center of attention for theoretical modeling in the field. We will start there as well.
We will see that, while the main concepts found for AOS in alloys still hold in ferrimagnetic bilayers, there are some key differences.

As in the demagnetization of single elemental samples, we need to understand where and how the angular momentum in ferrimagnets is transferred upon excitation. An important distinction between ferromagnets and ferrimagnets is that we have two magnetic sublattices with opposing magnetization directions, similar to an antiferromagnet. This opens new relaxation channels for the angular momentum.

Switching in ferrimagnetic alloys

After the demonstration of distinct dynamics of the Fe and Gd sublattices in the GdFeCo alloy and the discovery that the effect was thermally driven by Radu *et al.* in 2011 [9], Mentink *et al.* presented a theoretical framework for the modelling of ultrafast spin dynamics in multisublattice magnets with rate equations on the basis of Onsager's relations in 2012 [62]. They differentiate between three temperature regimes, which are experimentally accessed on different timescales. Within $10 - 100$ fs after excitation, the electronic temperature T_e is increased beyond the critical temperature T_C of the sample, such that the thermal energy is much larger than the exchange energy between the sublattices. In this way,

both sublattices demagnetize independently. It is important to note that the excitation is any pulse-like stimulus that increases the electronic temperature, and not necessarily a laser pulse.
After several picoseconds, the electronic temperature has relaxed below the critical temperature of the sample. The exchange of magnetic moments between the sublattices becomes dominant and angular momentum conservation between the spin subsystems is obeyed. If the first sublattice magnetization is close to zero, it still receives magnetic moments from the second, more slowly demagnetizing sublattice and can thus remagnetize in the direction opposite to it's initial magnetization, if the sublattices couple antiferromagnetically.
The third temperature regime occurs around T_C. In this intermediate regime both exchange between the sublattices and angular momentum transfer to the crystal lattice are relevant. In antiferromagnetically coupled sublattices this leads to faster demagnetization compared to single elemental samples due to the exchange of magnetic moments.

Atxitia *et al.* [63] derived a Landau-Lifshitz-Bloch (LLB) equation to describe the dynamics of two-sublattice systems without the need to distinguish between temperature ranges. It combines atomistic spin simulations with a macrospin approach to model both longitudinal, i.e. changes of the length of the spin vector, and transversal, i.e. rotations of the spin vector, relaxations of the sublattice magnetizations. The theory was used to show a pathway for the angular momentum in the switching dynamics of transition-metal-rare-earth-metal compounds [64].
Three contributions are considered: A precession of the transition-metal magnetization around the exchange field of the rare-earth magnetization, a relaxation towards the rare-earth exchange field direction and a longitudinal relaxation. All three contributions act on the same timescale in this model.
In this model AOS is only possible due to a perpendicular component between the sublattice magnetizations, caused by thermal fluctuations, and the consequent possibility to apply a torque between them. Upon excitation the two magnetization vectors start precessing antiparallel around each other's mean direction. Angular momentum is exchanged between the sublattices, which enhances the precession. Together with the relaxation term, i.e. damping of the precessional motion, both magnetizations eventually arrive at the direction that the other had occupied prior to the excitation. This process may be called "precessional switching". The model does not, however, make statements about the microscopic processes that transfer angular momentum between the subsystems.

Schellekens *et al.* [65] formulated a model on the basis of the microscopic three-temperature model (M3TM), which was originally developed to model the ultrafast demagnetization of ferromagnets [27]. The M3TM started as a phenomenological description of the demagnetization dynamics of rare earth metals and considers the interaction of the three subsystems of electrons, phonons and spins. In [65] they make use of a second spin system to model the two sublattices. Notably Schellekens *et al.* make the assumption that electronic

scattering events are responsible for the transfer of angular momentum. Namely electron-phonon scattering, Elliott-Yafet spin-flip scattering (see Subsec. 2.1.1), and electron-electron scattering in which both electrons exchange their spin.

Wienholdt *et al.* [3] use the LLG equation to refine the previous works in so far as they make an explicit distinction between Gd 5d and 4f electrons. Similar to Mentink *et al.* the authors divide the processes into three timescales. On the timescale of the laser pulse, the dominating processes are electronic in nature. This leads to the known phenomenon of ultrafast demagnetization. The main carriers of the magnetic moment in Gd are the 4f electrons that lie 8 eV below the Fermi energy. They cannot be directly excited by the laser pulse in contrast to the Fe 3d electrons, which leads to faster dynamics for Fe. The excitation by the laser pulse is calculated in the two-temperature model as was done by Vahaplar *et al.* [50] in their study of helicity dependent AOS and first formulated by Beaurepaire *et al.* [1].
On the second timescale after ca. 1 ps we find the spin systems in nonequlibrium. The Fe spins are more strongly excited than the Gd spins. Due to the principle of maximization of entropy and conservation of angular momentum and energy, Wienholdt *et al.* argue that a dissipationless transfer of angular momentum and energy from the Fe to the Gd sublattice must occur. This leads to the transient ferromagnetic state that is observed in experiments and that is an important step for the final relaxation into a switched state. These calculations were performed with the Landau-Lifshitz-Gilbert equation of motion.
Finally on the timescale of several picoseconds, dissipation leads to a loss of angular momentum and energy in the spin system. This causes the relaxation back to a ferrimagnetic state, switched with respect to the initial state.

Local or non-local processes? We noted in the beginning that the transfer of angular momentum is crucial for our understanding of AOS. But we have also seen that only a few theoretical works make statements about which microscopic processes are responsible for that transfer. We can distinguish two ideas: local and non-local processes. The first one was already implicitly presented in the interpretation of the experiment by Radu *et al.* and more thoroughly explained in the paper by Schellekens and Koopmans [65]. In the form of electron-electron scattering they assume a local exchange interaction between neighboring Gd and Fe atoms in the alloy lattice.
Looking at the stoichometry study of GdFeCo alloy performed by Graves *et al.* [55], a non-local transfer was hypothesized. In other words: a spin current. This concept will be crucial for the interpretation of our experimental findings.

Switching in ferrimagnetic bilayers

A theoretical treatment of synthetic ferrimagnets, i.e. bilayers of antiferromagnetically coupled ferromagnets, was given by Gerlach *et al.* already in 2017 [66]. They

use an atomistic spin model with localized spins that only experience exchange interactions and magnetic uniaxial anisotropy. Gerlach *et al.* performed *ab initio* calculations to obtain the model parameters. The dynamics afters laser excitation are treated with the LLG equation on a very similar footing to Wienholdt *et al.* [3]. Their results indicate that deterministic switching without backswitching or simple relaxation to the initial state only occurs if the equilibrium temperature of the system prior to the excitation is above a threshold temperature. The exchange interaction between Fe and Gd atoms at the interface is found to play an important role as the monolayer resolved dynamics on either side depends on the distance to the interface. Contrary to Atxitia *et al.* precession of the spin vectors is absent in [66] when switching occurs and only present when not. The ratio between Fe and Gd layer thicknesses is found to be irrelevant for switching as long as a magnetization compensation temperature exists, but the thickness may influence the timescales of the dynamics.

A second approach to describe synthetic ferrimagnets was undertaken by Beens *et al.* [7], belonging to the Koopmans group that performed the first experiments on Co/Gd bilayers [6]. The modelling is done in the framework of the M3TM as we saw for GdFeCo alloys in Schellekens *et al.* [65]. In [7] they compare the results of the M3TM for ferrimagnetic alloys and bilayers and find significant differences. While an ambient temperature close to the magnetization compensation temperature is believed to be of crucial importance for AOS in alloys, such a compensation temperature seems to be unimportant for AOS in ferrimagnetic bilayers. The model suggests that switching nucleates at the interface. It is caused by angular momentum transfer between the Co and Gd atoms, which in the M3TM is mediated via exchange scattering of electrons. Subsequently a front of reversed Co magnetization propagates from the interface deeper into the layer. Due to this local character of the initial switching event, the total thickness of the Co layer is irrelevant. The thickness of the Gd layer was not varied in this study, because all experiments were undertaken at room temperature, where only an interface layer of Gd is magnetized by it's proximity to Co. It is therefore particularly possible to switch a bilayer that has no magnetization compensation temperature.

Chapter 3

Experimental Methods

In order to gain a thorough and complete understanding of the sample systems under investigation, we employ a number of different experimental techniques in this work. An introduction to the theoretical background as well as the experimental realization of those techniques will be given in this chapter.

Since they all rely on tuneable X-ray radiation, it is convenient to discuss how to obtain such radiation. Section 3.1 will therefore deal with synchrotrons, specifically the BESSY II facility and it's beamlines.
Once we have established how electromagnetic radiation for our needs is created, we will ask ourselves how it interacts with our sample. In Sec. 3.2 we will therefore go through the basic principles of light-matter interaction. This knowledge sets the ground work for the characterization of thin film systems. The first step will be to determine the layer thicknesses. As we will see later, drastical changes in the magnetic properties of those bilayers can be provoked by manipulating the layer thicknesses. To quantify them we make use of X-ray specular reflectivity, which we will therefore describe in Sec. 3.3.
Having established the more geometrical makeup of the sample, we will start to look into its magnetic properties. Because we are working with bilayers of two chemical species, it is useful to gain element-selective information on the magnetization state. This can be accomplished with X-ray magnetic circular dichroism, which we will elaborate on in Sec. 3.4. Most importantly, XMCD can be expanded to observe magnetization dynamics on an ultrafast timescale by employing the femtoslicing technique.
When we combine X-ray specular reflectivity and XMCD, X-ray resonant magnetic reflectivity (XRMR) emerges, which enables us to glean information on the geometrical properties of the sample magnetization, such as a rotation of the magnetization direction along the growth direction. We will delve into this fascinating technique in Sec. 3.5.

3.1 Synchrotron radiation

Synchrotron radiation was discovered in 1947 as a side product in particle accelerators [67]. Generally speaking any accelerated charge emits radiation. On the one hand the effect is unfortunate for particle accelerators, since the charges need to be constantly re-accelerated to compensate for the energy loss. On the other hand synchrotron radiation lies in the X-ray regime, is broad band in nature and exhibits a very high intensity. It can therefore serve as a more powerful alternative to bremsstrahlung based X-ray tubes. The emitted synchrotron radiation was thus parasitically used for X-ray experiments. The early particle accelerators are known as first generation synchrotrons in that context. The second generation encompasses facilities exclusively build as sources of synchrotron radiation. In this thesis we will be dealing with experiments performed at the third generation synchrotron BESSY II in Berlin.

3.1.1 Berliner Elektronen Speicher Synchrotron - BESSY II

BESSY II consists of a storage ring for electrons with a radius of about 38 m. The trajectory is not strictly circular, as the ring consists of 16 straight sections that are interjected with quadrupole magnets for refocusing and bending magnets, undulators or wigglers that change the direction of the electronic trajectory and generate synchrotron radiation. Photons are guided via a beamline to an adjacent experimental setup.
The kinetic energy of circulating electrons is 1.7 GeV, which is sustained against the energy loss due to synchrotron radiation by microwave cavities.
Electrons travel in spatially - and thereby temporally - separate bunches, that lead to photon pulses of around $5 - 70$ ps. BESSY II can be operated with different filling patterns. The most prevalent is top-up mode in which an overall current of 300 mA is kept constant by regular injections.

The experiments discussed in this thesis were performed at the PM3 beamline and the beamline UE56-1_ZPM. The experimental setup at the latter is also denominated with "FemtoSpex".

PM3 beamline

The radiator of the PM3 beamline is a dipole magnet. Using a SX700 collimated plane-grating monochromator it can be operated in the soft X-ray range of $20 - 2000$ eV [68, 69]. The monochromator's energy resolving-power depends on the size of the exit slit and can reach values of 34000 at an energy of 64 eV. For the presented experiments, the typical exit slit width was 50 μm, with a resolving power of around 20000.
By using a position sensitive diode (PSD), the horizontal beam position may be

automatically controlled to grant very stable operation conditions [68].

This beamline is suited for the investigation of magnetic samples as it provides two basic ingredients. Firstly, the X-ray photons may be elliptically polarized in either direction to about 90 % ellipticity. Secondly, the diffraction chamber installed at the beamline is equipped with an electromagnet that is capable of rotation and generates magnetic fields in the 100 mT range, well above the coercive fields of our thin film layers on the order of at most several 10 mT.
Furthermore the sample holder and detector are both mounted such that they may be rotated independently from each other to accomodate for transmission and reflection geometries at variable angles.

FemtoSpeX

While the PM3 beamline is ideal for the investigation of equilibrium properties, the natural time resolution of the X-ray pulses (50 ps) is not suited for ultrafast magnetization dynamics that have timescales below 1 ps.
The FemtoSpex setup makes use of the femtoslicing technique to generate X-ray pulses of 100 fs length. It is advisable to take a look at the work of Zholents and Zolotorev, who proposed the method in 1996 [70] and Holldack *et al.* [71] for an in-depth article on the beamline. We will go through the basic principles here, as well.

Femtoslicing Slicing is the act of modulating the kinetic energy of a fraction (a "slice") of the electrons of a single bunch. This is accomplished here in a planar wiggler with 10 periods. As the electrons travel on their meandering path, a fs-laserpulse co-propagates along the wiggler axis. The polarization of the pulse is linear in the wiggler plane[1], so the electric field either accelerates or decelerates electrons, depending on the present phase of the wave. For a photon energy of 1.55 eV and a pulse energy of 1 mJ an energy modulation of up to $\Delta E_{max} = 20$ MeV is achievable.

The wiggler is followed by a bending magnet to deflect the entire electron bunch. This maps the kinetic energy profile within the bunch onto an angular distribution as seen in Fig. 3.1. By applying an orbital bump, the electron-beam path may be shifted to point the decelerated portion of electrons into the center of the radiating elliptical undulator, where they emit elliptically polarized X-rays.
The root-mean-square (r.m.s.) pulse length of synchrotron radiation from these sliced electrons is in principle given by the laser-pulse length of 20 fs. Since the electrons travel with a velocity close, but not equal, to the speed of light in the undulator, there is a relative movement of the laser pulse with respect to the electron bunch, however. This leads to temporal broadening of the photon pulses.

[1] and thus parallel to the scattering plane in the diffraction chamber, i.e. p-polarized

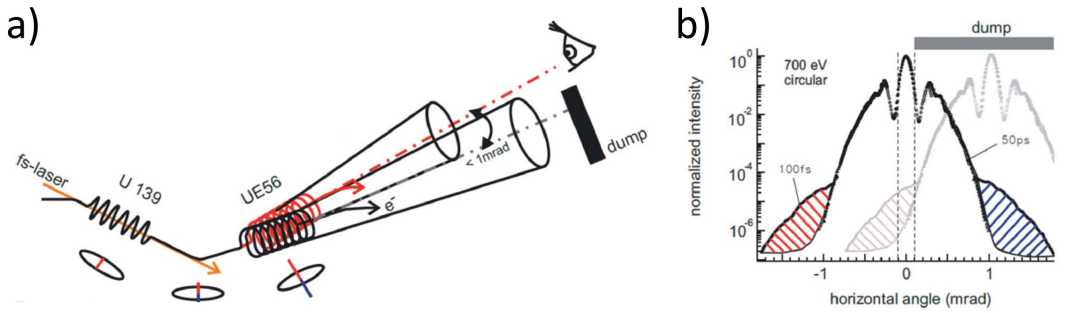

Figure 3.1: a) *Electrons and the fs-laser pulse travel through the wiggler (U 139). A bending magnet deflects the electrons. An orbital bump may be applied to change the trajectory by ca.* 1 mrad.
b) *The angular distribution of photons after the radiator UE56. Photons from decelerated electrons (red) and accelerated electrons (blue) form wings. X-rays from unmodulated electrons are found in the center. The transparent distribution shows the change in trajectory due to the orbital bump. (The image is taken from [71].)*

The resulting 100 fs X-ray pulses are kicked in the beamline, all other photons are dumped [72].
It is noteworthy that the slicing technique suffers from a severe loss of intensity in the X-ray beam as compared to the PM3 beamline for example, because this limits the range of systems that can be feasibly investigated. The ratio of the average flux to the source flux is given by

$$R = \eta \frac{I_b}{I_0} \frac{\nu_L}{\nu_{rev}} \frac{\sigma_L}{\sigma_b} \approx 10^{-8} \ , \tag{3.1}$$

where η is the fraction of modulated electrons ($\eta = 10 - 20\%$), $I_b = 5 - 10$ mA is the intensity of the 'hybrid' bunch on which the slicing is performed, $I_0 = 300$ mA is the total ring current, $\nu_L = 6$ kHz is the laser frequency, $\nu_{rev} = 1.25$ MHz the revolution frequency of the electron bunches and $\sigma_L = 20$ fs and $\sigma_b = 20$ ps the r.m.s. durations of the laser pulse and electron bunch respectively [71].

Laser system The same laser system that drives the femtoslicing technique is also used to generate the pump pulses for time resolved experiments. Pump and probe are thus inherently synchronized, which avoids temporal jitter. A sketch of the beam paths and functional elements is shown in Fig. 3.2.
Key component of the setup is a Ti:Sa laser oscillator. It generates pulses of 20 fs duration. To achieve a pulse power of 1.8 mJ, both the pump and the probe path possess an amplifier. While the probe amplifier works at a repetition rate of 6 kHz, the probe amplifier works with only 3 kHz. In this fashion it is straightforward to measure the pumped and unpumped states of the sample in a single experiment, while simultaneously excluding intensity fluctuations with a sub kHz frequency.

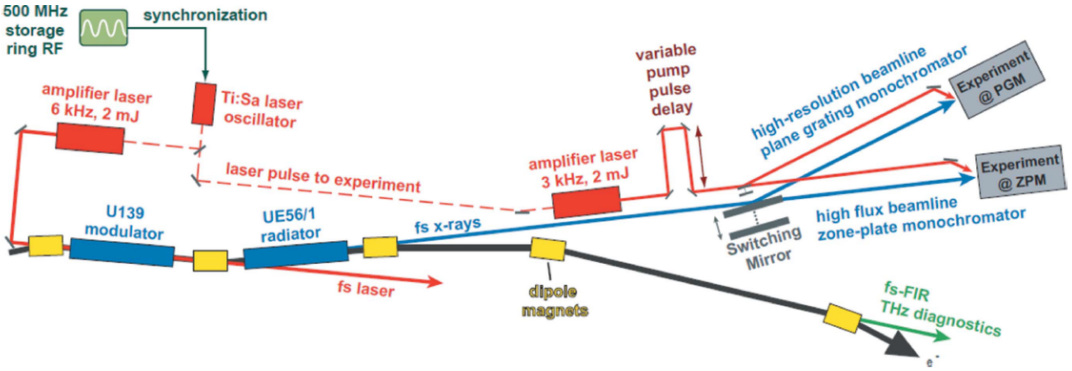

Figure 3.2: *In red we see the beam path of the IR laser. After the oscillator, it splits into a probe (used for femtoslicing) and a pump path, which includes a delay stage. Both paths make use of an amplifier to increase the pulse power.*
In blue we see the beam path of the X-ray side of the experiment. In the planar wiggler (modulator), the laser overlaps with the electron bunch and modulates it's energy. The modulated electrons radiate a fs X-ray pulse in the undulator (radiator), which propagates to the experiment, in our case the ZPM.
(The image is taken from [71].)

Pump and X-ray probe beam meet just before the experimental chamber under a relative angle of 1.5° to each other.

Zone-plate monochromator Considering the reduced intensity resulting from the slicing process, one aims to minimize further losses from X-ray optics. At the same time it is important to avoid pulse elongation when performing time-resolved experiments.
In the FemtoSpeX setup a reflective zone-plate monochromator (RZP) with a maximum transmission of 21% is used, which allows for pulse durations of approximately 100 fs. The downside of a RZP is that the focal distance is wavelength dependent. For that reason the beamline design contains an array of nine zone plates, each optimized for a distinct wavelength and usable in a small interval around it. Overall a range of $410 - 1333$ eV with a spectral resolution up to $\lambda/\Delta\lambda = 500$ is realized[2] [71]. The spectral resolution itself is energy dependent, as the best resolution is only achievable for one energy, the "design energy" of the zone plate in use. Looking back at Subsec. 3.1.1 the importance of the characterization of the sample in a high resolution setup becomes apparent now. In the slicing mode it is ambitious to distinguish detailed spectral features.

[2]The resolution can be interpreted as Gaussian width. At 713 eV it reaches a peak of $\lambda/\Delta\lambda = 2000$.

3.2 Basics of light-matter interaction

For the following sections it is useful to introduce and discuss some fundamental aspects of the interaction of light with matter.

3.2.1 The index of refraction

In continuum optics we characterize a medium by its refractive index n, that determines the wave number[3] k of light within the medium as compared to the wave number k_{vac} in vacuum by

$$k = nk_{vac} \ , \tag{3.2}$$

which, using Fermat's principle, leads to the refraction of light at interfaces according to Snell's law.
To be able to describe absorption, we assume a complex index of refraction

$$n = n' - i\kappa = \sqrt{\epsilon} = 1 - \delta - i\beta \ , \tag{3.3}$$

where the real part can be written as either n' or $1-\delta$ and the imaginary part as either $-\kappa$ or $-\beta$. The second identity is the dielectric constant of the medium ϵ and only applicable in this form for isotropic materials[4]. The third identity is a frequently encountered convention in X-ray physics, where the real part of the refractive index is only slightly smaller than 1 for all materials [30, 73]. We will further on keep to this convention.

Let us describe the electric field of an electromagnetic wave travelling through the medium by a complex exponential of the form

$$E(x,t) = E_0 \mathrm{e}^{i(\omega t - kx)} \ . \tag{3.4}$$

The frequency is given by ω and the wave number by k. The refractive index enters the equation according to Eq. 3.2, giving us

$$E(x,t) = E_0 \mathrm{e}^{i(\omega t - k_{vac}(1-\delta-i\beta))x} = E_0 \mathrm{e}^{i(\omega t - k_{vac}(1-\delta))x} \mathrm{e}^{-k_{vac}\beta x} \ . \tag{3.5}$$

We retain a traveling wave in the first, complex, exponential function. It's wave number is changed, it experiences dispersion. The second exponential describes a decay of the signal due to absorption.

For practical purposes it is usually more useful to work with the radiated power or intensity, given by the absolute square of the electric field

[3] For simplicity we will only consider a 1D problem. Otherwise we use the wave vector $\vec{k}$.
[4] In the most general case, ϵ is a tensor

$$P(x) = |E(x,t)|^2 = P_0 \mathrm{e}^{-2k_{vac}\beta x} = P_0 \mathrm{e}^{-ax} \tag{3.6}$$

with the absorption coefficient $a = 2k_{vac}\beta$. It can be rewritten with the relation $k_{vac} = \frac{2\pi}{\lambda}$ to

$$a = \frac{4\pi\beta}{\lambda} \ , \tag{3.7}$$

where λ is the wavelength of the radiation in vacuum.
Equation 3.6 is known as **Lambert-Beer's law of absorption**. For the full derivation and treatment of this topic see Bergmann and Schäfer [74].

3.2.2 The structure factor

By only considering the index of refraction, we assume the medium to be a homogeneous area without internal structure. This holds true if we consider low photon energies or small scattering angles. For large energies[5], however, the wavelength approaches inter-atomic distances and we need to consider diffraction effects. To this end the structure factor is introduced. It describes the scattered amplitude as a result of interference between the contributions stemming from individual scattering sites within the crystal unit cell. For a reflection in the direction given by the Miller indices (h,k,l) off a general crystal lattice the structure factor reads

$$F(hkl) = \sum_j f_j \mathrm{e}^{-M_j} \mathrm{e}^{2\pi i(hx_j + ky_j + lz_j)} \ . \tag{3.8}$$

The summation is performed over the atomic sites in the unit cell. The quantity M_j describes exponential dampening due to thermal smearing of the atomic positions, while the vector (x_j, y_j, z_j) gives the position of the jth atom [75]. The prefactors $f_j = f_j' - if_j''$ are the complex atomic form factors. As one can see, they give a weight to the scattering amplitude of each individual atom. It is given by the Fourier transform of the effective spatial density distribution of the atom, which in turn can differ for different kinds of radiation.

Without delving too deeply into theoretical considerations, the form factors are closely related to the complex index of refraction as

$$\delta = \frac{r_0\lambda^2}{2\pi}(Z + f')n_{Atom} \tag{3.9}$$

and

[5] Meaning energies on the order of 10^4 eV – 10^5 eV.

$$\beta = \frac{r_0 \lambda^2}{2\pi} f'' n_{Atom} \tag{3.10}$$

with the classical electron radius r_0, the atomic number density n_{Atom} and the number of electrons per atom Z [30]. Substituting the identity Eq. 3.10 into Eq. 3.7 yields

$$a = 2 r_0 \lambda n_{Atom}^2 f'' \ , \tag{3.11}$$

which will be useful shortly.

In the form

$$f_1 = Z + f' \ , f_2 = f'' \tag{3.12}$$

these factors are called *Henke-Gullikson* factors [30] and tabulated for all elements of the periodic table [76].
When working with the relations given in this section, it is imperative to remember, that n and the connected figures δ, β, f', f'', f_1 and f_2 generally depend on the photon frequency.

We will need f' and f'' later on. It is therefore interesting to know how to acquire these values.

3.2.3 Experimental derivation of atomic form factors

Let us assume a XAS experiment in transmission geometry, where the X-ray beam is incident normal to the sample surface. Following the Lambert-Beer law in Eq. 3.6, one measures an intensity of $P(d)$ transmitted through a sample of thickness d. P_0 can be measured by removing the sample entirely or by using a grid in the beamline.
By mathematical transformations and use of Eq. 3.11 we are able to retrieve the energy dependent imaginary part of the atomic form factor, f''. It is then scaled to match the reference non-resonant form factor, archived in the Chantler tables [77], far from the resonance.
To calculate the real part f', we make use of Kramers-Kronig relation:

$$f'(\omega') = \frac{2}{\pi} \mathcal{P} \int_0^\infty \frac{\omega f''(\omega)}{\omega'^2 - \omega^2} d\omega \ . \tag{3.13}$$

Here the principal value integral $\mathcal{P} \int$ is taken to handle the singularity at $\omega' = \omega$. Similarly one may derive the imaginary part f'', given the real part f':

$$f''(\omega') = \frac{2\omega'}{\pi} \mathcal{P} \int_0^\infty \frac{\omega f'(\omega)}{\omega'^2 - \omega^2} d\omega \ . \tag{3.14}$$

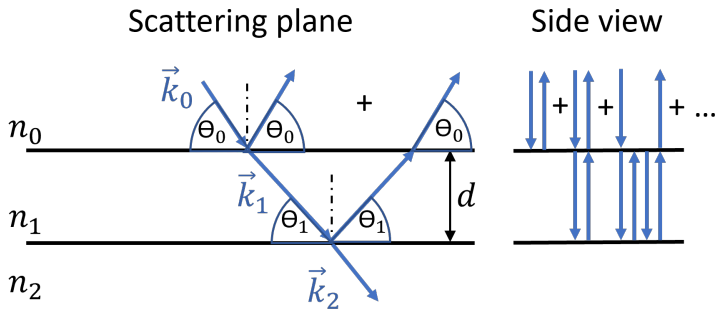

Figure 3.3: *The sample is tilted by an angle θ_0 to the incident X-ray beam. From a medium with refractive index n_0 (usually vacuum) the beam enters a medium with refractive index n_1 through the first interface. It propagates to the second interface with the substrate, that has a refractive index of n_2 and extends infinitely downwards.*
Multiple reflections between the first and second interface may take place. The right-hand side shows a side view of the sample slab and thus only the beam components perpendicular to the interfaces. (The image is an altered version from [78].)

The analysis we perform in Subsec. 5.4.3 makes extensive use of the atomic form factors. It shows how crucial it can be to have access to the atomic form factors of the sample under investigation.

3.3 X-ray specular reflectivity

To specify the thickness of our MBE-grown films, X-ray diffraction in the soft X-ray regime was employed. At an energy of ca. 1 keV the photon wavelength is on the order of 1 nm, which means that we do not resolve information on the atomic, but on the scale of layer thicknesses.

3.3.1 Single homogeneous slab

Consider the setup shown in Fig. 3.3. To simplify calculations we first model a single homogeneous slab, which is tilted by an angle θ_0 to the beam. The incident X-rays are partially transmitted and partially reflected at each interface, which leads to multiple internal reflections[6]. All of them contribute to the overall electromagnetic field propagating in the specular-reflection direction at an angle of $2\theta_0$ with respect to the incident beam.

What we would like to compute is the overall specular amplitude reflectivity

[6]Note that we only consider elastic scattering of X-ray photons.

$$r_{slab} = \frac{E_{ref}}{E_{inc}} \ , \tag{3.15}$$

with the amplitudes E_{inc} and E_{ref} of the incident and reflected electric field, respectively. As mentioned before, we must sum up all contributions that leave the slab surface at an angle $2\theta_0$. This will lead to interference. Thus, there are two figures of importance which we need to track: The amplitude and the phase of the electromagnetic wave.

We start off with the incident beam given by the normalized spatial wave function

$$\Psi(\vec{r}) = \mathrm{e}^{i(\vec{k}_0 \cdot \vec{r})} \tag{3.16}$$

and the following observation:

- The amplitude of a wave in medium i is modified by a factor
  - r_{ij}, upon reflection at the interface to medium j.
  - t_{ij} upon transmission through the interface to medium j.

r_{ij} and t_{ij} represent the reflection and transmission coefficient of an interface, respectively.

Recalling Snell's law, we know that a wave, upon entering a different medium, is refracted and has the new wave vector $|\vec{k}_1| = n|\vec{k}_0|$ and the angle θ_1 with the surface[7]. If, projected onto the surface normal, the wave travels once back and forth in a slab of thickness d, it picks up an additional[8] phase of $2k_1 \sin\theta_1 d = Q_1 d$. The second identity uses the wave-vector transfer $Q_1 = 2k_1 \sin\theta_1$. For further shortening, we will write $p^2 = \mathrm{e}^{iQ_1 d}$.

Adding the prefactors for the first few reflections and re-reflections up as shown in Fig. 3.3 we receive [78]

$$\begin{aligned} r_{slab} &= r_{01} + t_{01}t_{10}r_{12}p^2 + t_{01}t_{10}r_{10}r_{12}^2p^4 + t_{01}t_{10}r_{10}^2r_{12}^3p^6 \ ... \\ &= r_{01} + t_{01}t_{10}r_{12}p^2\{1 + r_{10}r_{12}p^2 + r_{10}^2r_{12}^2p^4 \ ...\} \\ &= r_{01} + t_{01}t_{10}r_{12}p^2 \sum_{m=0}^{\infty} (r_{10}r_{12}p^2)^m \end{aligned} \tag{3.17}$$

[7]Since the refractive index for X-rays is smaller than unity, the beam is refracted towards the interface.

[8]Because of the continuity condition of the wave function at interfaces, the wave-vector component parallel to the surface is equal for all partial waves and the phase in this direction as well. So we will neglect it.

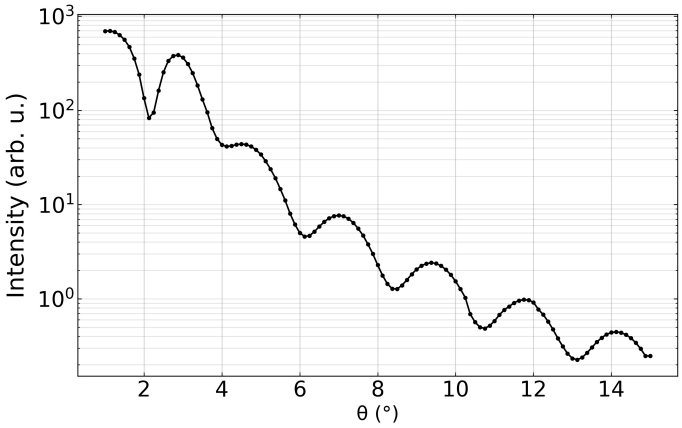

Figure 3.4: *Kiessig fringes measured with a photon energy of* 1100 eV *for a* 140 Å *thick Gd(0001) film on a W(110) substrate. The experiment was performed at the PM3 beamline of BESSY II.*

This is a geometric series with the solution

$$r_{slab} = r_{01} + t_{01}t_{10}r_{12}p^2\frac{1}{1 - r_{10}r_{12}p^2} \ , \tag{3.18}$$

which can be rewritten to

$$r_{slab} = \frac{r_{01} + r_{12}p^2}{1 + r_{01}r_{12}p^2} \tag{3.19}$$

using the identities $r_{01} = -r_{10}$ and $t_{01}t_{10} = 1 - r_{01}^2$ that follow from the Fresnel equations[9].
Figure 3.4 shows an experimental example of the resulting amplitude modulation called Kiessig fringes. Note the semilogarithmic scale.

In the same manner we can derive the transmissivity

$$t_{slab} = \frac{t_{01}t_{12}p^2}{1 + r_{01}r_{12}p^2} \ . \tag{3.20}$$

We will make use of the simulation software IMD by David Windt [79] in Chs. 4, 5 and 6. It calculates the transmittance, absorptance and reflectance of a multilayer recursively, i.e. it starts by applying Eq. 3.20 to the bottom layer and uses the resulting overall reflectivity of the bottom layer r_{slab} for r_{12} of the layer on top and so forth. It can also compute the electric field intensity as a function of depth within the sample with the help of Maxwell's equations. We will see its application later on.

[9]The identities are true for s- and p-polarization and consequently for circular polarization.

3.3.2 Matrix formalism

In the previous treatment we kept track of all light paths through the sample layer and summed them up, which is quite demonstrative. But the method is only feasible for a single slab and already impractical for a bilayer. Let us therefore discuss a different approach, which is easily expandable to an arbitrary number of layers[10].

According to Maxwell's equations the tangential components of the electric and magnetic fields are continuous, i.e. the field components parallel to the interface must be equal on both sides. With some algebra this can be expressed in the form of a matrix [80]. It links the tangential components of the electric field between adjacent layers m and $m-1$:

$$\begin{bmatrix} E_{m-1}^{+} \\ E_{m-1}^{-} \end{bmatrix} = \frac{1}{t_m} \begin{bmatrix} \mathrm{e}^{i\delta_{m-1}} & r_m \mathrm{e}^{i\delta_{m-1}} \\ r_m \mathrm{e}^{-i\delta_{m-1}} & \mathrm{e}^{-i\delta_{m-1}} \end{bmatrix} \begin{bmatrix} E_m^{+} \\ E_m^{-} \end{bmatrix} = \frac{1}{t_m} \underline{\underline{C_m}} \begin{bmatrix} E_m^{+} \\ E_m^{-} \end{bmatrix} \tag{3.21}$$

The superscripts "+" and "-" denote such partial waves that propagate down or up respectively. In this way, we do no longer distinguish whether a partial wave has been reflected or transmitted before propagating in the direction it does. We simply combine all partial waves with the same propagation direction into one wave. The situation is sketched in Fig. 3.5.

We now make use of the amplitude reflectivity and transmissivity r_m and t_m of the interface between layers $m-1$ and m as given by the appropriate Fresnel equations. The acquired phase is described by the parameter δ_m as

$$\delta_m = \frac{2\pi n_m \sin\theta_m}{\lambda} \sum_{i=1}^{m-1} d_i \tag{3.22}$$

where the sum stretches over the layer thicknesses d_i.
It is possible to split the matrix into a propagation and a boundary part as

$$\underline{\underline{C_m}} = \underline{\underline{P_m}} \cdot \underline{\underline{A_m}} = \begin{bmatrix} \mathrm{e}^{i\delta_{m-1}} & 0 \\ 0 & \mathrm{e}^{-i\delta_{m-1}} \end{bmatrix} \cdot \begin{bmatrix} 1 & r_m \\ r_m & 1 \end{bmatrix} \tag{3.23}$$

This will become useful in Sec. 3.5.

Amplitude reflectivity & transmissivity

As in the previous approach, we would eventually like to know the reflection and transmission coefficient of the entire film. We therefore express the electric field amplitudes on the vacuum side through those of the substrate side by matrix multiplication. Vacuum is denoted as the layer "0". The substrate is denoted as

[10] albeit not easily calculated by hand

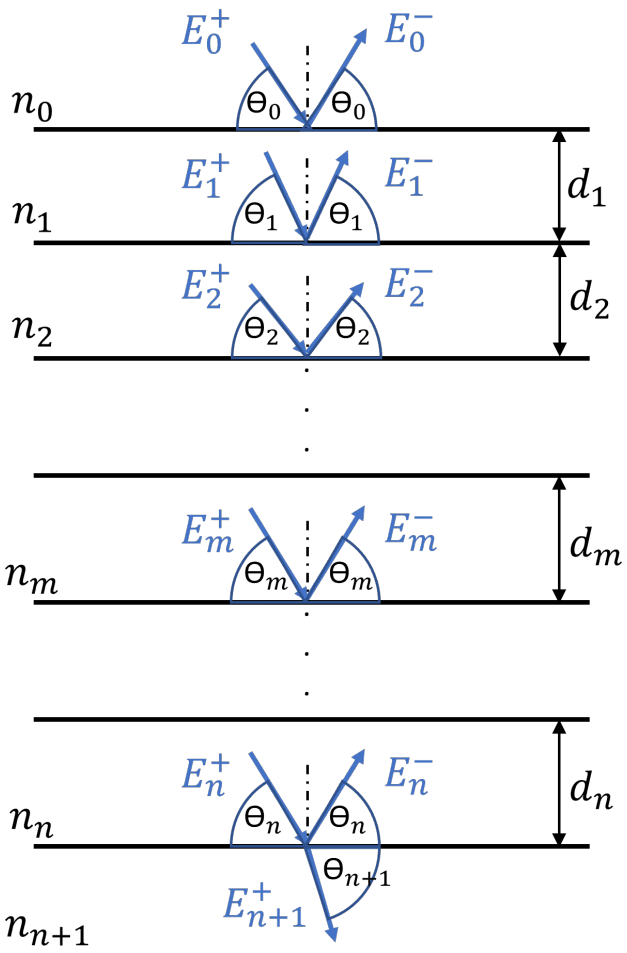

Figure 3.5: *Illustration of a multilayer film with n layers on top of a substrate denoted by $n+1$. The layer m symbolizes an arbitrary layer in the film. The sum of all downwards propagating waves in layer m has the electric field amplitude E_m^+, while it is E_m^- for upwards propagating waves. A layer has a thickness d_m.*
The X-ray beam is incident at an angle θ_0 from a medium with refractive index n_0. The refracted angle in layer m with refractive index n_m is θ_m respectively.
(The image is an altered version from [80].)

the layer "$n+1$" and characterized by the fact that no wave propagates upwards in it, meaning $E^-_{n+1} = 0$. We thus have

$$\begin{bmatrix} E^+_0 \\ E^-_0 \end{bmatrix} = \frac{\underline{\underline{C_1 C_2 ... C_{n+1}}}}{t_1 t_2 ... t_{n+1}} \begin{bmatrix} E^+_{n+1} \\ 0 \end{bmatrix} = \begin{bmatrix} a & b \\ c & d \end{bmatrix} \begin{bmatrix} E^+_{n+1} \\ 0 \end{bmatrix} \tag{3.24}$$

The desired reflection coefficient of the entire film is given by

$$r_{film} = \frac{E^-_0}{E^+_0} = \frac{c}{a} \ , \tag{3.25}$$

and the transmission coefficient by

$$t_{film} = \frac{E^+_{n+1}}{E^+_0} = \frac{t_1 t_2 ... t_{n+1}}{a} \ . \tag{3.26}$$

A more extensive derivation as well as computationally useful recursive relations for the calculation of the product-matrix elements can be found in Heavens [80].

3.4 X-ray magnetic circular dichroism

We have seen in Sec. 3.2 that the interaction of light with matter can be described by the complex index of refraction n in Eq. 3.3. It can be divided into two effects: absorption, given by the imaginary part of n and scattering, given by the real part of n. We have also seen, that the two are fundamentally connected by the Kramers-Kronig relation Eq. 3.13. Both phenomena are therefore described as scattering events.

A distinction is made between non-resonant and resonant scattering. In a non-resonant scattering event, an X-ray photon may be absorbed by an electron, which gains enough energy to leave the parent atom, which is therefore ionized. It is clear that there is a threshold energy corresponding to the binding energy of the electron. When going from valence to core level shells, the binding energy increases. The absorption cross section of the atom will thus exhibit steps as a function of photon energy, whenever the threshold for an electronic shell is reached. This behavior is described by the *Henke-Gullikson* factors f_1 and f_2 in Eq. 3.12, specifically the non-resonant factors that are tabulated in the Chantler tables [77].

If, however, the photon energy matches an electronic transition between a core and valence shell, we observe resonant scattering. It can be shown that the cross section for resonant scattering is enhanced by a factor of about 10^4 over the non-resonant scattering cross section for photon energies in the soft X-ray regime of ca. 1 keV [30]. The resulting resonant peaks, also known as fine structure, are

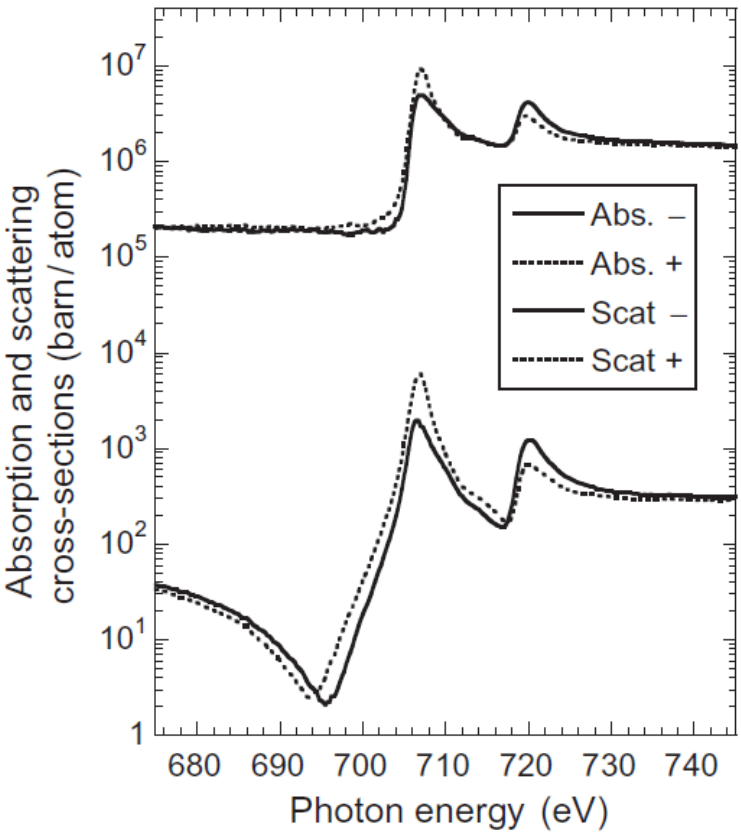

Figure 3.6: ***Top:*** *XMCD cross-section of the absorbed intensity at the Fe L-edges.* ***Bottom:*** *XMCD cross-section of the elastically scattered intensity. (The image is taken from [30].)*

overlaid with the non-resonant steps.

In the experiments of this work, resonant scattering at the L_3 and L_2 edges of Fe as well as at the M_5 and M_4 edges of Gd was investigated. It entails the absorption and reemission of a photon. Our considerations up to here mean that the reflected X-ray intensity contains much of the same information about the electronic transitions as the absorbed intensity. However, since the angle dependent reflectivity and effects such as interference play an additional role, the observed intensity takes a different shape as a function of energy as illustrated in Fig. 3.6. More precisely, the cross section for absorption is only determined by f_2 [30] (optical theorem)

$$\sigma^{abs}(E) \propto f_2(E) \ , \tag{3.27}$$

while the cross section for resonant scattering as measured in reflection is given by both f_1 and f_2

$$\sigma^{scat}(E) \propto [f_1(E)]^2 + [f_2(E)]^2 \ . \tag{3.28}$$

In the following we will discuss the electronic transitions within the picture of resonant absorption.

If we analyze the absorbed intensity more quantitatively, we need to make a

quantum mechanical calculation. For example for the Fe L_3 edge we calculate the transition probability of an electron from the $2p_{3/2}$ to the $3d$ state. It is worthwhile to note that $J = 3/2$ in the $2p$ state entails spin-orbit coupling. In the ground state of the atom, the $2p$ state is fully occupied and spin-orbit coupling does not play a role. The consideration of SOC reflects the missing electron in the excited state - after photon absorption. Since both the relaxation of the electronic shell and the electronic transition happen simultaneously, we need to take the atomic final state into account.
We find that the intensity averaged over all relative orientations between sample and photon polarization[11] is in general proportional to the number of holes or empty states N_h in the atomic ground state[12]. For the L-edge of 3d transition metals we get [30]

$$\langle I \rangle = \mathcal{A}\mathcal{R}^2 \frac{L}{3(2L+1)} N_h \ , \tag{3.29}$$

where L is the angular momentum quantum number.
For the L_3 edge we get

$$\langle I \rangle = \frac{2\mathcal{A}\mathcal{R}^2}{15} N_h \tag{3.30}$$

with $\mathcal{A} = 4\pi^2\hbar\omega/137$ and $\mathcal{R}$ the radial matrix element of the dipole operator.

Experimentally we would like to find out the magnetic moment of the atoms in our sample, which is given by the difference between spin-up holes and spin-down holes. This means we ideally need a way to drive transitions preferentially into either kind of holes. This is accomplished with circularly polarized photons.
For an antiparallel alignment of photon spin and sample magnetization we may write

$$I^{\uparrow\downarrow} = \mathcal{A}\mathcal{R}^2 \sum_{states} |\langle C^{(1)}_{-1} \rangle|^2 \ , \tag{3.31}$$

and for parallel alignment similarly

$$I^{\uparrow\uparrow} = \mathcal{A}\mathcal{R}^2 \sum_{states} |\langle C^{(1)}_{+1} \rangle|^2 \ . \tag{3.32}$$

Here the dipole matrix elements of Racah's spherical tensors were used [30]

$$\langle C^{(1)}_q \rangle = \langle d_{n,\chi^+} | C^{(1)}_q | p_j, m_j \rangle \ . \tag{3.33}$$

The initial state is denoted by the specific multiplet state p_j and the quantum number m_j for the projection of the total angular momentum on the quantization

[11] To exclude anisotropy effects.
[12] Not the excited state!

axis. The final state is given as the n'th d-state with spin up χ^+. The subscript q denotes the circular polarization direction.
The desired quantity is the XMCD difference intensity [30]

$$\Delta I_{XMCD} = I^{\uparrow\downarrow} - I^{\uparrow\uparrow} = \mathcal{A}\mathcal{R}^2 \sum_{states} |\langle C^{(1)}_{-1}\rangle|^2 - |\langle C^{(1)}_{+1}\rangle|^2 \ . \tag{3.34}$$

The sign is given by convention and chosen such that $I_{XMCD} < 0$ for the L_3 edge of $3d$ metals. Why it is different from zero at all is illustrated in the two-step model of XMCD below.

3.4.1 The two-step model

The excitation with circularly polarized photons can be depicted in two distinct steps.
In step one the electron absorbs the photon. We must keep in mind that circular polarization bestows an angular momentum of $\pm\hbar$ on the photon, depending on the polarization direction. And furthermore that angular momentum is a conserved quantity. The photon cannot directly interact with the spin of the electron, but with the orbital angular momentum. Since the initial state of the electronic transition experiences spin-orbit coupling, neither spin nor orbital angular momentum are good quantum numbers. The angular momentum is instead transferred to the total angular momentum $\vec{J}$ and thereby indirectly to the spin. For that reason one speaks of "spin polarization" in this step.

In step two the relation of Eq. 3.29 comes into play: If there is a different number of spin-up and spin-down holes, one observes a preferential transition of either kind of electrons. This is the case for ferromagnets. They exhibit an exchange splitting of their valence states, which shifts the spin-up (minority spin[13]) state further above the Fermi energy, creating more spin-up holes, as illustrated in the top left corner of Fig. 3.7. The resulting inequality of electronic transitions excited by left- and right-circularly polarized photons is given on the right-hand side of the figure. The results were obtained in the aforementioned atomic one-electron picture. We further assume that the photons are perfectly polarized and that their momentum vector is parallel to the sample magnetization.

In general the XMCD difference intensity is proportional to the amount of circular polarization P_{circ} and the projection of the magnetic moment $\vec{m}$ onto the photon angular momentum $\vec{L}_{ph}$ as

$$I_{XMCD} \propto P_{circ}\vec{m} \cdot \vec{L}_{ph} \propto P_{circ} \cdot m\cos\theta \ . \tag{3.35}$$

[13]Note that spin and magnetic moment are oppositely aligned.

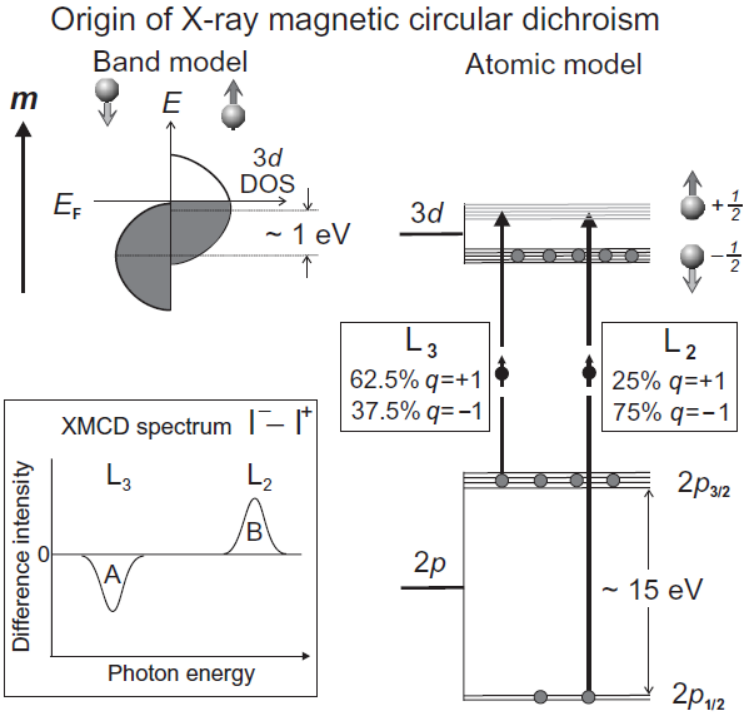

Figure 3.7: Top left: *Schematic illustration of the density of states of an exchange-split 3d band. The spin-minority states are shifted up in energy. Due to the proximity of the Fermi energy, they are only partially filled.* ***Right:*** *The fraction of p-electrons undergoing a transition at the L_3 and L_2 edges for excitations with left or right circularly polarized photons.* ***Bottom left:*** *The intensity difference between L_3 and L_2 edge spectra recorded with both circular polarizations. (image taken from [30])*

3.5 X-ray resonant magnetic reflectivity

X-ray resonant magnetic reflectivity (XRMR) is an experimental method that combines the two concepts of X-ray magnetic circular dichroism (XMCD) and X-ray specular reflectivity.
As in specular reflectivity experiments, we use a $\theta - 2\theta$ geometry in our measurements. Instead of an energy far from resonance, the energy of the X-rays is tuned to a magnetically sensitive absorption edge[14], such as the $M_{4,5}$ edges for Gd and the $L_{2,3}$ edges for Fe, as in XMCD.
In the same manner as we obtained the Kiessig fringes in Sec. 3.3, we vary θ in the measurement by rotating sample and detector simultaneously. At the same time we record the XMCD by applying an external magnetic field parallel to the sample surface with a non-vanishing projection onto the beam direction and alternating the polarity of the magnetic field for each angle θ.

Due to the complexity of the problem, the experimental data of XRMR cannot

[14] that means transitions into n-l-levels, which carry a part of the sample magnetization

readily be interpreted or fitted to a simple mathematical model. Instead we make use of the software tool *DYNA* that was developed by Elzo, Jal *et al.* [81] at the Sorbonne University in Paris to simulate the data. Our goal in the following is to grasp the key concepts of the formalism without deriving it in detail.

3.5.1 DYNA matrix formalism

Dielectric permittivity and refractive index

As mentioned in Subsec. 3.2.3 one can derive the complex atomic form factors f' and f'' and the closely related Henke-Gullikson factors f_1 and f_2 from absorption spectra. Similarly one may define magnetic factors $\mathcal{M}_1$ and $\mathcal{M}_2$, where $\mathcal{M}_2$ is derived from the intensity difference in XMCD and $\mathcal{M}_1$ via the Kramers-Kronig relation from $\mathcal{M}_2$. Using these factors we can write for the elastic resonant magnetic form factor

$$F(\hbar\omega) \approx [(\hat{\epsilon}_2^* \cdot \hat{\epsilon}_1)(f_1(E) + if_2(E)) - i(\hat{\epsilon}_2^* \times \hat{\epsilon}_1) \cdot \hat{m}(\mathcal{M}_1(E) + i\mathcal{M}_2(E))] \quad (3.36)$$

$$= [(\hat{\epsilon}_2^* \cdot \hat{\epsilon}_1)F_C - i(\hat{\epsilon}_2^* \times \hat{\epsilon}_1) \cdot \hat{m}F_M] \ . \quad (3.37)$$

Since the experimentally determined form factors are scaled to the Chantler table [77], we ignore constant prefactors here.

Because the magnetization of the sample introduces an anisotropy, the dielectric permittivity must no longer be considered as a scalar, but a tensor $\underline{\underline{\epsilon}}$. It is directly connected to the scattering factor $F(\hbar\omega)$:

$$\underline{\underline{\epsilon}} = 1 + \underline{\underline{\chi}} \ , \quad (3.38)$$

$$\underline{\underline{\chi}} = \frac{4\pi}{k_0^2} \sum_a \rho_a F_a \ , \quad (3.39)$$

where ρ_a is the number of atoms a per unit volume and F_a takes values from Eq. 3.37. Interestingly, this means that $\underline{\underline{\epsilon}}$ contains the magnetic information of spin-orbit effects in the core hole[15] through F_M. We receive

$$\underline{\underline{\epsilon}} = \begin{bmatrix} \epsilon & \epsilon_{xy} & \epsilon_{xz} \\ -\epsilon_{xy} & \epsilon & \epsilon_{yz} \\ -\epsilon_{xz} & -\epsilon_{yz} & \epsilon \end{bmatrix} \quad (3.40)$$

with

$$\epsilon = 1 + \frac{4\pi}{k_0^2}\rho F_C \ , \quad (3.41)$$

[15] Since this is a purely charge-based effect, the magnetic permeability is assumed as $\mu = 1$.

$$\epsilon_{xy} = -i\frac{4\pi}{k_0^2}\rho m_z F_M \ ,$$

$$\epsilon_{xz} = i\frac{4\pi}{k_0^2}\rho m_y F_M \ .$$

We can see that the off-diagonal terms of $\underline{\underline{\epsilon}}$ are zero if we neglect the magnetic contribution.
In addition, the DYNA formalism takes a finite roughness of the interfaces into account. It is assumed to be Gaussian in nature with a width of σ, which translates into an error-function-like change of the dielectric permittivity between layers $m-1$ and m:

$$\epsilon = \epsilon_m + (\epsilon_{m-1} - \epsilon_m)\,\mathrm{Erf}(z, \sigma) \tag{3.42}$$

This makes the roughness spacially homogeneous, i.e. it does not depend on the position in space. In practice an increased roughness of the interfaces makes itself felt by smearing out the Kiessig fringes in the angle dependent measurement.

For an eigenwave[16] propagating along the z-direction one finds the connection between refractive index and dielectric permittivity to be

$$n^{\pm} \approx \sqrt{\epsilon \pm i\epsilon_{xy}} \tag{3.43}$$

The $\pm$-sign indicates the difference in refractive index for waves traveling up or down in the medium. One finds equivalent relations for other propagation directions. $n^{\pm}$ becomes identical to the simple case of $n = \sqrt{\epsilon}$ if the off-diagonal terms of the permittivity tensor vanish, meaning for non-magnetic materials.

If we link the refractive index with the optical factors F_C and F_M from Eq. 3.36 we get

$$n^{\pm} \approx 1 + \frac{r_0\lambda^2\rho}{2\pi}(F_C \mp (\cos\theta m_{Lon} + \sin\theta m_{OP})F_M) \ , \tag{3.44}$$

where m_{Lon} and m_{OP} denote the longitudinal and out-of-plane component of the magnetization respectively, as shown in Fig. 3.8. We can directly see that the effect of the longitudinal component is most pronounced at small angles, while the out-of-plane component becomes dominant at large angles. This is in line with our findings from Sec. 3.4, namely that XMCD is only sensitive to magnetization components parallel to the polarization vector (i.e. propagation direction of the photons).

[16] Eigenwaves are those that do not experience a change of polarization upon propagating through the medium.

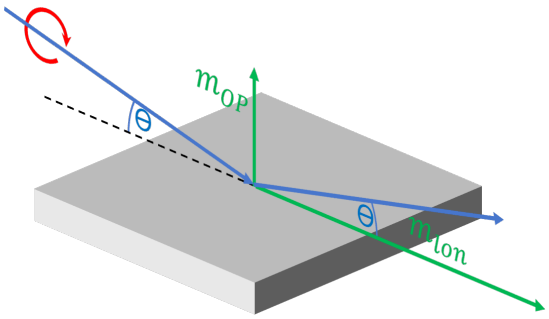

Figure 3.8: *For a circularly polarized X-ray beam incident at a finite angle θ, there is a finite projection of the magnetization components m_{Lon} and m_{OP} onto the polarization vector.*

Transmission and propagation

The problem of transmission and propagation in a multilayer film can be treated on the same footing as the matrix formalism in Subsec. 3.3.2. Employing the boundary condition that the tangential components of the electric and magnetic fields must be continuous at layer interfaces, we arrive at boundary as well as propagation matrices. The connection between incoming and outgoing waves is obtained as the product of matrices for each layer and interface. Similar to Eqs. 3.23 and 3.24 DYNA can thus express the reflected, outgoing wave in terms of the incident wave and a series of boundary and propagation matrices. In Subsec. 3.3.2 we saw that the refractive index enters Eq. 3.22. We can draw a connection to the refractive index in Eq. 3.44 there.

3.6 Sample preparation

3.6.1 W(110) substrate

To provide a suitable substrate for epitaxial growth, we use a W(110) crystal. It combines ideal growth conditions for Gd with a very high melting temperature of 3422 °C. This allows for high temperature flashes to clean the substrate and reuse it many times.

Tungsten, on the one hand, has a bcc crystal structure with a cubic lattice constant of $a_W = 3.17$ Å. Along the [110] direction we obtain a pseudo-hexagonal structure. On the other hand, Gd has a hcp crystal structure with a lattice constant in the (0001) plane of $a_{Gd} = 3.64$ Å and of $c = 5.78$ Å in the [0001] growth direction. We can see that the lattice mismatch between W and Gd is between 13% and 24.5% depending on the direction, as W is only pseudo and not truly hexagonal. Nevertheless detailed LEED studies by Nepijko *et al.* [82] have shown that the deviation of the Gd lattice constant from it's bulk value, when grown on W(110), only amounts to 2% in the first monolayer and 0.3% in the second. The third and following monolayers already grow with the bulk lattice constant.

Tungsten is known to exhibit carbon contaminations [83], which form super-

structures on the crystal surface and influence the quality of films grown on the substrate. It is therefore mandatory to deplete the surface region of carbon. The precise procedure used for this depends on the crystal[17], sample-holder surroundings and vacuum chamber [84]. There are two principle steps: Firstly, carbon segregation to the surface and simultaneous oxidation. Secondly, flashing off of carbon oxides. Such procedures are described in several publications [85, 86]. For the first step we elevate the crystal temperature to 1200 °C at a base pressure of 3×10^{-11} mbar and introduce an oxygen atmosphere to reach 5×10^{-8} mbar. After 30 min the oxygen influx is stopped and we perform the second step with a short flash of the sample to 1800 °C. The heating of the crystal is realized by electron-beam bombardment.
This procedure is repeated several times to obtain a clean substrate surface. Even for a cleaned crystal it is mandatory to check the surface for carbon superstructures regularly, because each flashing event promotes carbon segregation to the surface. This can be handily accomplished with low-energy electron diffraction [82].

3.6.2 Evaporators

We employ two different evaporator designs in this experiment.
For Gd, we use a home-build electron-beam (e-beam) evaporator. Gd metal is molten into a tungsten crucible prior to evaporation. It can be heated via electron bombardment to evaporate Gd atoms into a relatively large solid angle in front of the evaporator, limited by a cylindrical tantalum cover around the evaporator setup to reduce unintentional coating of vacuum components. Depending on the temperature reached in the crucible and the surrounding pressure, a certain evaporation rate is achieved and maintained with a quartz-crystal microbalance. The heating power is determined as the product of emission current[18] I_{emis} and acceleration voltage V and held constant by the automated variation of V.

For Fe evaporation, we employ the commercial EFM3 model from *FOCUS*, which is functionally mostly equivalent to the aforementioned design. Different from the Gd evaporator, the EFM3 uses electron bombardment of an Fe rod rather than a crucible. The evaporation-cone is furthermore spatially more focused than for Gd by a narrow nozzle. The heating power is controlled via I_{emis}, while V is held constant.

3.6.3 Gd film

To ensure a clean substrate surface, the W crystal was flashed before the evaporation to a temperature of about $1800°C$.
The evaporation rate of the Gd evaporator was determined as (4.0 ± 0.1) Å/min and held constant for a duration of (2.5 ± 0.02) h in a pressure of $(1.0 \pm 0.3) \times 10^{-9}$ mbar.

[17] Our W crystal has a cylindrical shape with a diameter of 8 mm and a height of 3 mm.
[18] The electron current between the electron emitting filament and the crucible.

The resulting thickness is (600 ± 20) Å. Gd is highly reactive. It is thus preferrable to evaporate it at an even lower pressure in the 10^{-10} mbar range. As a result, it is common to find a reduced saturation magnetization. But without an absolute measure of the magnetization or spin polarization, it is not possible to quantify this effect.
To improve the sample crystallinity the film was annealed for an extended period of 5 min at a temperature of 800 °C. A study into the optimal annealing temperature for Gd films performed by Aspelmeier *et al.* [87] extends only to thicknesses of ca. 30 nm and proposes an annealing temperature of ca. $650°C$.
Because we use no capping layer for this film, the transport to the experimental chamber was done by way of a vacuum suitcase. As the sample needs to pass a loadlock to reach the suitcase, it was exposed to a pressure of $(6.3 \pm 0.1) \times 10^{-6}$ mbar for several seconds. Consecutively one may assume that the topmost layers of the film are oxidized. The influence of these layers is however suppressed due to the large thickness of the film.

3.6.4 Y/Fe/Gd film

Calibration

The evaporation rate r_{QMB} of Gd is determined before and after evaporation by moving a quartz micro-balance (QMB) into the approximate evaporation position of the sample substrate. This proved to be unfeasible for Fe, since the very narrow evaporation cone complicated the adjustment of the QMB position[19].
In order to calibrate the evaporation rates, we grew single elemental layers and performed X-ray reflectometry measurements to determine their thickness. For Gd we found an evaporation rate of $r_{Gd,Diff} = T \cdot r_{Gd,QMB}$, with the tooling factor $T = 0.91 \pm 0.01$. The discrepancy indicates that the position of the QMB is not wholly equivalent to the sample position, which helps to explain the problems in aligning the Fe signal on the QMB.
The Fe evaporation rate according to X-ray reflectometry was $r_{Fe,Diff} = 1.27 \pm 0.02$ Å/min. Since $r_{Fe,QMB}$ has an inacceptably large uncertainty, we must rely on stable evaporation conditions of the EFM3 evaporator to allow the use of $r_{Fe,Diff}$. The EFM3 possesses a flux meter, which is sensitive to the ion current through the nozzle of the evaporator[20]. The ion current, or flux, is expected to be proportional to the evaporation rate. The flux during the evaporation of the calibration sample was $I_{f,calib} = (14.5 \pm 1.5)$ nA.

Evaporation

As before, prior to sample growth, the W crystal was flashed to a temperature of (1828 ± 10) °C in order to remove adatoms.

[19] The measured rate varied in the range $0.2 - 1.6$ Å/min

[20] Electron bombardment leads to the emission of charged and neutral particles, single atoms and clusters of different sizes.

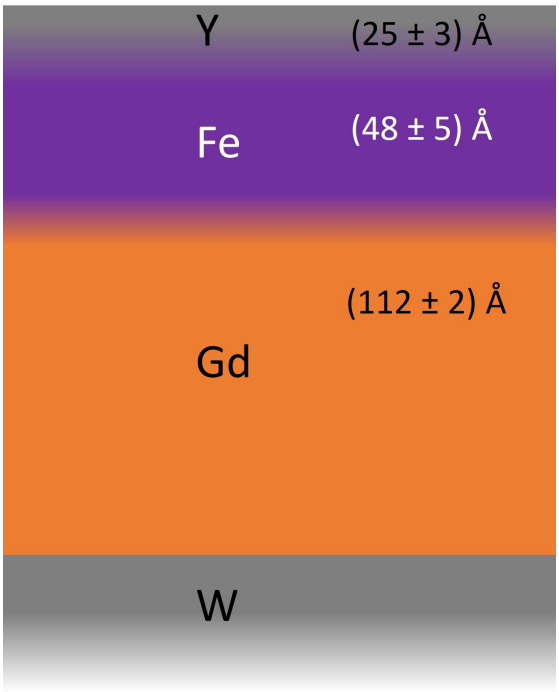

Figure 3.9: *Sample structure of the Y/Fe/Gd layer with the respective layer thicknesses.*

The first functional layer was Gd. We operated the e-beam evaporator at a heating power of 50 W. The evaporation rate, including the tooling factor, was (2.79 ± 0.22) Å/min before and after the evaporation process. With this rate we evaporated for (48.4 ± 0.1) min and thus expect a thickness of (135 ± 11) Å. Our analysis of diffraction experiments on the sample in Subsec. 5.4.2 reveals a thickness of (112 ± 2) Å for the Gd layer. The discrepancy may stem from a systematic error of the evaporation rate as determined by the quartz-micro balance. Because the position of the QMB is not fully equivalent to the sample position.
To ensure a high crystallinity the Gd layer is annealed via e-beam heating to a temperature of (316 ± 5)°C for 1 min.
In the case of Fe/Gd we have a unique opportunity to quantify the saturation magnetization, as we will see in Ch. 5.

The second functional layer was Fe. With a heating power of 9.7 W the EFM3 was stabilized at a flux of $I_{f,bi} = (13.5 \pm 1.5)$ nA, well within the range of $I_{f,calib}$. The evaporation time was (40.0 ± 0.1) min and we expect a thickness of (50 ± 4) Å. The analysis in Subsec. 5.4.2 agrees with this, resulting in a thickness of (48 ± 5) Å for the Fe layer.
To prevent oxidation during the sample transport through ambient air, we added a Y capping layer. Y is evaporated from an e-beam evaporator equivalently to Gd. The evaporation rate was not calibrated, because Y is not a functional layer and all measurements were carried out far from any Y resonances. The precise thickness of Y is therefore not crucial.
The Y e-beam evaporator was operated with a heating power of 60 W, which resulted in an evaporation rate of $r_{Y,QMB} = (2.1 \pm 0.2)$ Å/min. With an evaporation time of (12.0 ± 0.1) min we expect a thickness of (25 ± 3) Å.

Figure 3.9 depicts the sample structure with the respective thicknesses. For Fe we

will use the thickness based on our evaporation rate calibration. For the Y capping layer we rely on the QMB to determine the evaporation rate and thickness. Finally for Gd we will use the diffraction based thickness. We will see in Subsec. 5.4.2 that this method is very precise.

Chapter 4

Magnetization dynamics of Gd revisited

As we touched upon in Subsec. 2.1.3, the microscopic processes underlying the ultrafast magnetization dynamics of Gd are not fully understood. We will try to shed some light on the puzzling results that have been obtained so far. This has the additional advantage of providing us with a solid foundation to investigate Fe/Gd bilayers later on.

In the case of a 10 nm Gd film, ARPES and XMCD yielded contradicting results for the $4f$ magnetic response to optical excitations. While the XMCD $4f$ study found a double-exponential decay with a sub-picosecond timescale [20], it is absent in the ARPES $4f$ study, where sub-picosecond dynamics were only observed in the $5d6s$ system [2]. This unsolved puzzle raised a controversial debate about non-equilibrium $4f - 5d$ coupling.

We elucidate the above incongruity by considering the distinct probing depths in ARPES and XMCD. While ARPES is only sensitive to the first few atomic layers, due to the small mean free path of electrons, X-rays can penetrate several nanometers of the sample, even under resonance conditions. We therefore speculate that effects at the film-substrate interface may be relevant for the interpretation of the dynamic signal in a 10 nm Gd film. The main suspect is electronic and spin transport, which is expected to occur on the ultrafast timescale. We will discuss it in more detail later on.

Here we will present an experiment, performed at the FemtoSpeX slicing facility of BESSY II and compare it to the XMCD investigation of Bobowski *et al.* [20]. In this experiment, we aim to test for interface effects on the ultrafast $4f$ dynamics, with transport effects in mind. For this purpose we would like to prohibit transport within the sample. One option is to use an insulating substrate. But it goes hand in hand with strongly changing the growth conditions and negatively influences the magnetization of the Gd layer. Instead we increased the sample thickness such that we are insensitive to the substrate interface and obtain the signal from

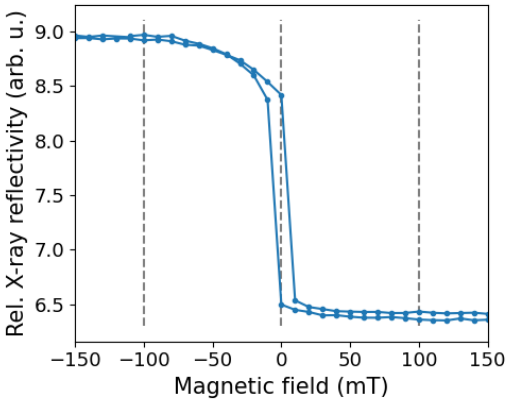

Figure 4.1: *Magnetic hysteresis of the Gd film at a photon energy of* 1188.2 eV *at the Gd M_5 edge. The film was measured in reflection geometry with an incidence angle of $\theta = 5°$. The magnetic field was applied in the sample plane. The y-axis displays the reflected signal in arbitrary units. The zero field as well as* ±100 mT *are indicated by the horizontal dashed lines. The film temperature was $T = 87$ K.*

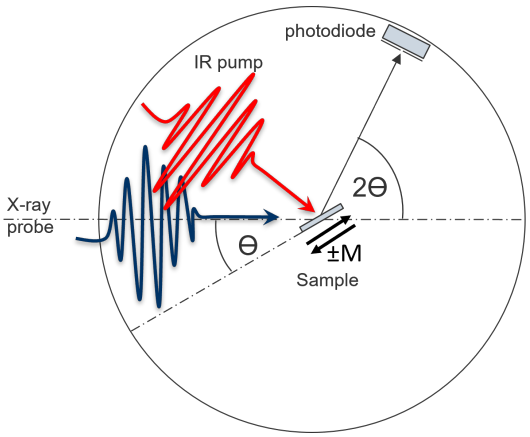

Figure 4.2: *Sketch of the experimental setup. The sample is mounted on a rotatable manipulator in the rotational center of the scattering chamber at an angle of θ to the incident X-ray beam. The IR-pump pulse is incident almost collinear to the X-ray-probe pulse. The deviation is an angle of* 1.5° *perpendicular to the scattering plane. After scattering off the sample, the probe pulse is detected by a photodiode at an angle of 2θ, while the pump pulse is blocked.*

isolated Gd. The sample is a 60 nm thick Gd film grown on a W(110) substrate and magnetized in plane, as shown by the easy-axis hysteresis in Fig. 4.1, that was measured with the magnetic field in the sample plane. For more details on the sample preparation, see Sec. 3.6.

The experimental setup is shown in Fig. 4.2. Our sample is mounted on a rotatable sample holder at the center of the scattering chamber at an angle of $\theta = 4°$ to the incident X-rays. With an IR-pump pulse with a wavelength of 800 nm we excite the system. The X-ray pulse probes the sample and is specularly reflected at an angle of $2\theta = 8°$. It is detected in an avalanche photodiode when in slicing mode. This enhances the signal to compensate the considerable loss of intensity during the slicing process. If the slicing process is not active, we speak of the picosecond mode (ps-mode), due to the natural picosecond time resolution of the X-ray pulses. In that case, a silicon photodiode is sufficient to detect our signal. The pump beam has an angle of 1.5° to the X-ray beam in the vertical direction. In this way the laser beam that is reflected off the sample hits a beam blocker slightly above the photodiode which protects it from the intense light.
The sample is located in a superconducting vector magnet which allows the application of magnetic fields up to 1.5 T in variable directions. For our dynamic experiments we applied a field strength of ±100 mT along the X-ray beam direction.

Before we get to the time-resolved data, we will start with some preparatory

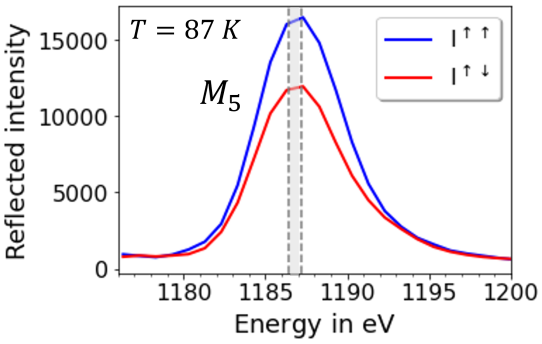

Figure 4.3: *X-ray reflectivity at the Gd M_5 edge for $T = 87$ K. The spectrum was measured at the FemtoSpeX beamline in slicing mode and is therefore energy broadened. The grey area marks the energy uncertainty range in which the dynamic data were recorded. The labels $I^{\uparrow\downarrow}$ and $I^{\uparrow\uparrow}$ denote the orientation of the external magnetic field either antiparallel or parallel to the X-ray photon momentum, respectively.*

considerations. Firstly, we will describe the acquisition of the data as well as their treatment and evaluation procedure in Sec. 4.1. Secondly, we will present a simulation of the optical properties of the film in Sec. 4.2, which will be useful for the understanding of our experimental results.
Finally we will look into the dynamics of the Gd film, that show a distinct lack of an ultrafast timescale in Sec. 4.3. Our results indicate that effects at the Gd-W interface are indeed responsible for the emergence of this ultrafast timescale in previous works.

4.1 Data acquisition and treatment

The energy-dependent X-ray reflectivity is shown in Fig. 4.3. The slicing setup introduces a somewhat variable energy offset. In order to correct the position of the M_5 edge, it was compared to a spectrum simulated in the DYNA software, which is described in Subsec. 3.5.1. The uncertainty of the energy stems from this comparison.
For time-resolved measurements the incident X-ray photon energy was set to (1186.8 ± 0.4) eV, at which the peak of the M_5 edge was observed. The uncertainty stems from the use of slightly different probing energies used throughout the experiment. X-ray photons reflected off the sample were recorded with an avalanche photodiode (APD) operated close to the breakthrough voltage. This allows for single-photon counting. To optimize the required time for data acquisition, we need to consider several factors. Firstly, because of interference effects, the overall reflected intensity exhibits Kiessig fringes as discussed in Sec. 3.3. Secondly the intensity diminishes significantly for increasing incidence angles, so it is convenient to work in grazing incidence. Lastly, the magnitude of the XMCD effect at the resonant absorption edge varies with incidence angle. An optimal dichroic signal was found for an incidence angle of 4°.
Each data point of the time-resolved measurements represents an integration time of 20 s.

4.1.1 Calculating XMCD

As was described in Sec. 3.4, it is necessary to switch the magnetic field direction to obtain the XMCD contrast as a measure of the sample magnetization. Additionally we introduced in Subsec. 3.1.1 that the pumped and unpumped sample are being measured alternatingly in the slicing setup with a probe repetition rate of 6 Hz and a pump repetition rate of 3 Hz.
Therefore we have 4 signals to work with: $I_{up}^{\uparrow\uparrow}$ and $I_{p}^{\uparrow\uparrow}$ for the unpumped and pumped signals in the parallel alignment of photon spin and sample magnetization, $I_{up}^{\uparrow\downarrow}$ and $I_{p}^{\uparrow\downarrow}$ for the antiparallel alignment, respectively.
The XMCD contrast does not give us the absolute magnetization, but it is proportional to it. We will therefore normalize the XMCD contrast in the equilibrium state, before the pump pulse arrives, to 1 and look at relative changes. This is accomplished by the following relation as a function of the delay time t

$$\mathrm{XMCD}(t) = \frac{(I_{p}^{\uparrow\downarrow}(t) - I_{up}^{\uparrow\downarrow}(t) + \overline{I_{up}^{\uparrow\downarrow}}) - (I_{p}^{\uparrow\uparrow}(t) - I_{up}^{\uparrow\uparrow}(t) + \overline{I_{up}^{\uparrow\uparrow}})}{\overline{I_{up}^{\uparrow\downarrow}} - \overline{I_{up}^{\uparrow\uparrow}}} \ , \tag{4.1}$$

where the bar above denotes the average of the unpumped signal over all delay times. The use of the differences between pumped and unpumped signal at delay t smoothes out fluctuations.
The uncertainty is computed as the square root of the signal counts for each channel $I_{p}^{\uparrow\downarrow}$, $I_{up}^{\uparrow\downarrow}$, $I_{p}^{\uparrow\uparrow}$, $I_{up}^{\uparrow\uparrow}$ and enters a Gaussian error propagation to obtain the uncertainty of the XMCD.

4.1.2 Fit model

In order to get a quantitative handle on the observed processes, we fit a phenomenological model to the data. We assume three exponential functions, that set in at a time $t' = 0$: two exponential decay functions with time constants τ_1 and τ_2 and prefactors M_1 and M_2, as well as one recovery function with time constant τ_3 and prefactor M_3 respectively, reading

$$M'(t') = (M_1 + M_2)\Theta(-t') + \Theta(t')\left(M_1 \mathrm{e}^{-\frac{t'}{\tau_1}} + M_2 \mathrm{e}^{-\frac{t'}{\tau_2}} + M_3(1 - \mathrm{e}^{-\frac{t'}{\tau_3}})\right) \ . \tag{4.2}$$

$\Theta(t')$ is the Heavyside step function. It causes the decay behavior to start just at the arrival of the pump pulse and keeps the value $M_1 + M_2$ before.
To account for broadening effects due to the pulse lengths of pump and probe, the function is convolved with a Gaussian. The time resolution of the experiment is given by the Gaussian width $\sigma = 150$ fs. After normalization we obtain the following fit model

$$
\begin{aligned}
M(t) = M_0 + \frac{1}{2}\Bigg[& M_1 e^{\frac{\sigma^2}{2\tau_1^2}} e^{-\frac{t}{\tau_1}} \operatorname{Erfc}\left(\frac{\sigma^2 - t\tau_1}{\sigma\sqrt{2}\tau_1}\right) \\
& + M_2 e^{\frac{\sigma^2}{2\tau_2^2}} e^{-\frac{t}{\tau_2}} \operatorname{Erfc}\left(\frac{\sigma^2 - t\tau_2}{\sigma\sqrt{2}\tau_2}\right) \\
& - M_3 e^{\frac{\sigma^2}{2\tau_3^2}} e^{-\frac{t}{\tau_3}} \operatorname{Erfc}\left(\frac{\sigma^2 - t\tau_3}{\sigma\sqrt{2}\tau_3}\right) \\
& + M_3 \left(1 + \operatorname{Erf}\left(\frac{t}{\sigma\sqrt{2}}\right)\right)\Bigg] \\
& + (M_1 + M_2)\frac{1}{2} \operatorname{Erfc}\left(\frac{t}{\sigma\sqrt{2}}\right) . \qquad (4.3)
\end{aligned}
$$

The normalization is chosen such that the magnetization level before time zero is $M_0 + M_1 + M_2$, while for very long times the recovery level $M_0 + M_3$ is reached. The Gaussian width is included as σ and the delay by t. The variable M_0 allows for an offset along the relative-magnetization axis.

4.2 Pump-probe penetration depth

When we record the dichroic signal of a sample it is easy to assume that it gives a complete view of the sample magnetization. But we need to remember that photons have a finite penetration depth in the material. The absorption depends on the complex refractive index of the medium at the appropriate wavelength and is therefore different for the pump and probe photons.
In the following we will first simulate the intensity profile of the IR-pump beam in the 60 nm film as well as in the 10 nm film used by Bobowski *et al.* [20]. Values referring to the latter will be given in brackets. Then we are able to calculate the absorbed intensity as a function of the depth within the film. This allows us to get a grasp at where the pump effect is stronger or weaker.
In the second subsection we will equivalently simulate the intensity profile of the X-ray-probe beam. Thus we can calculate the penetration depth to judge the sensitivity of the experiment to different sample regions.

4.2.1 The IR-pump pulse

To make our work comparable, we would like to state the amount of energy that excites the dynamic processes, as it determines how far out of equilibrium the system is driven.
For this purpose one usually considers the fluence F, given as the energy per unit area. The incident fluence F_{in} can be determined from the laser repetition rate R_{laser}, the beam power P_{beam} and the spot size on the sample A_{spot} as

$$F_{in} = \frac{P_{beam}}{R_{laser} A_{spot}} \ . \tag{4.4}$$

The absorbed fluence F_a however, is much harder to obtain, as it is influenced by the photon energy and incidence angle of the pump pulse as well as the thickness and chemical make-up of the layer. When dealing with thin films as in our case, one must take the issue of multiple reflections into account as well. The problem was discussed for X-rays already in Sec. 3.3. One solution is realized with the simulation software IMD by David Windt, explained in detail in his 1998 paper [79]. It was used in conjunction with the XOP (X-ray Oriented Programs) driver software, developed by Manuel Sanchez del Rio and Roger J. Dejus [88].
IMD calculates the reflectance r, transmittance t and absorptance a of a given multilayer. For $j = r, t, a$ they are defined as

$$j = \frac{\phi_j}{\phi_i} \tag{4.5}$$

with the reflected, transmitted or absorbed flux ϕ_j and the incident flux ϕ_i in units of power per area. Since our substrate is assumed to be infinitely thick, which is a reasonable assumption for a thickness on the order of several millimeters, we will change the denomination. Instead of the transmittance t, we will speak of the substrate absorptance a_s. The film absorptance will be called a_f.
IMD uses a recursive approach to calculate the reflectance, substrate absorptance and film absorptance layer by layer to eventually obtain these figures for the total film. It works with the complex index of refraction given on the left side of Eq. 3.3 as

$$n = n' - i\kappa \ .$$

In order to simulate the film properties in the infrared regime, we use the tabulated complex refractive indices found in the ‚Handbook on optical constants of metals' by Adachi [89]. For Gd the indices were measured with the electric field parallel to the c-axis of a single crystal sample at a temperature of 4.2 K. For p-polarized light, as in our experiment, this corresponds to an incidence direction parallel to the film with $\theta = 0°$. Our grazing incidence at $\theta = 4°$ is very close to this setup.

In Fig. 4.4 (Fig. 4.5) we see the electric-field intensity profile for the 60 nm (10 nm) Gd film. We simulate $\lambda = 800$ nm light incident at an angle of 4° (4.5°) with respect to the sample surface. The underlying W substrate is semi-infinite. The left-hand side of the figure shows the logarithm of the resulting field intensity. About 51% (38%) of the light is reflected. The linear decay within the film on this scale illustrates the Lambert-Beer law for absorption.

In the next step, we calculate the absorbed intensity in each layer, by integrating the relation [90]

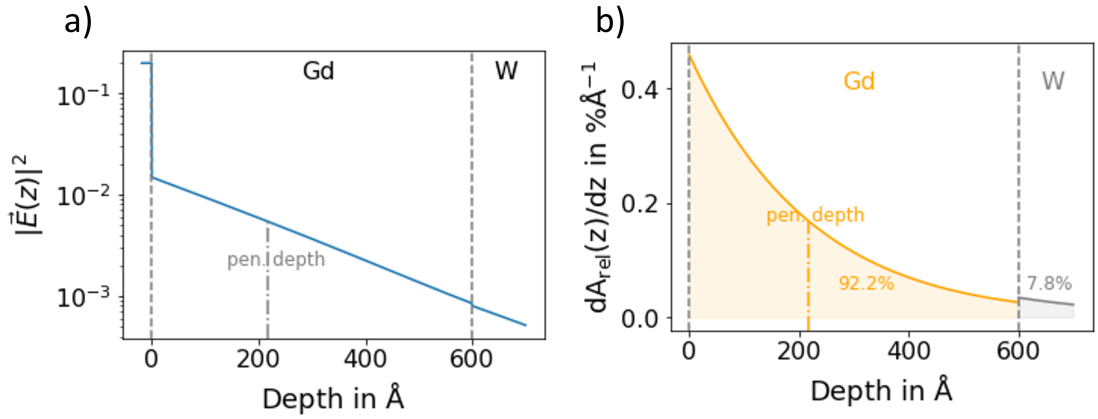

Figure 4.4: *a) Field intensity $|\vec{E}(z)|^2$ of the pump pulse as a function of depth in the 60 nm Gd film on a semi-infinite W(110) substrate. The incidence angle is 4°. Note the logarithmic scale of the intensity.*
b) Absorption profile in the Gd film on a semi-infinite W substrate. The total absorption ratio is given in the shaded area and refers to the total ***absorbed*** *fluence. The penetration depth at which the intensity has dropped by a factor of $1/e$ is marked by the dash-dotted lines.*

$$dA(z) = \alpha(z)n'(z)|\vec{E}(z)|^2 dz \tag{4.6}$$

over dz. Here we use the real part of the refractive index $n'(z)$, the absorption coefficient $\alpha(z) = 4\pi\kappa(z)/\lambda$, which contains the imaginary part of the refractive index $\kappa(z)$ and the field intensity $|\vec{E}(z)|^2$. The parameter z gives the depth in the sample. Only the field intensity varies continuously with z, while the refractive index is assumed to change abruptly at the interface for the purposes of Eq. 4.6. The absorptance of the Gd film is found to be $a_f = 0.45$ ($a_f = 0.20$). The substrate absorptance is $a_s = 0.038$ ($a_s = 0.42$). The absorption profile within the layer is shown in Fig. 4.4 b) (Fig. 4.5 b)). It shows the relative absorption per unit length $dA(z)/dz$, which is proportional to the integrand of Eq. 4.6. For one specific layer i of a multilayer film it is generally given by

$$dA_{i,rel}(z)/dz = \frac{\alpha_i(z)n_i'(z)|\vec{E}(z)|^2}{A_{total}} \frac{a_f}{a_f + a_s} \tag{4.7}$$

with the sum of the layer integrals

$$A_{total} = \sum_i A_i \ . \tag{4.8}$$

Each A_i is obtained from integrating Eq. 4.6 for the respective layer, excluding the substrate.
For the W substrate the similar relation

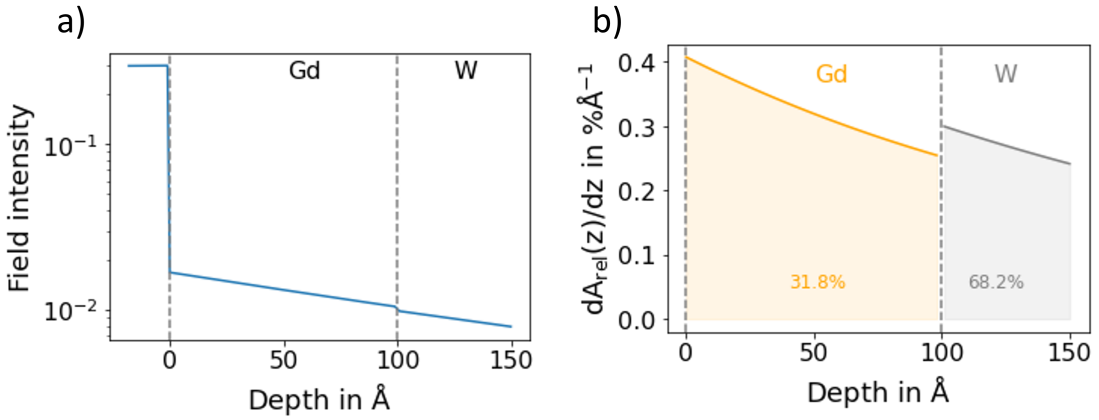

Figure 4.5: *a) Field intensity $|\vec{E}(z)|^2$ of the pump pulse as a function of depth in the* 10 nm *Gd film on a semi-infinite W(110) substrate. The incidence angle is* 4.5°*. Note the logarithmic scale of the intensity.*
b) Absorption profile in the Gd film on a semi-infinite W substrate. The total absorption ratio is given in the shaded area and refers to the total ***absorbed*** *fluence. The penetration depth at which the intensity has dropped by a factor of $1/e$ is larger than the film thickness.*

$$dA_{s,rel}(z)/dz = \frac{\alpha(z)n'(z)|\vec{E}(z)|^2}{A_W}\frac{a_s}{a_f + a_s} \tag{4.9}$$

applies. The integral over the W substrate A_W cannot be computed numerically, as the substrate is infinitely thick. Instead we determine the parameters of the exponential function $|\vec{E}(z)|^2$ within W from the IMD simulation and compute the integral analytically.
Additionally, Fig. 4.4 (Fig. 4.5) shows the full relative integral value A_i in percent. Note again that it states the distribution of the absorption within the sample and as such is not referred to the incident power, but the absorbed portion of the power only. About 92% of the absorbed power is deposited in the Gd film and only a minor contribution of ca. 8% in the W substrate. In the case of the 10 nm Gd film, the situation is significantly changed. About 32% of the absorbed power is deposited in the Gd, but a larger portion of 68% is absorbed in the W substrate. We see that in the thinner film, the substrate will be excited to a much larger degree than in the thick one. Furthermore, the absorption per unit length is still comparatively high at the bottom of the 10 nm Gd layer. Interface effects between film and substrate can thus be assumed to play a larger role there.

4.2.2 The X-ray-probe pulse

We would like to judge the depth sensitivity of our experimental data as well. The reflected intensity is a result of all X-ray interactions within the sample. If an interaction takes place in the depth z, the intensity $|\vec{E}(z)|^2$ is changed to $|\vec{E}(z) - \Delta\vec{E}(z)|^2$, which then contributes to the reflected intensity. If we assume that

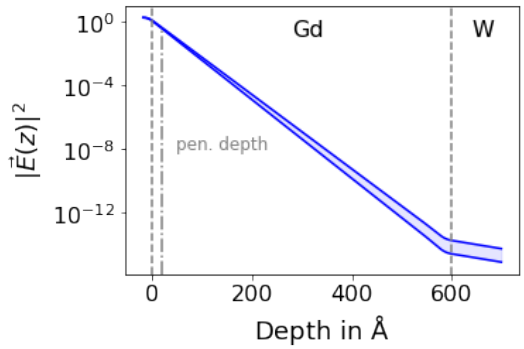

Figure 4.6: *Intensity profile of a X-ray beam with a photon energy of* (1186.8 ± 0.4) eV *incident at an angle of* $\theta = 4°$ *on a* 60 nm *Gd film on top of a semi-infinite W substrate. The lines show simulations for the energies at the limits of the photon energy's uncertainty interval. The shaded area indicates the range in between. Depth is measured along the surface normal. The penetration depth at which the intensity has dropped by a factor of* $1/e$ *is marked by the dash-dotted line on the left.*

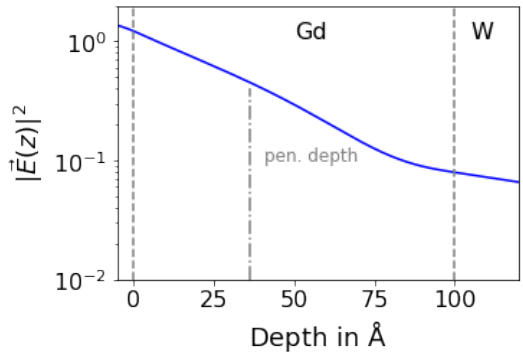

Figure 4.7: *Intensity profile of a X-ray beam with a photon energy of* 1186.4 eV *incident at an angle of* $\theta = 4.5°$ *on a* 10 nm *Gd film on top of a semi-infinite W substrate. Depth is measured along the surface normal. The penetration depth at which the intensity has dropped by a factor of* $1/e$ *is marked by the dash-dotted line on the left.*

$\Delta\vec{E}(z)$ is a small perturbation, each contribution is approximately still proportional to $|\vec{E}(z)|^2$. The intensity profile can thus give us an idea of the depth sensitivity. We have already discussed that X-rays will be absorbed in the sample. In the simple case of a single elemental layer, this always leads to an exponential intensity profile, as in Eq. 3.6. The length scale is given by the photon-energy dependent absorption coefficient in Eq. 3.7. We make use of IMD to take multiple reflections and interference effects into account, which will proof especially prudent for the multilayer in Ch. 6.

The simulation shown in Fig. 4.6 (Fig. 4.7) illustrates the exponential decay of the electric field intensity within a 60 nm (10 nm) Gd film. The energy was chosen at the peak of the M_5 absorption edge with (1186.8 ± 0.4) eV (1186.3 eV). An energetic broadening due to the femto-slicing process, see Subsec. 3.1.1, needs to be applied to the refractive index. This reduces the absorption of X-rays within the layer. We determined a Gaussian energy broadening of (2.0 ± 0.2) eV ((4.8 ± 0.3) eV) for the 60 nm (10 nm) Gd film[1]. For this we compared an artificially braodened energy spectrum, that was simulated with DYNA for the experimental parameters, with an experimental energy spectrum.
Following the exponential decay of the field intensity, we find a $1/e$ penetration depth of (18.0 ± 0.5) Å ((36 ± 2) Å).

[1]Note that this is a Gaussian width. Thus (2.0 ± 0.2) eV are comparable to the FWHM of 12 eV given in Bobowski *et al.* [20]

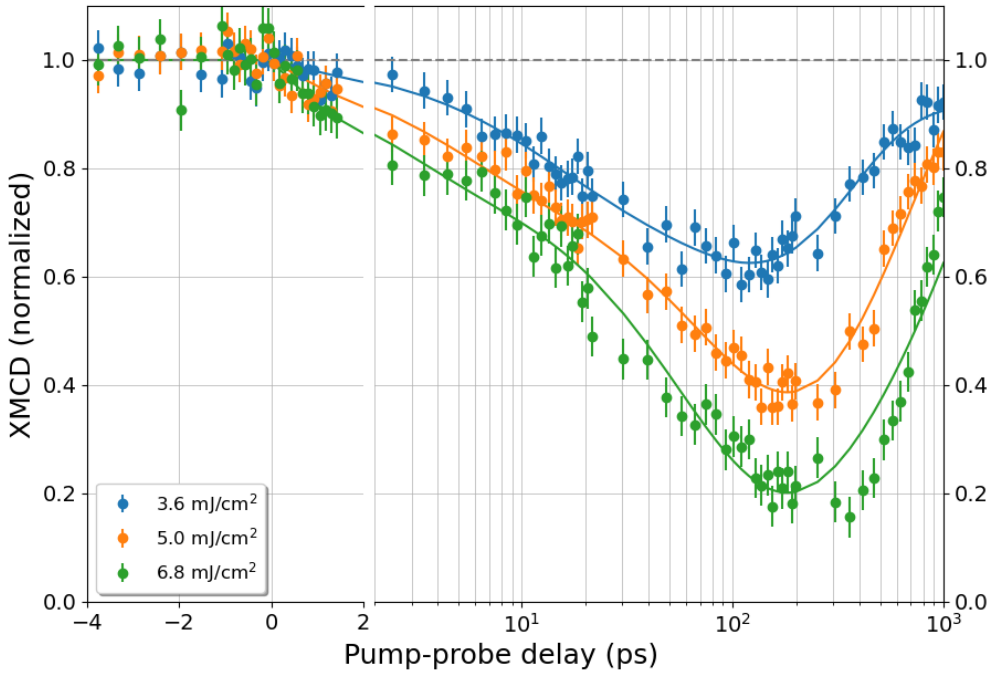

Figure 4.8: *Magnetization dynamics of a* 60 nm *Gd film, measured at the* M_5 *absorption edge at an energy of* 1186.8 eV *for three fluences, absorbed in Gd.*

In order to detect the magnetic response to the pump pulse, the probe pulse must propagate fully within the pumped volume. We can make an estimate to check if this is the case. Both, pump and probe beam, are incident at an angle of $\Theta = 4°$ ($\Theta = 4.5°$) with respect to the sample surface. Using Snell's law, we find that the pump beam travels at an angle of $\Theta'_{pump} = 66.5°$ within the Gd film and the probe beam at an angle of $\Theta'_{probe} = 1.7°$ ($\Theta'_{probe} = 2.7°$). On the one hand, the pump beam changes its lateral position by merely 26 nm (4.4 nm) within a film thickness of 60 nm (10 nm). The lateral travel of the probe beam, on the other hand is about 2022 nm (212 nm). The typical beam diameter is on the order of 100 μm. In addition to that, the grazing incidence causes the spot on the sample to be strongly elongated in the lateral direction. We can therefore safely assume that the probe beam does not leave the pumped volume.

4.3 Magnetization dynamics

At the resonance peak (1186.8 eV) we recorded the Gd dynamics for a series of three fluences. The values in Fig. 4.8 state the absorbed fluence in the Gd film according to the IMD simulation in Fig. 4.4. The incident fluences were 8 mJ/cm^2, 11 mJ/cm^2 and 15 mJ/cm^2, respectively.
We use the fit function presented in Eq. 4.3. It is necessary to reduce the amount

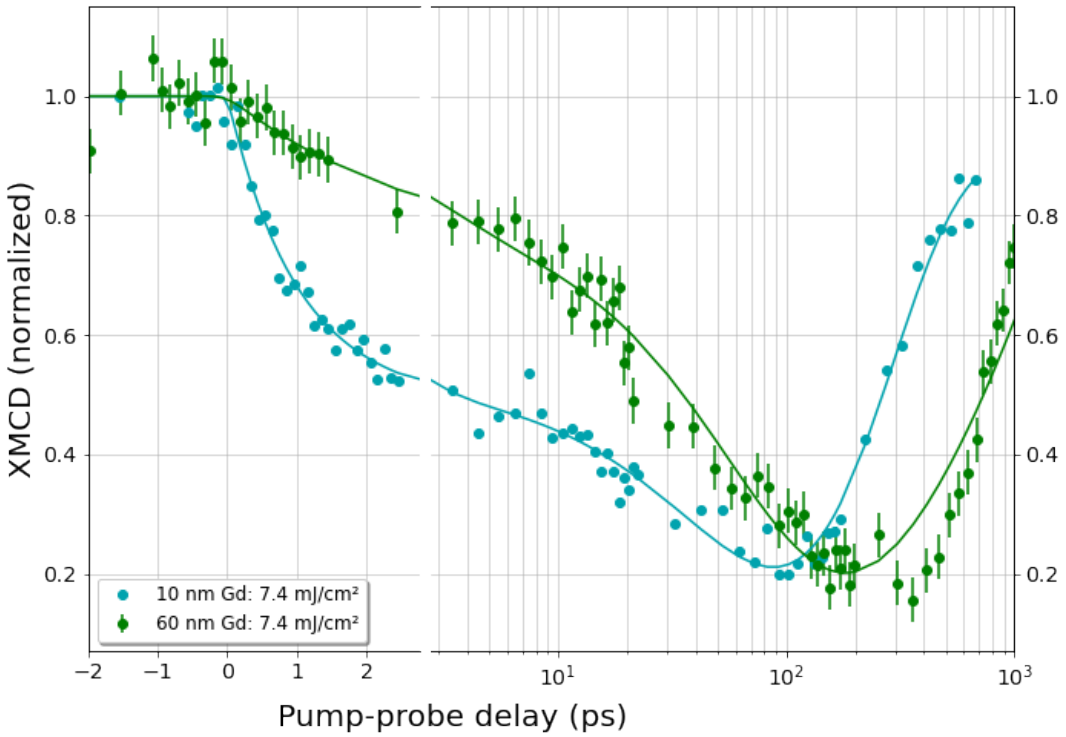

Figure 4.9: *Comparison of the magnetization dynamics of our* 60 nm *Gd film with the* 10 nm *Gd film investigated by Bobowski et al. [20]. The latter was measured at the M_5 absorption edge at an energy of* 1186.3 eV. *The given fluences here are those absorbed in Gd and W for both layers. In Fig. 4.8 and Tab. 4.1 this is the* 6.8 mJ/cm^2 *dataset of the* 60 nm *film. Despite uncertainties in the comparability of the two fluence values, the maximum demagnetization levels are comparable and thus the total energy intake per probed volume of both films.*

of free parameters to minimize the correlations between them. The Gaussian width was set to $\sigma = 150$ fs as the standard time resolution assumed for the setup. We further fix the offset $M_0 = 0$ and set $M_1 = 0.2$ as well as $M_2 = 0.8$. The values for M_1 and M_2 result from preliminary fits with free parameters.
It is immediately apparent that the magnetization changes only marginally within the first picoseconds. This is reflected in the timescales listed in Tab. 4.1. The fast timescale amounts to a few picoseconds, while the slow timescale is on the order of tens of picoseconds to a hundred picoseconds. After 1000 ps, the magnetization recovers to $70 - 90\%$ of the initial value.
With increasing fluence, the demagnetization increases and the timescales decrease. Figure 4.9 shows the dynamics of a 10 nm [20] and a 60 nm Gd film in comparison for similar fluences at which equivalent demagnetization is reached. Note the ultrafast timescale that is absent in the dynamics of the 60 nm Gd film. Appendix B shows equivalent comparisons for the fluences 3.6 mJ/cm^2 and 5.0 mJ/cm^2 that were presented in Bobowski's PhD thesis [91].
The absorbed fluence stated by Bobowski *et al.* [20] is that absorbed in Gd and W combined. In Fig. 4.9 we state the same for the 60 nm Gd film. The absorbed fluences in the Gd layer only are (2.6 ± 0.2) $\frac{\text{mJ}}{\text{cm}^2}$ in 10 nm and 6.8 $\frac{\text{mJ}}{\text{cm}^2}$ in 60 nm

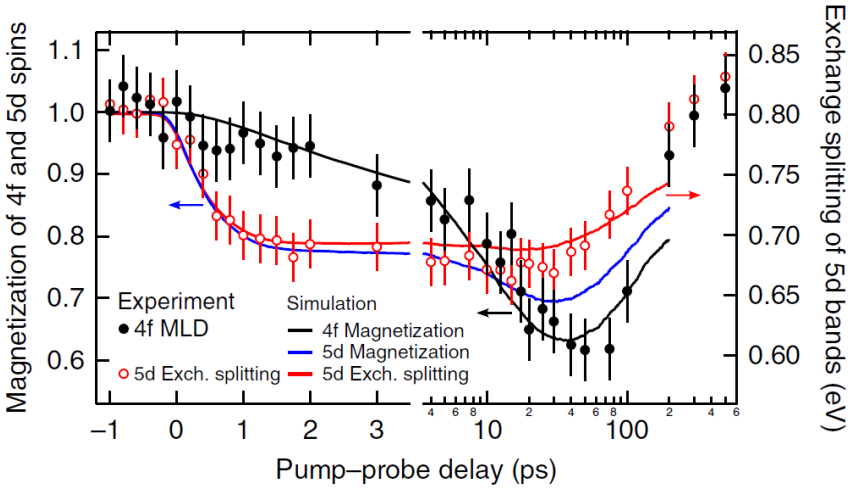

Figure 4.10: *Disparate magnetization dynamics of the* $5d6s$ *and* $4f$ *electron spins: The magnetic linear dichroism observed in the occupied* $4f$ *state of Gd is depicted in black and decays with a time constant of* 14 ps*. Red dots show the change of the exchange splitting of the* $5d$ *band with a time constant of* 0.8 ps*. The image is taken from Frietsch et al. [2]*

respectively, which we can estimate from the reflectance observed by Bobowski *et al.* and an IMD simulation. But it is arguably more useful to look at Gd and W combined, because we assume that the demagnetization is mainly caused by magnons in the Gd film that are driven by an effective spin current across the Gd/W interface.

F_a(mJ/cm^2)	τ_1 (ps)	τ_2 (ps)	τ_3 (ps)
3.6	11.0 ± 1.1	100.5 ± 6.4	222 ± 16
5.0	4.30 ± 0.55	97.1 ± 3.5	685 ± 76
6.8	2.34 ± 0.56	66.2 ± 3.4	1360 ± 580

Table 4.1: *Resulting fit parameters for the magnetization dynamics at a probing energy of* 1186.8 eV *and an incidence angle of* 4°*.*

4.3.1 Spin currents, spin polarization & 4f dynamics

The slower response in the 60 nm film, measured with XMCD, mirrors the response of the $4f$ electrons observed with ARPES [2], which is shown together with the dynamic response of the $5d6s$ band in Fig. 4.10. Both experiments probe the magnetization from sample regions that are distant from the W(110) substrate. In ARPES experiments this is the case because the probing depth is limited by the mean free path of electrons, which is only a few nanometers at the relevant electron energies. These experiments therefore show the intrinsic $4f$ magnetization dynamics of isolated Gd, excluding external effects. Both the excitation profile in Fig. 4.4 and the small penetration depth of the probe beam in Fig. 4.6 support this picture for the 60 nm Gd film.

In the case of the XMCD study of the 10 nm film by Bobowski et al., we find a different situation. The penetration depth in this experiment was larger as shown in Fig. 4.7, because of the larger energetic width of the probing beam, and the film was thinner. The probe signal is therefore more strongly influenced by the magnetization close to the Gd/W interface. Furthermore the excitation profile in Fig. 4.5 clearly shows that electrons in the W substrate absorb 60% of the energy and thus possess a high electron temperature.
A sub-picosecond timescale in the Gd demagnetization, as observed in the 10 nm film (0.75 ps), can thus be attributed to probe regions near the substrate. Other sources of sub-picosecond dynamics can be excluded in the 10 nm Gd film, as they would apply to the 60 nm film as well:
As we have discussed before, spin-lattice coupling is negligible on such short timescales due to the orbital angular momentum quantum number $L = 0$ of Gd. This can also be seen in the magneto-crystalline anisotropy energy, which is three orders of magnitude smaller in Gd than in Tb. In the latter an effective coupling of $5d$ excitations to the $4f$ magnetization is driven via lattice degrees of freedom [92]. Likewise, we do not expect $4f$ electronic excitations via $5d - 4f$ scattering as reported for Tb metal [93]. The first electronic excitation of the $4f$ state has an energy of 4.1 eV, far above our pump energy. [93]

A combination of spin-resolved photoemission (published in [84]) and terrahertz emission experiments by Gückstock *et al.* (in preparation) has shown that the spin transport in Gd is mainly driven by magnons instead of electrons. Their photoemission experiments show that in Gd there is no difference in the lifetimes of excited majority and minority spin electrons, which prevents electron driven spin transport.
In the THz emission experiments, they investigated a Gd/Pt sample. Hot electrons from the Pt substrate are reflected at the Gd/Pt interface in a spin flip scattering event. This launches a magnon in the adjacent Gd layer. Due to the similarity of the heavy metals Pt and W, the same can be expected in the case of a 60 nm Gd film on W. Because the lattice constants of W and Gd are closely matched, W electrons may penetrate a few layers into the Gd film. Because these electrons are not spin polarized, they decrease the spin polarization in Gd, leading to an additional demagnetization channel in experiments that are sensitive to the interface region, as is the case for the 10 nm Gd film that Bobowski *et al.* investigated [20]. The timescale of that electronic demagnetization is short due to the large electron velocities of around 300 nm/ps close to the Fermi edge.
The magnons which are generated close to the interface, however, may travel through the entire film and are detectable even close to the surface of a 60 nm film. Dissipation of energy from the magnon system to the phonon system must be mediated by spin-orbit coupling, as it is the connection between electronic spins and space. Here the very small SOC in Gd comes into play once more by preventing that energy dissipation. We can therefore expect the lifetimes and hence the mean free paths of magnons in Gd to be long.
Magnons do not need to be created at the Gd/W interface, but can be created anywhere in the Gd film, e.g. after an initial excitation of $5d6s$ electrons. This

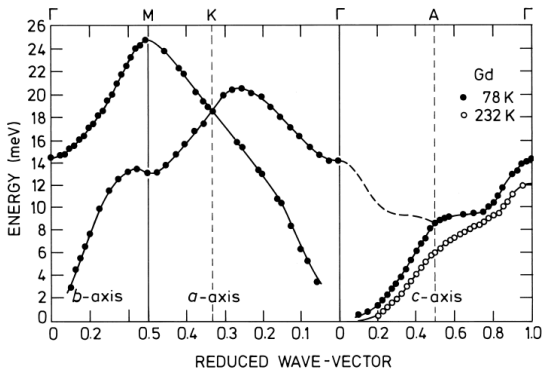

Figure 4.11: *Magnon dispersion for Gd. A propagation towards the Gd surface in our experiments corresponds to the A point along the $\Gamma - A$ direction. The image is taken from Jensen and Mackintosh [94]*

can lead to an equivalent spin transport out of the probing region and is arguably more likely, due to the weak excitation at the Gd/W interface seen in Fig. 4.4. Now we take a look at the magnon dispersion to get an estimate for the timescale that is to be expected from a magnon induced reduction of the magnetization. We consider the dispersion close to the A point along the $\Gamma - A$ direction in the Brillouin zone (see Fig. 4.11). It describes the propagation direction from the Gd/W interface to the Gd surface. The magnon group velocity is given by

$$v_g = \frac{\partial \omega}{\partial k} \tag{4.10}$$

with the wave number k and the magnon frequency $\omega = E/\hbar$, given by the magnon energy E. A simple estimate gives us $v_g \approx 2 - 3$ nm/ps. We conclue that magnons reach the surface of the Gd layer on the faster timescale τ_1 observed in the 60 nm Gd film (see Tab. 4.1). It is in turn the slow timescale reported by Frietsch *et al.* for the $4f$ magnetization dynamics (14 ps) [2] and by Bobowski *et al.* in XMCD in reflection for 10 nm Gd (26 ps) [20]. We believe that the slow demagnetization given by τ_2 in Tab. 4.1 shows the dissipation of angular momentum to the phonon system. Our investigation further shows that for increasing pump fluence, the τ_1 becomes shorter. This is compatible with the magnon picture. The number of magnons n_i at an energy E_i follows the Bose-Einstein distribution:

$$n_i = \frac{1}{\mathrm{e}^{\frac{E_i}{k_B T_m}} - 1} \ . \tag{4.11}$$

An increase of the magnon temperature T_m, e.g. through a higher pump fluence, creates magnons at larger energies and therefore larger velocities, as shown in Fig. 4.11. And it increases the overall number of magnons. An increase of the maximum magnon velocity would lead to a reduction of the demagnetization timescale in our picture. While the increase of the number of magnons would lead to stronger demagnetization. Both effects can be seen in our experiment.

One might wonder how the scattering of itinerant W electrons in the Gd layer leads to the creation of magnons and how these magnons affect the magnetic moments of the localized $4f$ electrons.

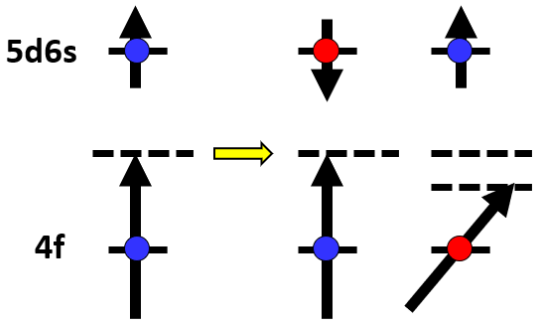

Figure 4.12: *Sketch of $4f$ and $5d$ spin levels. A change of the magnetic moment in the $5d6s$ and $4f$ system is described as a superposition of a change in either of the subsystems.*

Discussions by A. Melnikov, T. O. Wehling, A. I. Lichtenstein and M. I. Katsnelson lead to the physical picture shown in Fig. 4.12. The Gd atom is initially in the ground state Ψ_0, given in Eq. 4.12, where the first number is the magnetic quantum number of the $4f$ electrons and the second that of the $5d6s$ electrons. If both systems are entangled, the reduction of the total spin by 1 μ_B can be visualized in two microscopic ways. Either the $5d6s$ electron experiences a spin flip, or the $4f$ electron a spin flop[2]. These states form a coherent superposition of the electronic states as the excited state Ψ_e, as given in Eq. 4.13. The dephasing time of the superposition was estimated on the order of tens of femtoseconds, below the time resolution of experiments undertaken so far.

$$|\Psi_0\rangle = |\frac{7}{2}, \frac{1}{2}\rangle \tag{4.12}$$

$$|\Psi_e\rangle = \alpha\,|\frac{7}{2}, -\frac{1}{2}\rangle + \beta\,|\frac{5}{2}, \frac{1}{2}\rangle \tag{4.13}$$

An excitation of the $5d6s$ electron spin as given by the first term in Eq. 4.13 can be caused by a scattering event with a W electron. Once the coherent state Ψ_e is created, it collapses within the dephasing time as mentioned above. The prefactors α and β determine the probability with which the coherent state collapses to either of the two constituent states. It is thereby possible to cause a $4f$ excitation via itinerant electrons, explaining the imprint of $5d6s$ magnetization dynamics onto the XMCD signal that probes the $4f$ state, despite the breakdown of the intra-atomic exchange interaction on the ultrafast timescale reported by Frietsch *et al.* [2]. In the same fashion this leads to the creation of magnons.

4.4 Conclusion

In contrast to Bobowski *et al.* [20] we do not observe a sub-picosecond demagnetization. We attribute such fast timescales to short ranged electronic spin-transport across the Gd/W interface, which we are insensitive to.

[2] I.e. a change of the spin orientation that is not a flip. Here from $m_s = 7/2$ to $m_s = 5/2$.

Our findings are in line with the results obtained by ARPES studies of the $4f$ and $5d$ spin systems [2] as well as recent spin-resolved photoemission and terraherzt emission experiments by Gückstock *et al.* (in preparation). In a 60 nm Gd/W film, we observe a demagnetization on a ps-timescale and attribute it to magnons that are generated at the Gd/W interface due to interfacial electron transport. This timescale corresponds to the slow timescale observed by Frietsch *et al.* in the $4f$ MLD [2] and by Bobowski *et al.* in the XMCD contrast [20]. Because our experiment is sensitive to the localized $4f$ magnetic moments which are unaffected by electronic transport, these results show that a coherent superposition of $4f$ and $5d$ spin states has to be assumed.

Our findings have implications not only for our understanding of the magnetization dynamics in Gd, but also in alloys of Gd and $3d$ metals. As mentioned in Sec. 2.3, these alloys are the prototype systems for all-optical switching.
Theoretical descriptions of AOS rely on Landau-Lifshitz-Bloch equations [63, 66, 95, 96] and the M3TM [65], which commonly treat the complex multi-sublattice systems of rare-earth and transition metal as composites of a single $3d$ and a single magnetic system based on $5d$ and $4f$ states.
The mechanism for AOS in synthetic ferrimagnets, i.e. ferrimagnetic bilayers, was described as exchange scattering between transition and rare-earth metal electrons by Beens *et al.* [7]. Our findings suggest that electronic scattering and transport mechanisms play a role mainly over short distances, while magnonic spin currents are the major driving force of AOS over larger distances both in ferrimagnetic alloys and bilayers containing Gd. This will be discussed further in Ch. 6.

Chapter 5

Equilibrium investigation of Y/Fe/Gd

Before we can discuss the experiments on magnetization dynamics in the next chapter, it is imperative to characterize the samples in thermal equilibrium. Experimentally these investigations were undertaken after the dynamics experiments, presented in Ch. 6, because the latter must be performed on a fresh sample.
We will start the equilibrium characterization with modelling the magnetic moments within the sample in Sec. 5.1, because it offers valuable insights for the interpretation of the experimental data. In Sec. 5.2 we likewise simulate the X-ray penetration depth of the probe beam to estimate the sensitivity of the experiment. Secs. 5.3 and 5.4 discuss insights about the magnetic structure from experiments that were performed at the PM3 beamline of BESSY II. In Sec. 5.3 we will extract information from magnetic hystereses, while Sec. 5.4 deals with the structural and magnetic depth profiling through XRMR, a method described in Sec. 3.5.

We find clear signatures of the twisted state as described in Sec. 2.2. Our hysteresis analysis shows that the magnetizations of the Fe and Gd layers align almost perpendicularly to the external magnetic field. Additionally the magnetic depth profiling, described in Sec. 3.5, reveals the presence of a spatial variation of the magnetic orientation within the Gd layer.

5.1 Balance of magnetic moments

Both Fe and Gd are ferromagnets. When brought into contact, the exchange constant between neighboring Fe and Gd atoms can be assumed as -3.25 meV [3], which results in a preferred antiparallel alignment of their magnetic moments. The magnetic moment per atom in bulk Fe is 2.2 μ_B, while that of bulk Gd is 7.55 μ_B [97]. If we assume both layers to behave independently as their bulk materials, except for their overall antiferromagnetic alignment due to the interface interaction, we obtain a ferrimagnet.
What is more, the magnetizations of Fe and Gd exhibit different temperature

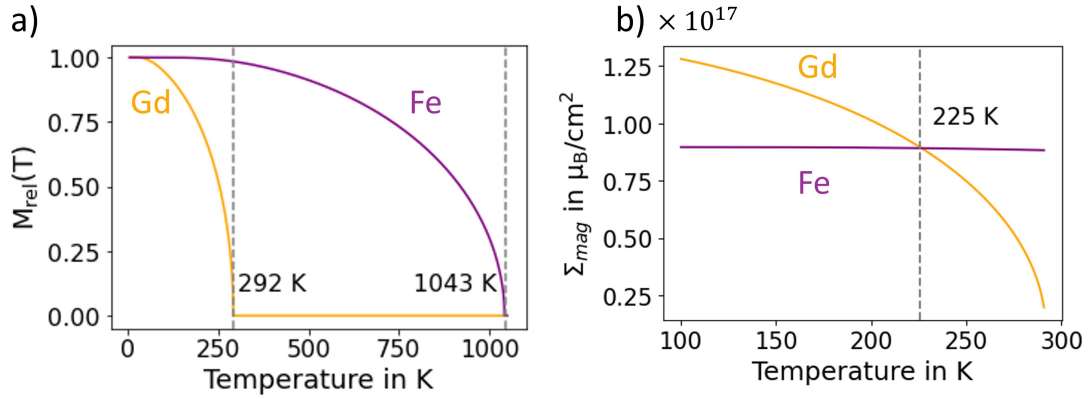

Figure 5.1: *a) Relative magnetization of ideal Gd and Fe, calculated in the framework of the Weiss molecular-field model. The Curie temperatures are marked with vertical dashed lines.*
b) Area density of magnetic moments for a 4.8 nm *thick Fe and a* 11.2 nm *thick Gd layer as a function of temperature. Due to their antiferromagnetic orientation, the Fe and Gd magnetic moments in the actual film have opposite signs. The compensation point occurs around* (225 ± 15) K. *Gd exhibits a reduced maximum magnetization due to growth conditions.*

dependences, which can be calculated in the Weiss molecular-field model for the spontaneous magnetization. A description of this model can be found in most textbooks on magnetism (e.g [30, 97]). Input parameters are the crystal structure, the atomic total angular momentum and the Curie temperature. Fig. 5.1 a) shows the results for Fe and Gd. We will expand on this by calculating the area density of magnetic moments in the Fe and Gd layers.
In the calculation, we assume that each Fe atom carries a magnetic moment of $m_{at,Fe} = 2.2\ \mu_B$. Under normal conditions Fe crystallizes in the bcc structure. One cubic unit cell contains 2 atoms[1] and has a volume of $V_{Fe} = a^3$ with $a = 2.87$ Å. Equivalently we find that each Gd atom carries a magnetic moment of $m_{at,Gd} = 7.55\ \mu_B$. Gd crystallizes in the hcp structure. Each hexagonal prism contains 6 atoms. The volume is calculated by $V_{Gd} = 3/2 \cdot b^2 c \cdot \tan 60°$ with the lattice constants $b = 3.64$ Å and $c = 5.78$ Å.
From these ingredients we obtain the magnetic moment density $\rho_{mag,i}$ of element i as

$$\rho_{mag,i} = \frac{m_{at,i}}{V_i} \ . \tag{5.1}$$

Our film is evaporated onto a circular W substrate with a macroscopic diameter of 8 mm. By working with a continuous magnetic moment density instead of discreet numbers of atoms, we thus produce a negligible error. Furthermore both layers have the same size in the sample plane. We will therefore only differentiate the layer extension d_i perpendicular to the sample plane. To account for partial thermal demagnetization, we also include the relative magnetization $M_{rel,i}$ as seen

[1] and is thus not the primitive unit cell of the bcc lattice

in Fig. 5.1 a) and obtain for element i a temperature dependent area density of magnetic moments $\Sigma_{mag,i}$:

$$\Sigma_{mag,i}(T) = M_{rel,i}(T)\rho_{mag,i}d_i \ . \tag{5.2}$$

Fig. 5.1 b) shows the values for both elements close to the compensation point, at which the magnetization of both layers is equal. For our layer composition, this occurs around (225 ± 15) K, which is the experimentally determined value, as we will see in Sec. 5.3. We have matched the calculated compensation temperature to the experimental one. For this the value of $M_{rel,Gd}(0\ \mathrm{K})$ was adjusted to $(51 \pm 5)\%$, meaning that the Gd layer in Fe/Gd has a reduced maximum magnetization compared to the saturation magnetization of an ideal Gd layer. In the following, we continue to relate the Gd magnetization to the ideal saturation magnetization. We assume that the Fe layer is perfectly magnetized, because it is less sensitive to the preparation conditions. One additional assumption goes into our estimate of the relative Gd magnetization:
It has been shown in several experiments as well as simulations, that the proximity to Fe enhances the magnetization in the Gd interface layer [98–101]. This can be attributed to hybridization between the electronic states of the itinerant Fe 3*d* and Gd 5*d* electrons [101]. The extension of this effect was estimated to be (4.1 ± 0.7) Å [100]. We assume that a Gd interface region of this thickness is magnetized with the magnetic moment per atom of Gd, but following the Fe Brillouin function. Without this proximity magnetization, we would need to assume a larger overall Gd magnetization of $(57 \pm 4)\%$ to retain the observed compensation temperature. That we are able to determine a reduction of the Gd magnetization is remarkable, because the XMCD signal is only proportional to the element-specific magnetization. The antiferromagnetic coupling between Fe and Gd in our film enables us to make quantitative statements nevertheless.

5.2 The X-ray-probe pulse

Before we look at our experimental results, we need to find out, in how far we probe the sample structure. For this we will use an IMD simulation of the X-ray intensity profile, similar to that shown in Ch. 4. Due to the very high energy resolution of the PM3 setup, we will neglect energetic broadening effects and use the natural linewidth of the optical coefficients.
In Fig. 5.2 we see IMD simulations of the field intensity at the Gd M_5 and Fe L_3 absorption edges in a Y/Fe/Gd multilayer film on a semi-infinite W substrate. As we saw for the single elemental film in Ch. 4, the intensity of X-rays at the M_5 edge within the Gd layer and at the L_3 edge for 708.7 eV (Fig. 5.2 b) red) in the Fe layer decays mostly exponentially with $1/e$ penetration depths of (20.7 ± 0.3) Å and (21.8 ± 0.3) Å, respectively. But we can see, e.g., in the Y layer around the M_5 edge as well as in the Fe layer at 705.9 eV (Fig. 5.2 b) blue) that different intensity profiles are possible. Here we have to keep in mind that multiple reflections are taken into account, which lead to interference effects. We can judge

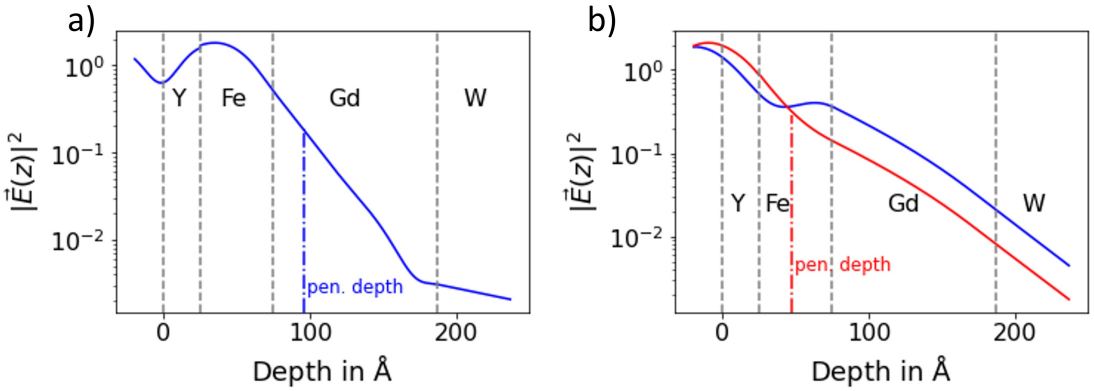

Figure 5.2: *a) Intensity profile of a X-ray beam with a photon energy of* 1184.3 eV. *b) Intensity profiles of X-ray beams with photon energies of* 705.9 eV *(blue) and* 708.7 eV *(red).*
In both cases the X-ray beam is incident at an angle of $\theta = 5°$ *on a Y/Fe/Gd film on a semi-infinite W substrate. Depth is measured along the surface normal. The penetration depth at which the intensity has dropped by a factor of* $1/e$ *is marked by the dash-dotted lines.*

now the sensitivity of our experiment to different depths of the sample. In Gd we preferentially probe the vicinity of the Fe-Gd interface. But the data taken at 708.7 eV (blue line) are representative of the entire Fe layer, since the intensity does not drop, but stays rather constant. Most data were recorded at this energy.

Recall the twisted state introduced in Sec. 2.2. Figure 2.5 shows a sketch of the differently oriented sublayers in the Fe and Gd layers. To visualize what we probe in this experiment, we make a similar illustration in Fig. 5.3 in which we arbitrarily divide both layers into sublayers: one interface layer and several sublayers that are further away from the Fe/Gd interface. Each sublayer contains a number of atomic layers, depending on the number of sublayers we define. We view the magnetization vectors from the top of the film to visualize the in-plane twisting. Figure 5.3 a) shows an orientation of the sublayer magnetizations for a temperature close to the magnetic compensation. We have learned in Sec. 2.2 that the twisted state will occur in this temperature regime. At the interface, both the Fe and Gd magnetization vectors point almost perpendicular to the external magnetic field $\vec{H}$. To reduce the Zeeman energy in the field, the system increases the exchange energy between neighboring atomic layers and allows for a small twist angle. Over many atomic layers, the magnetization is twisting towards alignment with the external field. Due to the lower inter-atomic exchange constant and Curie temperature in Gd, the twisting there is stronger at finite temperatures. Note that the shown angles are exaggerated, since theoretical predictions taken from Camley and Tilley [10, 11] show that the twist angle per atomic layer is only on the order of 0.1°, depending on temperature. If we take into account the depth sensitivity of the X-ray beams in Fig. 5.2, we note that we are sensitive to the vectors in Fig. 5.3 b), i.e. their projection along $\vec{H}$.

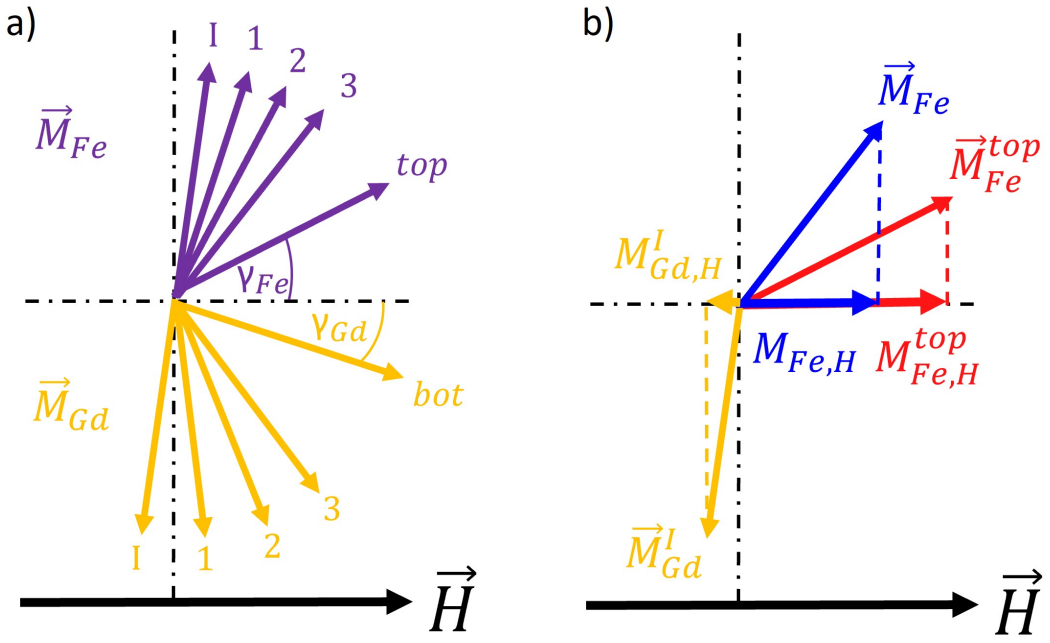

Figure 5.3: **a)** *Configuration of the magnetization in Fe and Gd when divided into sublayers. The image shows a view from the top. The magnetizations are twisting in plane with increasing distance from the Fe/Gd interface. Between the interface I and the top (Fe) or bottom (Gd) layer, the twist angle develops gradually. The twist angles $\gamma_{Gd,Fe}$ are measured from the field direction as shown, but exaggerated in the image for the sake of visibility. Theory by Camley and Tilley [10] predicts a twist angle on the order of* $0.1°$ *between atomic layers.* **b)** *The probe beam is sensitive to the orientation of the interface magnetization $\vec{M}^{I}_{Gd}$ in Gd. In Fe we observe the overall magnetization vector $\vec{M}_{Fe}$ for $h\nu = 705.9$ eV and the top layer $\vec{M}^{top}_{Fe}$ for $h\nu = 708.7$ eV. In XMCD we are sensitive only to the projections $M^{I}_{Gd,H}$ and $M_{Fe,H}$, $M^{top}_{Fe,H}$ along the external magnetic field.*

With these insights in mind we can move on to the experimental observations.

5.3 Magnetic hystereses

In this section we will extract information from magnetic hystereses measured at the PM3 beamline of BESSY II for the Fe/Gd bilayer. As discussed in Subsec. 3.1.1, the beamline allows for XMCD measurements in reflection geometry at variable angles as well as high energy resolution and photon flux. The results of this section will be a valuable foundation for the understanding of our findings in Ch. 6. We begin by introducing the experimental setup.

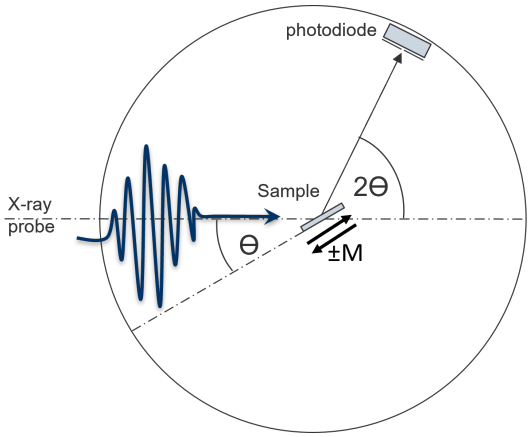

Figure 5.4: *The sample is tilted by an angle of $\theta = 5°$ to the X-ray beam. The detector is positioned at an angle of $2\theta = 10°$ according to the law of reflection. The incidence direction provides a large projection of the magnetization vector onto the probe-photon polarization vector.*

5.3.1 Scattering Setup

The sample is tilted by an angle of $\theta = 5°$ with respect to the X-ray beam. The beam is reflected to an angle of $2\theta = 10°$, where the photodiode is positioned. Figure 5.4 illustrates this geometry. The photons are elliptically polarized, so that their polarization vector is pointing along the beam axis. The small angle with the sample surface-plane provides a large projection of the magnetization vector onto the polarization vector. As described in Sec. 3.4, upon switching either the direction of the magnetic field or that of the photon's ellipticity, one observes the XMCD effect. Following this principle, we continuously change the magnetic field strength and obtain a hysteresis loop. The signal is representative of the sample magnetization as a function of external field. But keep in mind that only the difference between a set of two values at opposite magnetic field strengths is truly proportional to the magnetization.

The sample temperature was controlled with a cryostat. It is cooled via liquid nitrogen and stabilized to a set value via a *Lakeshore* temperature controller.

5.3.2 Experimental Observations

Figure 5.5 shows a selection of hystereses recorded at different temperatures to give a quick overview. The Gd layer was probed at the M_5 edge with an energy of (1184.3 ± 0.2) eV. The Fe layer was probed at the L_3 edge with an energy of (705.9 ± 0.3) eV. The uncertainty in photon energy stems from both the setting of the monochromator exit slit and, more importantly, from the use of slightly different probing energies during the experiment. Furthermore changes in the overall signal intensity occur between datasets. To correct for this, each hysteresis curve is normalized to the average signal of the curve itself. A value of 1 corresponds to the intensity of the M_5 or L_3 edge of an unmagnetized film. Due to the polarity of the current within the magnetic coil, $H < 0$ corresponds to a magnetic field parallel to the photon momentum and $H > 0$ to the antiparallel alignment. When we determine the difference of the curve between a magnetic field of $+H$ and $-H$, we determine $2I_{asym}$, with the XMCD asymmetry

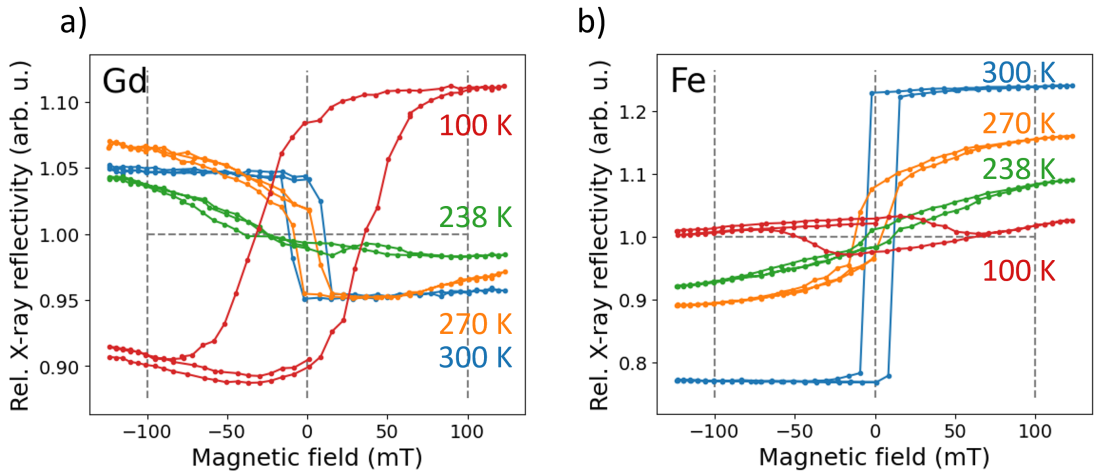

Figure 5.5: *Magnetic hystereses of the a) Gd and b) Fe layer of the Y/Fe/Gd film. The thin film was measured in reflection geometry with an angle of* $\theta = 5°$ *to the beam of elliptically polarized X-ray photons. The photon energy was* (1184.3 ± 0.2) eV *for Gd and* (705.9 ± 0.3) eV *for Fe. The magnetic field was applied in the sample plane. The y-axis displays the reflected signal, normalized to the average of each hysteresis scan. The horizontal dashed line indicates the average signal. In the vertical direction the zero field is indicated, while the lines at* ± 100 mT *show the field values used for studying magnetization dynamics.*

$$I_{asym} = \frac{I^{\uparrow\downarrow} - I^{\uparrow\uparrow}}{I^{\uparrow\downarrow} + I^{\uparrow\uparrow}} , \tag{5.3}$$

according to Stöhr *et al.* [30]. We will encounter the XMCD asymmetry in Sec. 5.4 again.

With the hystereses we start at room temperature and follow the cooldown of the sample. If we go back to Fig. 5.1 we note that the Fe layer is magnetically dominant[2] at 300 K. The film is in the aligned Fe state, as described in Subsec. 2.2, with Gd aligned antiparallel to the external field. We also note that pure Gd has no spontaneous magnetization remaining at this temperature, since it is above the Curie temperature. The observation of a hysteresis at this temperature demonstrates that the assumption of a proximity magnetization in the interface region of Gd is valid [100], see Sec. 5.1. Its orientation is antiparallel to Fe.

At 300 K both hystereses (blue lines in Fig. 5.5) have the typical shape for ferromagnetic samples: Upon crossing the coercive field the magnetic domains switch to full saturation magnetization in the opposite direction[3].

When cooling to 270 K (orange lines), the shape of both hystereses changes. The magnetization does not saturate but increases with increasing external field and the curves show a slight asymmetry in the external magnetic field between $+H$

[2] I.e. the Zeeman energy in the external magnetic field is dominated by the contribution of this layer.

[3] The hysteresis loop is "rectangular".

and $-H$. The orientation of the hysteresis, and thus the preferential orientation relative to the external magnetic field does not change.

At 238 K (green lines) Fig. 5.1 shows that we are close to the compensation temperature. The hysteretic effect, i.e. the loop opening, is not observable at the Gd M_5 edge. This behavior can be interpreted as the thermal switching point of Gd. The XMCD asymmetry, when taken at larger fields around ±100 mT, would still retain the same sign as for higher temperatures. This can be explained by an increase of the Zeeman contribution to the overall energy balance, which drives the system away from the twisted state that is already establishing at these temperatures, as we will see. The magnetizations tend towards the collinear orientation we see at 300 K with Fe aligned in the external field and Gd opposite to it. This will become significant for the understanding of our experiments on magnetization dynamics in Ch. 6.
The Fe hysteresis retains its general orientation and shows a behavior similar to a magnetization along a hard axis.
Furthermore we notice that the XMCD asymmetry for 238 K represented by the hystereses is significantly diminished for both layers compared to the XMCD asymmetry at 300 K. From the well known shape of the Brillouin function, the opposite behavior is to be expected in single layers. The phenomenon is therefore clearly a result of the interactions within the film and indicates the magnetization tilting away from the observation direction[4], as proposed by Camley *et al.* [10], i.e. the twisted state. Due to shape anisotropy, we assume that the new direction is still in the plane of the thin film. MOKE experiments by Felix Steinbach and Clemens von Korff-Schmising at the Max-Born-Institut in Berlin confirmed that there is no out-of-plane component to the magnetization.

When we try to infer the compensation point from the hysteresis measurements, it is clear that the sign of the magnetization changes for both layers between 238 K and 100 K. Surprisingly further analysis shows that the sign change occurs at a different temperature for both layers, namely around 240 K for Gd and around 210 K for Fe. This is caused both by the presence of the twisted state as well as our limited probing sensitivity. On the one hand the twisted state causes the magnetic moments in both the Fe and Gd layers to be aligned in a non-uniform way. What is more, both layers generally exhibit a different twist structure, so that their magnetic moments do not compensate as in a collinear ferrimagnet anymore. The X-ray penetration depth, seen in Fig. 5.2 on the other hand, shows that we are sensitive to the Gd interface region, not the entire layer as in Fe. We use the average of both switching temperatures to estimate the compensation temperature as (225 ± 15) K.

For a temperature of 100 K (red lines) both the Fe and Gd hystereses show the hysteretic effect and align with the external magnetic field for high field strengths.

[4] i.e. away from the incidence direction of X-rays, which is parallel to the external field in the in-plane direction

However, there is no sharply defined coercive field. Instead the film could be interpreted to be broken up into domains. This can be attributed to the helical magnetization structure of the twisted state in which atomic layers farther away from the Fe/Gd interface require a smaller external field to be switched. This is because the influence of the exchange interaction with the Fe layer magnetization diminishes with distance. The switching of the layer in the external field would therefore occur over a range of field strengths. The orientations of both layers are generally opposite to one another, showing the antiferromagnetic coupling. They are also reversed when compared to 300 K. This is due to the fact that Gd and no longer Fe is now magnetically dominant as seen in Fig. 5.1.

5.3.3 Average twist angle

Now that we are familiar with the temperature dependent shapes of the hystereses, we will try to understand why they occur.
When we look again at high fields and intermediate temperatures, we note that the XMCD asymmetry is strongly field dependent. This dependence contains valuable physical information; its extraction is the main objective of this section. Qualitatively, when we compare the high-field region of other hysteresis scans with that at 300 K we see that the Gd magnetization is always pulled into an alignment antiparallel to the field direction and the Fe magnetization parallel. Therefore the Gd XMCD asymmetry at low-field strenghts may be opposite to that at high field strenghts and the loop tilted.

In the first analysis step we need to quantify our observation that the development of the XMCD contrast with temperature differs from a Brillouin function. We will focus on the XMCD asymmetry as it is measured in static depth profiling (see Sec. 5.4) as well as in dynamic slicing experiments (see Ch. 6). That means we will extract the difference between the reflected intensity detected at an external magnetic field of $+H$ and $-H$ as a function of H and the temperature. We will differentiate between low external field strengths below 30 mT, where we observe the hysteresis loop, and high field strengths above 50 mT (compare Fig. 5.5). This distinction stems from the fact that a magnetic field of sufficient field strength to close the hysteresis loop is necessary to obtain a reproducibly ordered state of the magnetic domains. It is therefore only sensible to extract one value for the XMCD asymmetry in this field range, which we determine from the relative reflectivity at the center of the rising and falling flanks of the tilted hysteresis loops. This value is then representative of the remanent magnetization, i.e. without an external magnetic field, and will therefore be denoted as "0 mT". The high-field region in turn does represent ordered states for all magnetic field strengths.
To interpret the XMCD asymmetry we will make two assumptions:
i) At 300 K Fe is aligned fully parallel to the external field, Gd antiparallel.
ii) A (4.1 ± 0.7) Å thin layer of Gd is aligned antiparallel to Fe and follows the Fe Brillouin function with the Gd magnetic moment per atom. The rest of the film is magnetized as in a single Gd layer [100], albeit with the reduced magnetization of 51% we determined in Sec. 5.1.

The first assumption is grounded in the rectangular hysteresis shape of both layers at 300 K, indicating no twist. Furthermore Fe is magnetically dominant at this temperature[5] for a sample of collinearly aligned magnetic moments and should be aligned in field direction.
For Fe we can now set the value of the magnetization measured at 300 K to the relative magnetization $M_{rel,Fe}(300\ \mathrm{K})$ given by the Brillouin function. $M_{rel,Fe}$ gives the magnetization relative to the saturation magnetization $M_{s,Fe}$ that is reached at 0 K so that $M_{rel,Fe}(0\ \mathrm{K}) = 1$.
For Gd we include the reduced maximum magnetization of our film (see Sec. 5.1) and use $M_{rel,Gd}(0\ \mathrm{K}) = 0.51$. In a pure Gd layer we further encounter $M_{rel,Gd}(300\ \mathrm{K}) = 0$. But for our Fe/Gd film the second assumption yields

$$M^I_{Gd}(300\ \mathrm{K}) = -\frac{d^I_{Gd}}{d_{Gd}} M_{rel,Fe}(300\ \mathrm{K}) \tag{5.4}$$

where d^I_{Gd} and d_{Gd} are the proximity-interface thickness and the total thickness of the Gd layer. The negative sign marks the antiparallel alignment to the external magnetic field.
For Gd the range from 300 K down to 100 K was measured in a single dataset. The Fe data is divided into two datasets. The first was measured at a photon energy of 708.7 eV for temperatures from 300 K to 270 K and normalized to the Brillouin function as explained before. The second was measured at a photon energy of 705.9 eV and stretches from 275.5 K down to 100 K. We normalize the data for 705.9 eV indirectly to the Brillouin function by normalizing them to the data for 708.7 eV. Remember the influence of the probing energy on the penetration depth, seen in Subsec. 5.2. Because of it, normalizing datasets at different probing energies to one another introduces an error due to the different depth sensitivity. But because the length of a 180° twist in Fe is expected to be about 100 nm (see Sec. 2.2), the internal twisting between interface and top layer is on the order of only a few degrees, meaning that both energies should probe very similar magnetization arrangements and the error is small.

Using these assumptions, we finally arrive at Figs. 5.6 and 5.7. They show the temperature dependence of the XMCD contrast for a selection of field strengths. As mentioned before, the low-field region is labeled $H = 0$ mT and Fig. 5.6 takes into account that our Gd layer shows a magnetization that is reduced to 51% of the saturation magnetization $M_{s,Gd}$ of an ideal Gd film. To enhance the visibility of the experimental results, the Gd Brillouin function was further scaled with a factor of 0.2. Therefore a value of 0.1 represents the maximum Gd magnetization.

We can now clearly see that the XMCD asymmetry of the hystereses does not follow the Brillouin function. Let us therefore come back to the twisted state and how we may quantify it.
In the twisted state, Fe and Gd on average tilt towards an orientation perpendicular

[5]The ratio of Gd to Fe magnetic moments is 9.6 if we include the proximity magnetization in Gd.

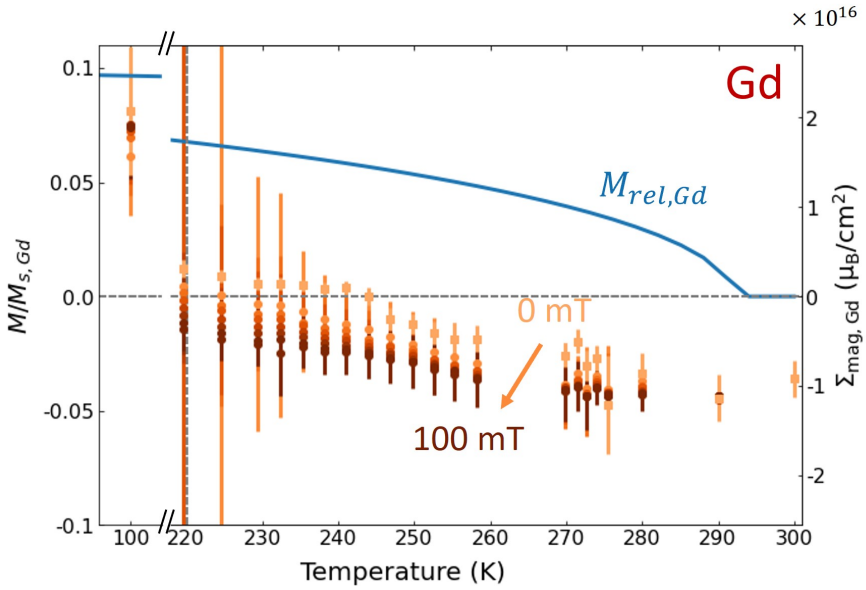

Figure 5.6: *Relative magnetization (left axis) and magnetic moments per area (right axis) as a function of temperature: Brillouin function of a bulk sample, scaled by a factor of* 0.2 *(blue) to enhance the visibility. A shown value of* 0.1 *thus corresponds to* 0.5*, showing the reduced maximum Gd magnetization relative to the ideal saturation magnetization M_s. The image additionally shows the relative magnetization extracted from the XMCD contrast of the Gd layer hystereses. The rectangles depict the XMCD contrast of the low-field hysteresis loop, while the dots mark the high-field contrast for different magnetic field strengths (*50 mT, 60 mT, 70 mT, 80 mT, 90 mT *and* 100 mT*). Darker colors indicate higher magnetic fields.*

to the external field [10], as we saw in Subsec. 2.2. According to Camley and Tilley there is an internal structure to each layer [10], as sketched in Fig. 5.3. The magnetization directions of adjacent atomic layers have an angle between each other.

In the setup of the hysteresis measurements, we have fixed both the photon energy as well as the incidence angle. We are therefore only sensitive to the projection of the vector sums $M^I_{Gd,H}(T)$ and $M^{top}_{Fe,H}(T)$ of all magnetic moments in the probed area[6] onto the photon momentum axis or H-axis. We are not sensitive to the depth dependent twist angle of the magnetic moments. What we will determine is the angle of $\vec{M}^I_{Gd}(T)$ and $\vec{M}^{top}_{Fe}(T)$ with the H-axis, which we will call "average twist angle" $\gamma_i(T)$ for simplicity, where i denotes the elements Gd, Fe. A decrease of $\gamma_i(T)$ could be caused both by a decrease of the twist angle already at the interface as well as by an increased angle step size between atomic layers. The expected length scale over which the atomic layers reach alignment with the external field is tens to hundreds of nanometers [11] and hence the order of magnitude of the angle step size 0.1°. $\gamma_i(T)$ is thus a rather good measure of the twisted state as a whole, even though it is not the twist angle of the full magnetization in the layer. We recall Eq. 5.4 and expand it to the form

[6] weighted by the remaining probe beam intensity at the respective depth

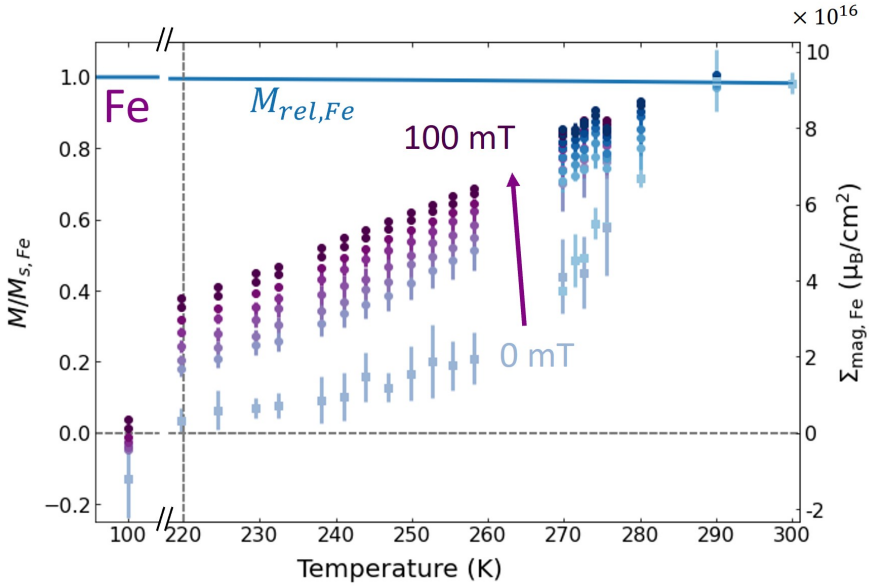

Figure 5.7: *Relative magnetization (left axis) and magnetic moments per area (right axis) as a function of temperature: Brillouin function (blue) and XMCD contrast of the Fe layer hystereses. Shades of purple for* 706 eV*, shades of blue for* 709 eV*. The rectangles depict the XMCD contrast of the low-field hysteresis loop, while the dots mark the high-field contrast for different magnetic field strengths (*50 mT, 60 mT, 70 mT, 80 mT, 90 mT *and* 100 mT*). Darker colors indicate higher magnetic fields.*

$$M_{Gd,H}(T) = -\left(\frac{d^I_{Gd}}{d_{Gd}} M_{rel,Fe}(300\ \mathrm{K}) + \left(1 - \frac{d^I_{Gd}}{d_{Gd}}\right) M_{rel,Gd}(T)\right) \cos\gamma_{Gd}(T,H) \tag{5.5}$$

for Gd. For Fe we find

$$M_{Fe,H}(T) = M_{rel,Fe}(T) \cos\gamma_{Fe}(T,H)\ . \tag{5.6}$$

Thus we can extract $\gamma_i(T,H)$ from the experimentally determined $M_{i,H}(T)$, that is normalized as seen in Figs. 5.6 and 5.7. The value $d^I_{Gd} = (4.1 \pm 0.7)$ Å is the interface thickness of Gd and d_{Gd} and d_{Fe} are the total thicknesses of the layers. $M_{rel,i}(T)$ is given by the Brillouin functions. The signs are chosen to ensure that Gd is aligned antiparallel ($\gamma_{Gd} = -180°$) and Fe parallel ($\gamma_{Fe} = 0°$) to the field at 300 K. The data do not contain this information, because they are only sensitive to the component along the H-axis and the cosine function is symmetric around zero.

Figure 5.8 shows the absolute values of angles $|\gamma_i(T)|$ that result from Eqs. 5.5 and 5.6. Depicting the absolute value makes it more easily apparent how close the layers are to being perpendicular to the external magnetic field.

On the one hand we can see that the Fe and Gd XMCD asymmetries switch their sign at different temperatures, which can be explained by the twisted state as

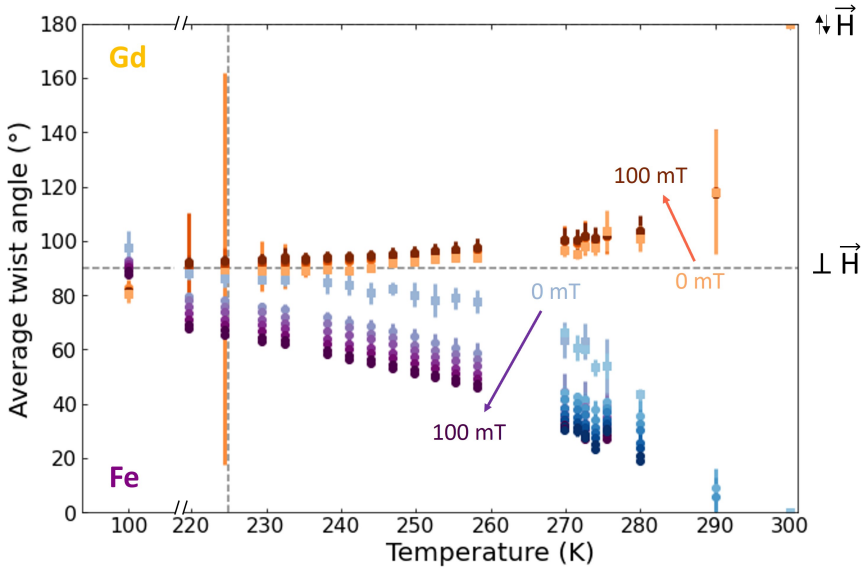

Figure 5.8: *Average twist angle as a function of temperature: The rectangles depict the XMCD contrast of the low-field hysteresis loops, denoted as* 0 mT*, while the dots depict the high-field XMCD contrast at different magnetic field strengths (*50 mT, 60 mT, 70 mT, 80 mT, 90 mT *and* 100 mT*). Gd is plotted in shades of yellow and Fe in shades of purple for* 706 eV *and shades of blue for* 709 eV*. The dotted lines mark the estimated compensation temperature at* 225 K *and the orientations parallel and perpendicular to the external field.*

well as our probing depth. The sublayer magnetizations that we detect are not antiparallel to each other. This is only the case directly at the Fe/Gd interface, but we are sensitive only to the interface sublayer of Gd, while we measure the sublayer at the top, the furthest away from the interface, for Fe. For that reason, the measured twist angle of Gd is close to 90° while we measure a Fe magnetization that is significantly tilted towards the field. We learned in Sec. 2.2 that Gd has a shorter twist length, i.e. a larger twist angle per layer, than Fe at finite temperatures, as well. So we see that on top of the fact that the experimental sensitivity sets our window of observation, the magnetic structure in both layers is generally different. On the other hand we notice that the sign change is influenced by the applied magnetic field strength, because the layer magnetizations are forced towards a parallel or antiparallel alignment to the field, depending on temperature.
Nevertheless the sign of the XMCD contrast in the hysteresis data is changed below 220 K for both layers, as shown in Figs. 5.6 and 5.7.

Figure 5.9 gives us a more intuitive visualization of the two-dimensional dependence $\gamma_i(B,T)$. We limit the range of interest to the temperature region between 220 K and 280 K where $\gamma_i(B,T)$ changes more slowly.

We can clearly see that there is an almost diagonal gradient of change to γ_i in both layers, i.e. a reduction of both the external field and the sample temperature drives γ_i towards zero. Only in remanence, at $H \approx 0$ mT, a sign change occurs for Gd, while the Fe magnetization vector still exhibits a parallel component to the magnetic field within this temperature window. The presence of an external

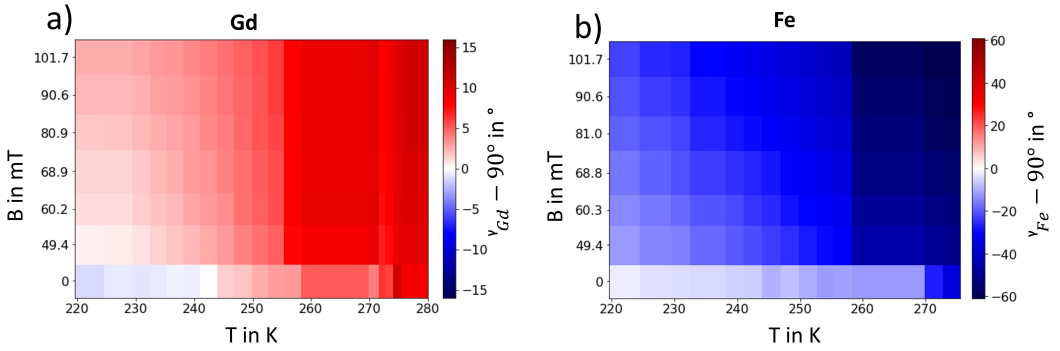

Figure 5.9: *2D pseudo color plot of the average twist angle γ_i for a) Gd and b) Fe. Red color indicates an antiparallel and blue a parallel component to the field. The vertical axis shows the magnetic field strength with the low-field readout as the lowest entry. The horizontal axis shows the sample temperature.*

magnetic field reduces the switching temperature. As we can see in Fig. 5.8, both Fe and Gd are switched at 100 K, irrespective of H. Perpendicular to the mentioned gradient in H and T the angle stays mostly constant. Due to the different switching temperatures of Fe and Gd, a spin flop with components of both layers parallel to the external field is established at intermediate temperatures.

If we keep the temperature constant, we observe that an increase of the magnetic field strength drives the film towards a collinear state with Fe aligned to the field and Gd antiparallel to the field, as γ_{Gd} increases and γ_{Fe} decreases.

5.4 Magnetic depth profiling

In this section we will take a look at the magnetic depth profile. That means our goal is to gain information on how the magnetization changes direction as a function of the depth in the film. We will first describe the experiment and how the data were processed. Then we will use the DYNA software to simulate our experimental data and discuss our findings.

5.4.1 Data acquisition

Just as the hysteresis measurements described in Sec. 5.3, this experiment was performed at the PM3 beamline of BESSY II.
Due to the energy dependence of the absorption coefficient given in Eq. 3.7, X-ray photons of different wavelengths will exhibit a different penetration depth within the sample. They will therefore provide a different depth sensitivity. The same holds for a change of the incidence angle. If we increase the angle between X-ray beam and sample surface, approaching normal incidence, we increase the penetration depth. We must keep in mind, though, that the incidence angle also

changes the projection of the magnetization vector onto the photon momentum axis. For normal incidence we are blind to an in-plane magnetization, but have the highest out-of-plane sensitivity.
These two effects combined necessitate that our measurements cover a range of energies and incidence angles to provide a full picture of our sample. To this end we have performed $\theta - 2\theta$ scans. We detect the specularly reflected intensity for varying incidence angles. This was done for 9 energies distributed over a spectrum around the Gd M_5 absorption edge. To further characterize the temperature dependence of the magnetization, which we have already seen in Sec. 5.3, the procedure was repeated for three temperatures.
Each angle scan covers incidence angles between $\theta = 2°$ and $\theta = 60°$ and was recorded in steps of 0.1°. At each point, the reflected signal for ±100 mT is recorded. To correct for varying photon flux of the synchrotron storage-ring, the signal is normalized for the ring current in our analysis.

We make use of DYNA to simulate the reflectivity scans. It allows us to define 7 parameters for each simulated sublayer. These can be divided into 4 structural (see Subsec. 5.4.2) and 3 magnetic parameters (see Subsec. 5.4.3). It is advisable to determine the sample structure first and keep the obtained parameters fixed for the investigation of the magnetic structure. This follows from the fact that the XMCD asymmetry contains both charge and magnetic scattering information, while the structure can be determined purely from the charge scattering.
Our measurements were performed around the Gd M_5 resonance. We are thus insensitive to the Fe magnetization, but structural information is accessible to a point. The simulations are based on tables of the optical coefficients f', f'', $\mathcal{M}_1$ and $\mathcal{M}_2$, which we have seen in Subsec. 3.5.1. They are derived from a total electron-yield experiment by Prieto *et al.* [102] in the case of Gd and XAS and XMCD experiments by Chen *et al.* [103] in the case of Fe.

5.4.2 Sample structure

To simulate the structure we use the following parameters: the molar density of the material, the thickness and the roughness of each sublayer. As mentioned above, we try to simulate the charge scattering intensity

$$I_{charge} = I^{\uparrow\downarrow} + I^{\uparrow\uparrow} \tag{5.7}$$

Due to lattice mismatch and other growth conditions, which can not be fully controlled, the density of thin layers can significantly deviate from that of bulk samples of the same element. For Gd on W this was discussed in Sec. 3.6 and found to be negligible, despite the fact that the magnetization of the layer is reduced compared to the sum of all magnetic moments. But Fe on Gd and Y on Fe are grown without annealing afterwards and are both thinner than the Gd layer. The relative influence of reconstructed monolayers close to the respective interface is therefore larger.
Furthermore the energy scale given by the beamline setup needs to be calibrated.

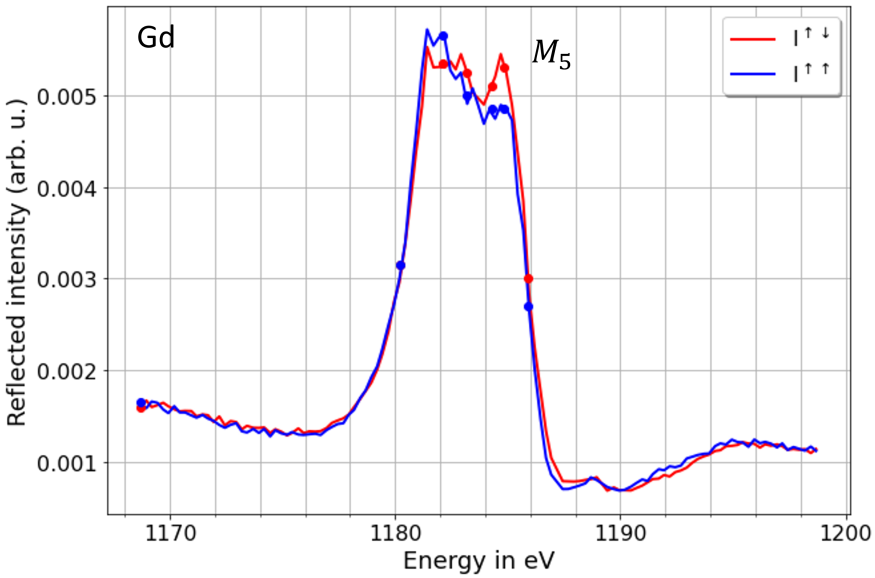

Figure 5.10: *X-ray reflectivity for positive and negative magnetic field polarization at the Gd M_5 edge at $T = 261$ K, corrected for the energy dependent X-ray intensity as described in the text. The data were recorded in reflection geometry at an incidence angle of $\theta = 5°$. The dots mark the energies chosen for $\theta - 2\theta$ angle scans.*

Drifts of the incidence angle of X-rays on the monochromator and thermally induced drifts of the monochromator position itself result in drifts of the energy scale. These drifts are on the order of a few eV and thus relevant for measurements in resonance, where the optical constants vary significantly with energy. For a given uncertainty of the incidence-angle, the energy drift scales roughly with $E^3/2$. It is however usually sufficient to consider a constant energy shift over the range of a resonance spectrum.

Gd $M_{5,4}$ X-ray reflectivity

Both the layer density and the energy shift can be determined by studying the X-ray reflectivity.
Figure 5.10 shows the spectrum recorded for the Gd M_5 and M_4 edges at a temperature of $T = 211$ K. The energy dependence of the beamline intensity was measured on the photodiode in the direct beam by removing the sample. It shows a linear decrease of intensity with energy. The spectrum in Fig. 5.10 is divided by that energy dependent intensity to correct for it.

We receive the best match between simulation and data for an increased Fe density of 0.184 $\frac{\text{mol}}{\text{cm}^3}$ as compared to the bulk value of 0.136 $\frac{\text{mol}}{\text{cm}^3}$, while the Gd density is set to the bulk value of 0.0502 $\frac{\text{mol}}{\text{cm}^3}$. The comparison between simulation and experiment is shown in Fig. 5.11. The energy axis is shifted by a constant offset of -1.3 eV, meaning that the read-off energy in our experiment was larger than the

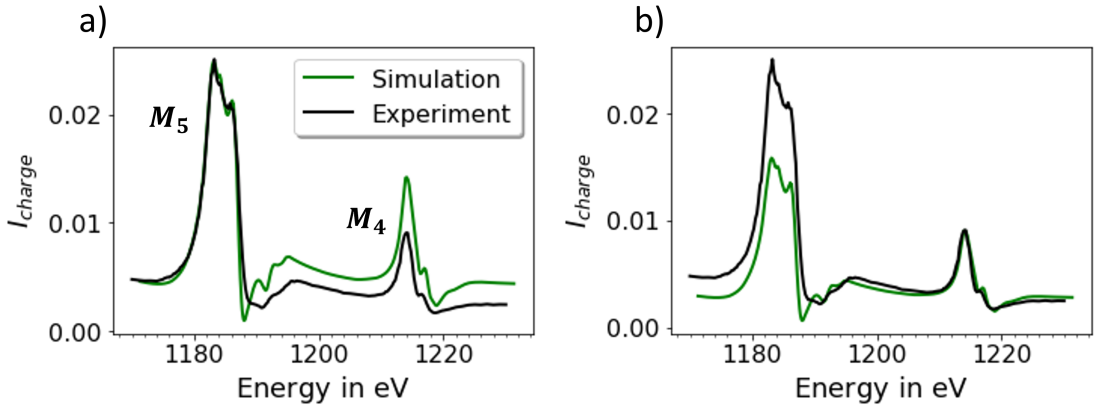

Figure 5.11: *Comparison between the simulated (green) and measured (black) X-ray reflectivity of Gd around the M_5 and M_4 absorption edges. In a) and b), the simulation has been differently scaled.*

actual energy.
It is immediately noticeable that the peak shape of both the M_5 and the M_4 absorption edge is correct, but the relative intensity ratio among them is not described correctly. This can be attributed to inappropriate optical constants used for the simulation. We will discuss this problem at the end of this section and encounter it during our further analysis.

Angle scans

Now we inspect the charge scattering intensity recorded in our angle scans. Figure 5.12 shows four such scans, at the off-resonant energy of 1168.7 eV, in the M_5 resonance at 1183.2 eV and 1184.8 eV as well as at the right flank of the resonance at 1185.9 eV. The simulated angle scan is shown in green. The experimental data that are shown here were recorded at $T = 211$ K, but are representative of all temperatures.
Having determined the molar density via the X-ray reflectivity, we are left with the thickness and roughness[7] of each layer. We assume that the Fe and Gd layers are both homogeneous, so that each can be treated as a single layer in the simulation. The periodicity of the Kiessig fringes mainly depends on the thickness of the Gd film with a smaller influence of Fe and a marginal influence of Y. An increased roughness on the other hand smears the fringes out and may lead to different intensity distributions.
At the two highest energies, 1184.8 eV and 1185.9 eV, an overall intensity modulation becomes apparent, as described below. To understand this modulation we can view the reflected intensity in the simplified picture of Bragg's law

$$2d \sin\theta = n\lambda_{ph} \ . \tag{5.8}$$

[7]That is the roughness of the upper surface/ interface with the layer above.

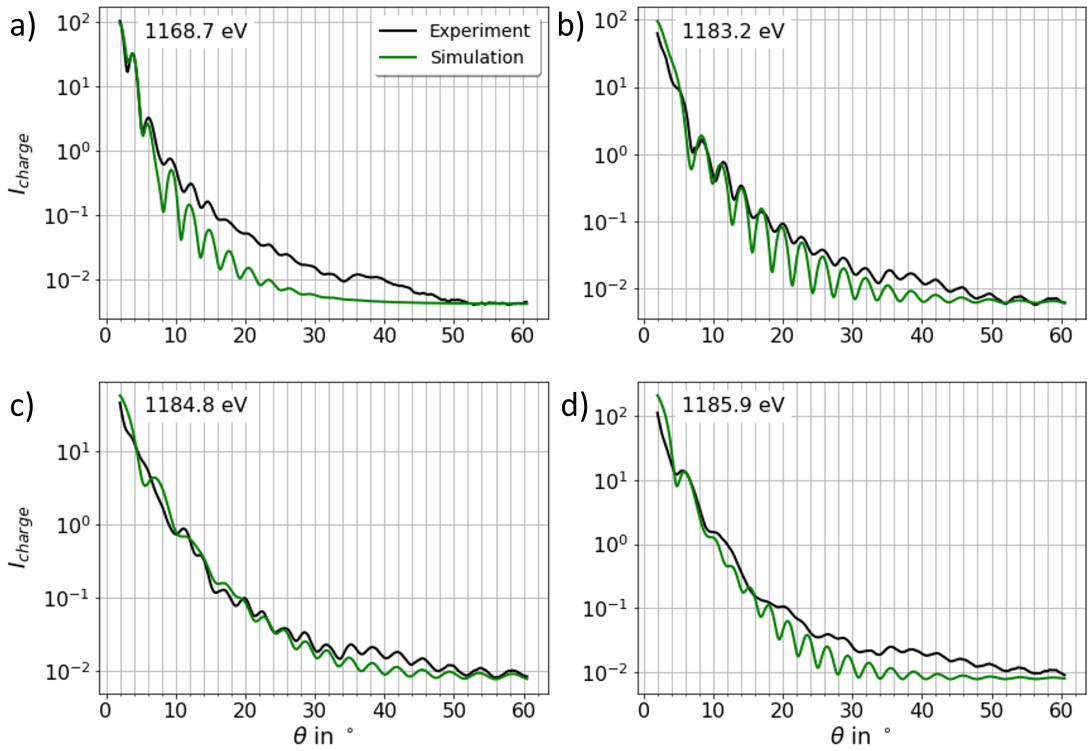

Figure 5.12: *Comparison between the simulated (green) and measured (black) angle scans at a)* 1168.7 eV, *b)* 1183.2 eV, *c)* 1184.8 eV *and d)* 1185.9 eV *and* $T = 211$ K.

For a thickness d and a photon wavelength λ_{ph}, we expect maxima of the reflected intensity at an angle θ. This means that the interference pattern from layers with smaller thickness only appear for larger wavelengths, if the scattering angle range is fixed. In our case the Fe layer is expected to be significantly thinner than the Gd layer. The simulations show that the overall intensity modulation is strongly influenced by the Fe thickness. An increased Fe roughness smears the modulation out until it vanishes. It is possible to determine the thickness and roughness of Fe in this way, albeit with a rather large uncertainty. Overall, the simulation reflects the data in the small angle region up to 15° rather well and deviates for larger angles.

The structural parameters which yield the best results may vary between angle scans at different energies. We can also see that there is a general deviation in the overall intensity and the amplitude of the Kiessig fringes for all but the smallest angles. The reason for both phenomena is that the energy dependence of the optical constants is very strong in the vicinity of the absorption edge. Even small deviations of the spectral shape assumed for the simulation and that of the actual sample lead to significantly different results.

Overall we see that the positions of minima and maxima of the Kiessig fringes are modelled correctly by the simulation for all energies. The structural parameters that we extracted from the simulations at all energies are shown in Fig. 5.13. As mentioned before, we are insensitive to the Y capping layer. It is therefore not feasible to determine its thickness and roughness from our simulations. The

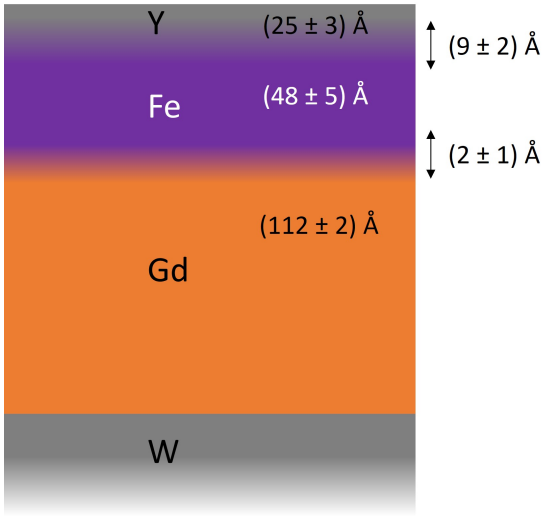

Figure 5.13: Sample structure from bottom to top: *W(110) single crystal; Gd(0001)* (112±2) Å, *roughness* (2±1) Å*; Fe* (50±4) Å, *roughness* (9±2) Å*; Y* (25± 3) Å*. The Y thickness is only determined from the evaporation rate. All layers were evaporated at* 300 K*. The Gd layer was annealed to* 800°C *after evaporation (see Subsec. 3.6).*

evaporation rate measured during growth suggests a Y thickness of (25 ± 3) Å.

5.4.3 Magnetic depth profile

With the structural parameters fixed, we can look into the XMCD asymmetry as given in Eq. 5.3. Figure 5.14 shows the angle-dependent asymmetry at the same energies shown in Fig. 5.12 for different temperatures. The applied strength of the external magnetic field was ±100 mT in all cases. The curves were smoothed by a Savitzky-Golay filter to third degree with a window size of 11 points, i.e. 1.1°. The angle range was cut at 40°, because the signal goes to zero for high scattering angles, which enhances the noise when we calculate the asymmetry. Also note that the fringes in the asymmetry scans are no Kiessig fringes. They are not representative of the sample structure. In a magnetized sample, the Kiessig fringes of $I^{\uparrow\uparrow}$ and $I^{\uparrow\downarrow}$ exhibit a different intensity modulation and are usually shifted on the θ-axis with respect to one another. This gives rise to the intensity modulation in I_{asym}.

For all energies and most angles we observe an increase of the intensity with temperature. That means with increasing temperature, the projection of the magnetization onto the external magnetic field gets larger. Figure 5.6 shows the same trend. Before resonance, at a photon energy of 1168.7 eV, this is the only clearly discernible change with sample temperature. At 1183.2 eV the amplitude at low θ decreases with temperature. Furthermore between $10 - 20°$ we observe peak shifts towards 14°, where two peaks are merging as the temperature increases. For 1184.8 eV and 1185.9 eV we mostly see a decrease of the modulation amplitude, i.e. a smearing of the peaks with increasing temperature.

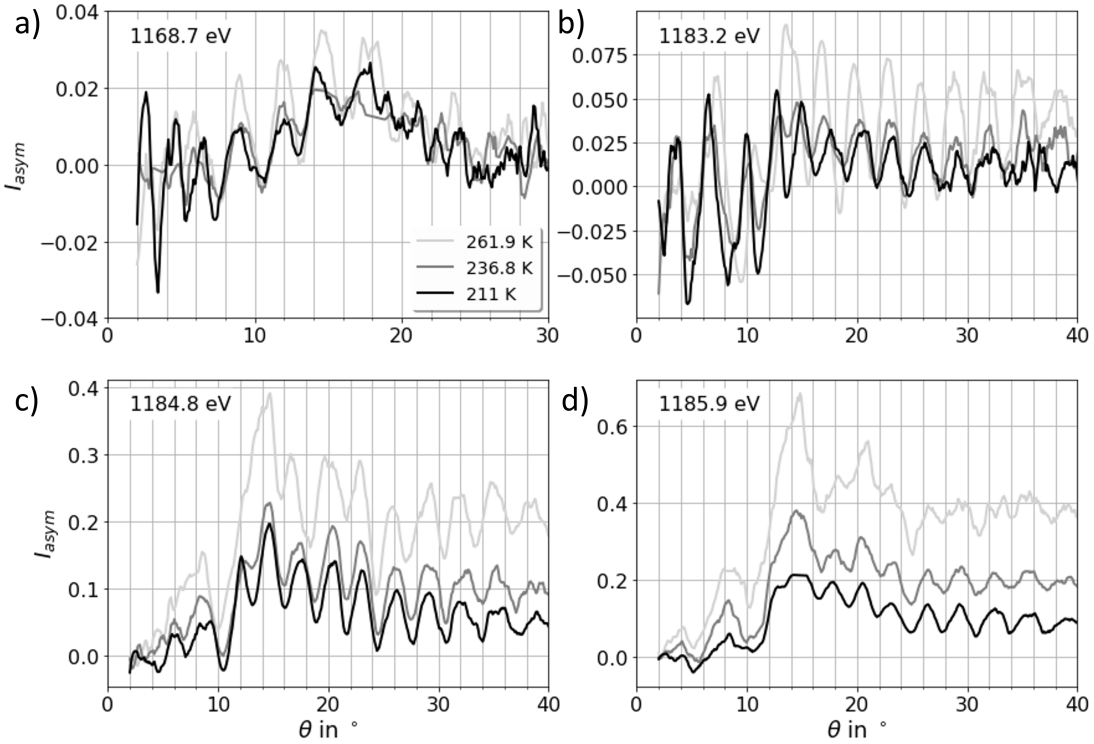

Figure 5.14: *The asymmetry I_{asym} of the angle scans. The angle range was reduced due to the high noise level of the asymmetry at higher angles. Depicted are the energies a)* 1168.7 eV*, b)* 1183.2 eV*, c)* 1184.8 eV *and d)* 1185.9 eV *again. Shades of grey indicate the temperatures of* $T = 211$ K, 237 K, 262 K *as shown by the legend in panel a).*

Simulation

To simulate the asymmetry, we add the following parameters to the structural simulation: the length of the relative sublayer magnetization vector $\vec{M}_{sl}$ and the polar and azimuthal angles φ and γ of the magnetization, as illustrated in Fig. 5.15. The angle φ is measured from the out-of-plane direction or surface normal of the sample m_{op}. γ on the other hand is the in-plane angle of the magnetization with the transversal magnetization axis m_{tran}. The value of the sublayer magnetization M_{sl} is set to 1.0 for the Gd sample of Prieto *et al.* from which the optical constants were derived [102]. It generally differs for other samples.
At 0 K the twist of the magnetization direction in both layers amounts to only a few degree over the entire layer, due to the long twist length at this temperature as we calculated in Sec. 2.2. While the low Curie temperature of Gd causes significant changes of the twist length with temperature, it is nearly constant for Fe. We have therefore chosen 9 energies for the $\theta - 2\theta$ scans that lie around the Gd M_5 edge and are not sensitive to the Fe magnetization. Hence we will neglect it in our simulation.

Because we assume a depth-dependent magnetic structure, we generally need to split the Gd layer into sublayers, as shown in Fig. 5.3 before. The first and simplest assumption implicit in the DYNA code is that the magnetic moments

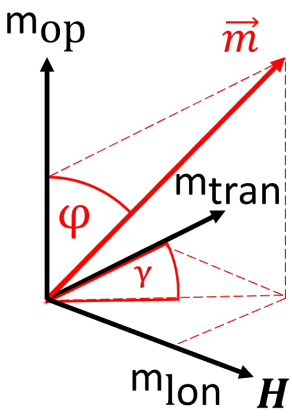

Figure 5.15: *The coordinate system of DYNA. Magnetization longitudinal m_{lon} and transversal m_{tran} to the probe beam and out-of-plane m_{op} with respect to the sample. The polar and azimuthal angles are φ and γ. The external magnetic field H lies along m_{lon}.*

within one sublayer, i.e. at a fixed depth, are equal in size and orientation. It is therefore possible to assign a sublayer magnetization $\vec{M}_{sl}$. To determine the microscopic depth profile of the magnetization, we would like to have a high depth resolution, i.e. very thin sublayers. Our simulated sublayers have a thickness of two atomic layers, i.e. 5.8 Å. This results in around 20 sublayers for the Gd layer. The roughness is considered only for the topmost sublayer[8]. In total we have 60 nominally free parameters. We reduce the number of parameters by assuming the twisted state:

- The Gd magnetization is highest at the Fe-Gd interface and decays exponentially to the Gd equilibrium value at a given temperature.
- The magnetization lies purely in-plane due to the shape anisotropy.
- The in-plane twist angle follows the predictions by Camley and Tilley (see Sec. 2.2).

The first of these assumptions is a simple realization of the proximity magnetization that we have discussed before and is described in [98–101]. The modulus of the sublayer magnetization at distance x from the Fe/Gd interface and temperature T, where $x = 0$ defines the interface, takes the form

$$M_{sl}(z,T) = M'(1 - M_{rel,Gd}(T))e^{-\mu z} + M' M_{rel,Gd}(T) \ , \tag{5.9}$$

with the prefactor M', the decay length $1/\mu$ and the depth z.

The second assumption sets $\varphi = 90°$ for all sublayers, as φ is measured from the out-of-plane direction m_{op}. And the third leads us back to Subsec. 2.2 and Ref. [10]. It predicts a hyperbolic depth dependence of the twist angle $\gamma(z)$, which we formulate as

[8] Roughnesses for intermediate sublayers have no effect, since the material and thus the optical constants are equal.

$$\gamma(z) = A \arccos\left(\tanh\left(\lambda z\right)\right) + 90^\circ \tag{5.10}$$

with amplitude

$$A = \frac{2\gamma_0'}{\pi} \tag{5.11}$$

and characteristic length $1/\lambda$ for

$$\lambda = \frac{\ln\left(1+\cos\frac{1}{2}\right) - \ln\left(1-\cos\frac{1}{2}\right)}{2z_0} \ . \tag{5.12}$$

In DYNA the angle $\gamma(z)$ is measured from the transversal direction m_{tran}, while Camley refers the angle to the external magnetic field direction, i.e. m_{lon}. We therefore add 90° in Eq. 5.10 to translate between the DYNA coordinate system and the one used by Camley. We will stay in the DYNA coordinate system when stating angles γ.
We set the parameters $\gamma_0 = \gamma_0' + 90^\circ$ and z_0. Equations 5.11 and 5.12 are defined in such a way that γ_0 and z_0 obtain an intuitive meaning when we enter A and λ in Eq. 5.10: We find $\gamma(0) = \gamma_0$ as the starting angle and $\gamma(z_0) = \gamma_0'/\pi + 90^\circ$. Thus z_0 gives a characteristic distance at which the magnetization is almost aligned with the external magnetic field, i.e. 90° measured from the perpendicular direction m_{tran}. It can be understood as a trigonometric equivalent to an exponential decay length.

We now have merely 4 parameters that define our model. The magnetization scaling factor M' that sets the magnetization at the interface, the decay length $1/\mu$ of the magnetization as a function of depth, the twist angle at the interface γ_0 and the characteristic length of the twist-angle relaxation z_0.
The simplest way to start is to simulate layers without internal magnetization twist, but uniformly rotated by the angle γ_0. Thus $z_0 = \infty$ and $\gamma(z) = \gamma_0$. Due to the geometry of the experiment, the signal for $\gamma_0 = 0$ is always zero as there is no projection onto the photon momentum axis.

In Fig. 5.16 we have depicted simulations for the extreme cases of $\gamma = 90^\circ$, i.e. parallel to the external field, and $\gamma = -90^\circ$, i.e. antiparallel to the field, for the 1184.8 eV asymmetry scan at a temperature of 262 K. Both simulations have an interface magnetization of $M' = 1.0$. The $\gamma = -90^\circ$ simulation shows the same quantitative intensity modulation as the data in a range from $\theta \approx 14^\circ$ to $\theta = 24^\circ$. For larger θ there appears to be a phase shift[9] and the maxima of the $\gamma = 90^\circ$ model start to coincide with those of the experimental data. For $\theta < 14^\circ$ we notice stronger deviations of the simulation from the data. They are already visible in

[9]We use the terminology of oscillations for the ease of description. As mentioned before, the asymmetry does not show the Kiessig fringes and the intensity modulations do not follow an oscillatory function.

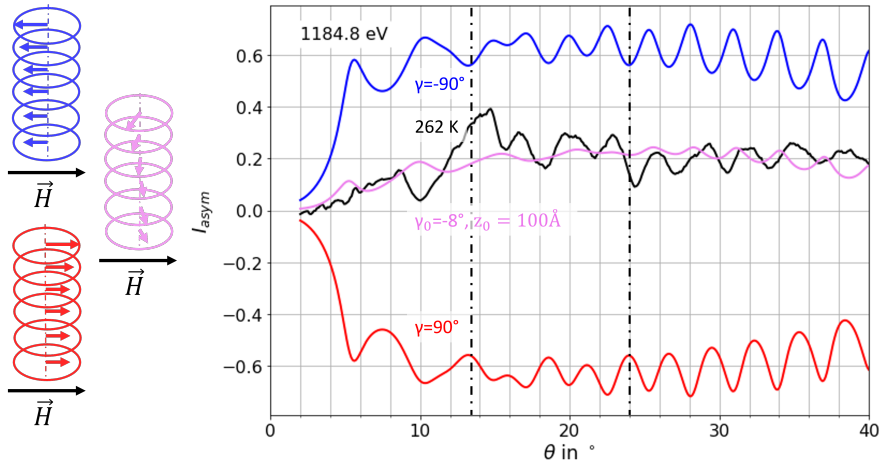

Figure 5.16: *Experimental asymmetry (grey) at* 1184.8 eV *and* $T = 262$ K *shown together with simulations of a uniformly tilted Gd layer with* $\gamma = -90°$ *(blue) and* $\gamma = 90°$ *(red). The violet curve shows a simulation with an internal twist. The vertical dashed lines divide the* θ *range. For* $\theta < 14°$ *our models show a poor agreement with the data. Is is carried over from the structural model for* 1184.8 eV *seen in Fig. 5.12. In the range between the two dashed lines, the* $\gamma = -90°$ *model fits the periodicity. The* $\gamma = 90°$ *model is a better description for* $\theta > 20°$*. To the left of the graph we see sketches of the magnetic structures that are implied by the models.*

the structural analysis in Fig. 5.12 c) and are carried over to the XMCD asymmetry.

We conclude that it is necessary to combine contributions that have a negative and those that have a positive projection onto the magnetization axis to model the experimental asymmetry, i.e. z_0 must be finite. This is an insight in itself. In Ref. [10] Camley and Tilley [10] predicted a length scale for the internal tilting back to field-alignment of $4.3 - 8.5$ μm. With the relations given by Camley in Ref. [11] (see Subsec. 2.2), we estimate a length of ca. 96 nm in Fe and ca. 45 nm in Gd for a 180° twist at 261 K. That our data indicate the aforementioned contributions implies that the length scale is actually close to the thickness of our Gd layer with $d_{Gd} = (112 \pm 2)$ Å, in agreement with our estimate.
To include this observation in our simulation we use the model presented in Eqs. 5.9 and 5.10. As an example we set $\gamma_0 = -8°$, which can be read off from Fig. 5.8 at 258 K, and $z_0 = 100$ Å so that the twist angle at $z = 110$ Å changes to $\gamma(110\ \text{Å}) \approx 63°$. The length of the magnetization vector is set to an initial value of $M' = 1.0$ and decays with a length of $\mu = 0.026$ Å^{-1} down to the relative equilibrium value $M_{rel,Gd}(261\ \text{K}) = 0.23$.
As we can see in Fig. 5.16, the model reproduces the minima and maxima positions at 1184.8 eV between $\theta \approx 18°$ and $\theta \approx 30°$. All three models struggle to replicate the intensity modulations quantitatively and fail to replicate the maxima positions over the entire angle range. Exploring the parameter space of our model reveals that such an agreement with the experimental asymmetry is not within the scope of our current model.

To understand what the model can achieve, we first note that the exemplary simulation is very similar to the sum of the two simplified simulations with $z_0 = \infty$. In those, the sign of γ_0 determines the sign of the intensity modulations, while the value determines their amplitude. This is because we are considering in-plane rotations, while the photon momentum axis rotates with θ in a plane perpendicular to the sample. Therefore an increase of $|\gamma_0|$ is qualitatively indistinguishable from an increase of M'.
For the characteristic length x_0 we find that if we set x_0 finite, a decrease of x_0 leads to a more rapid change of γ, suppressing contributions from sublayers with γ close to γ_0 and vice versa. The value of M' sets the overall intensity of the simulation[10]. Lastly, the value of μ influences the weighting of the sublayer contributions. For large values of μ, e.g. $\mu = 0.5$ Å^{-1}, the proximity magnetization has already vanished almost completely in the second sublayer. This gives the first sublayer, i.e. the interface layer, an increased weight, because it's magnetization is larger than that of the other sublayers. In the case of Fig. 5.16, the maxima positions of the violet curve resemble those of the $\gamma_0 = -90°$ model (blue) more closely for large μ.

It is clear that we need a model to reduce the amount of free parameters. It is reasonable that the sublayer parameters are connected by a continuous relation, as well. At the current time, the assumptions we made in the beginning seem reasonable. But a refinement of our simulation is needed to improve the agreement with the experimental data, nevertheless. Furthermore we have seen deviations of the simulation from the charge scattering data already. These deviations naturally carry over to the asymmetry simulation. As was mentioned before, it is advisable for future experiments to use the optical coefficients of the specific sample under investigation. This should be the first step to improve the analysis.

Optical coefficients

In Subsec. 3.2.3 we saw that one derives the imaginary part f'' of the atomic form factor from a XAS experiment. We use the data given by Prieto *et al.* [102]. They measured the total electron yield[11] of an *in situ* grown, epitaxial 8 nm thick Gd film on a $W(110)$ substrate. Differences in the growth conditions and sample properties[12] can lead to changes in the spectral shape of absorption edges and equivalently of the optical constants derived from them.
It is ideal to obtain the optical constants for each sample separately. The total electron-yield measurement is appropriate for non-transparent samples such as ours, keeping in mind to correct the data for the finite escape depth of excited electrons and the projection of the magnetization onto the photon polarization-axis,

[10] As mentioned before: This also happens if we increase $|\gamma_0|$.
[11] X-ray illumination leads to ionization, i.e. photoemission. A neutralizing current counteracts the charge-up of the sample. This current is proportional to the photon absorption, if all excited electrons escape the sample.
[12] E.g. changes in the chemical environment, local density variations

both depending on the incidence angle.
Furthermore it is mandatory to correct for the energy-dependent beamline intensity, as mentioned before. Our approach of a separate measurement of the energy dependence in the scattering chamber can be improved by a simultaneous measurement of the incident intensity and X-ray reflectivity. The beamline possesses a mesh before the scattering chamber for this purpose. But the signal it measures is influenced by the magnetic field in the chamber and thus unusable for normalization in our experiment. If one increases the distance between mesh and magnet, the influence will be quadratically reduced.

5.5 Conclusion

Overall we observe a complicated behavior of the Fe and Gd magnetization leading to the various temperature-dependent hysteresis forms in Fig. 5.5. They are the result of a twist of the magnetization direction in both films as proposed by Camley and Tilley [10]. Theory predicts a twist angle on the order of 0.1° between individual atomic layers, the exact value depending on temperature.
The twist of the magnetization is dictated by the interplay between the antiferromagnetic alignment of Fe and Gd moments at the interface, the Zeeman energy in the external field, and the temperature-dependent magnetic moment of Gd. The Fe moment is nearly constant in the temperature range between 100 K and 300 K. The magnetic moments of Gd at the interface layer are pinned antiparallel to those of the Fe layer. The Gd interface layer is therefore fully magnetized and aligned antiparallel to the Fe layer independent of temperature.
The magnetization of both layers is always aligned in-plane but rotates in plane around the film normal as a function of temperature. With the XMCD in reflection measurement we probe the magnetization of the whole Fe film. For Gd we measure mainly the interface magnetization. Note that we only measure the field component along $\vec{H}$. Our observations are as follows.

300 K: The Fe magnetization is aligned parallel to the external magnetic field $\vec{H}$. The Gd film is only magnetized at the interface (since $T > T_{C,Gd}$) due to the antiferromagnetic coupling to the Fe film. We observe rectangular hystereses in Fig. 5.5.

238 K: Close to the compensation temperature the Gd and Fe magnetizations have almost the same value. Therefore, the magnetizations of the Gd and Fe interface layers are aligned antiparallel and oriented nearly perpendicular to the external field. To reduce their Zeeman energy the magnetization direction of both layers is twisted into the field direction with increasing distance from the interface. The average twist angle of the Fe film rotates with increasing H into the field direction and amounts to $\gamma_{Fe} = (60 \pm 1)°$ with respect to $\vec{H}$ at 100 mT, i.e. a tilt of 30° from a perpendicular orientation. The magnetization of the Gd film is only

twisted to $\gamma_{Gd} = -(94 \pm 2)^\circ$, i.e. 4° from a perpendicular orientation, since we only probe the interface layer. For Gd we expect a stronger overall twist since the Gd magnetic moments exhibit a strong temperature dependence, which reduces the exchange energy contribution at elevated temperatures.
Both Gd and Fe hystereses recorded at 238 K show a behavior similar to magnetization along a hard axis. This is typical if the preferred magnetization direction and external field are not along the same direction.

100 K: At low temperature the overall magnetization of the Gd film is larger than that of the Fe film ($M_{Gd} \approx 1.4 M_{Fe}$). Both magnetization directions are again aligned nearly perpendicular to the external field. The dominating Gd component shows an average twist angle of $\gamma_{Gd} = -(81 \pm 3)^\circ$ to the external magnetic field at 100 mT, i.e. −9° from a perpendicular orientation. This angle is approximately the same in remanence. Here the Fe film magnetization is aligned antiparallel to the Gd film with an opposite twist of around 9°. With increasing H to 100 mT the average magnetization of the Fe film aligns nearly perpendicular to the field direction with $\gamma_{Fe} = (89 \pm 1)^\circ$. We expect that the overall magnetization of the Gd film rotates with a comparable twist into the field direction.

In order to determine the magnetic profile of the twisted state as a function of depth within the film, we performed a XRMR study. It includes the recording of $\theta - 2\theta$ scans for several energies around the Gd M_5 edge and temperatures as well as the subsequent analysis by comparison with simulated scans. The simulations were performed with the DYNA software.
First of all, our results reveal the microscopic structure of the film. These values are used throughout this work. Secondly, we formulated a model for the dependence of the Gd sublayer magnetization length and orientation on the depth within the layer. We used this model as a basis for the simulation of the magnetic depth profiles. Unfortunately we did not succeed in achieving a quantitative agreement between simulation and experiment. This discrepancy can be partially attributed to the fact that the optical constants for Fe and Gd were not determined from the same sample. Instead, we used values from the literature, which might exhibit a different energy dependence. This is especially crucial close to the resonance edges. Nevertheless our results clearly show that the projection of magnetic moments onto the magnetic field axis changes sign over the thickness of the Gd layer. This is a footprint of the twisted state. And it shows that the twist length in Gd can be estimated similar to the thickness of a Bloch domain wall, as proposed by Camley [11].

Chapter 6

Magnetization dynamics of Y/Fe/Gd

To unravel the microscopic processes in the ultrafast magnetization dynamics of the ferrimagnetic bilayer Fe/Gd, we studied its transient magnetization in XMCD in reflection at the FemtoSpeX slicing facility. The experimental setup is shown in Fig. 6.1 and detailed in Ch. 4.

We will start describing the acquistion of our experimental data as well as their treatment in Sec. 6.1 and evaluation procedure in Sec. 6.2, followed by the optical properties of the film in Sec. 6.3.
Afterwards we shall take a look at the magnetization dynamics of the Y/Fe/Gd film at different temperatures in Sec. 6.4. At room temperature we find a rapid demagnetization of both layers on similar timescales, different from the magnetization dynamics found in pure layers of both elements. Especially Gd exhibits a drastically increased demagnetization rate and shows signs of a partial switching. The magnetization dynamics at 100 K on the other hand, exhibit no ultrafast components. But we observe an increase of the observable magnetization component of the Fe layer, while that of Gd vanishes completely.
Finally at a temperature of 235 K close to the magnetic compensation point of

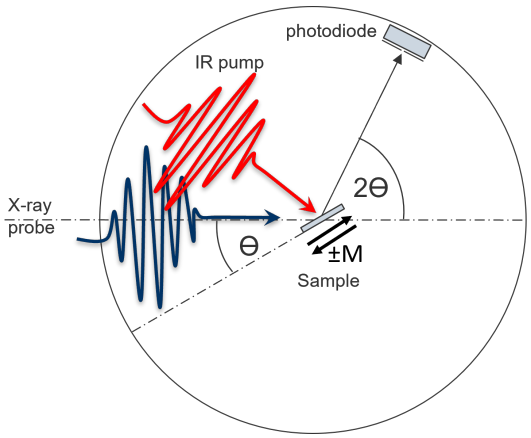

Figure 6.1: *Sketch of the experimental setup. The sample is mounted on a rotatable manipulator in the rotational center of the scattering chamber at an angle of θ to the incident X-ray beam. The IR-pump pulse is incident almost collinear to the X-ray-probe pulse. The deviation is an angle of 1.5° perpendicular to the scattering plane. After scattering off the sample, the probe pulse is detected by a photodiode at an angle of 2θ, while the pump pulse is blocked.*

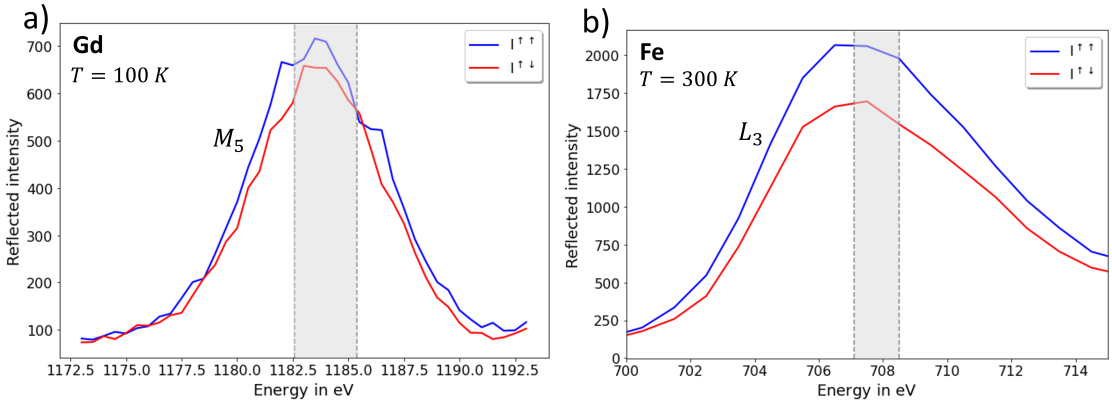

Figure 6.2: *X-ray reflectivity at a) the Gd M_5 edge for $T = 100$ K and b) the Fe L_3 edge for $T = 300$ K, where the XMCD contrast of either layer is largest and its magnetization points along the external magnetic field. These spectra were measured at the FemtoSpeX beamline in slicing mode and are therefore subject to energy broadening. The grey areas mark the energy range in which our dynamic data were recorded. The labels $I^{\uparrow\downarrow}$ and $I^{\uparrow\uparrow}$ denote the orientation of the external magnetic field either antiparallel or parallel to the net magnetization of the sample at this temperature, respectively.*

the two layers, we observe a switching of the observable magnetization component of the Gd magnetization, while that of Fe does not change its sign. The so created transient ferromagnetic like state lasts for ca. 10 ps. We combine our insights from Chs. 4 and 5 with these dynamic observations and conclude that both the twisted state of the bilayer magnetization as well as spin currents between Fe and Gd play a crucial role. With these ingredients we obtain remarkably fast dynamics of this switching behavior on a sub-picosecond timescale, rather than on a timescale of several picoseconds as previously found in FeGd alloys [9] and Co/Gd bilayers [7].

6.1 Data acquisition and treatment

During the experiment, the photon energy was readjusted several times to record the magnetization dynamics at the Gd M_5 and Fe L_3 edges, respectively. The apparent peak position experiences shifts during the experiment, as the zone plate monochromator is changing between Gd and Fe energies. These shifts were corrected in the analysis by comparison to the DYNA-simulated X-ray reflectivity of the absorption edges at the respective incidence angle. Because such treatment is not feasible during the experiment, we worked with several slightly different positions in the absorption edge. Figure 6.2 shows exemplary X-ray reflectivity scans of the Gd M_5 edge at 100 K and the Fe L_3 edge at 300 K with the energy range in which we worked marked in grey. These ranges result from the different chosen photon energies as well as the uncertainty in the size of the spectral shift.

To obtain reasonable statistics, it is necessary to invest long integration times into

the acquisition of each data point. The reasons are twofold. Due to the presence of the twisted state at most temperatures, we have seen e.g. in Subsec. 5.3 that the XMCD contrast can be drastically diminished. Furthermore we have learned in Subsec. 3.1.1 that the femtoslicing process reduces the intensity of the X-ray beam by a factor of 10000 and thus requires proportionally longer integration times to obtain the same statistics as in a regular scattering experiment. For practical purposes we choose an integration time of 5 s per point, resulting in a reasonable recording time of around 30 min per delay scan. This allows for an on-the-fly evaluation of the statistics and reduces the amount of lost data points in the case of an unnoticed beam loss or change during measurement.
By performing multiple scans and combining the data, we improve the signal-to-noise ratio. To reconcile scans spanning over different delay windows or using different delay step sizes, the data have been binned. We combine the scans by calculating the average of the values for a given delay bin. This is done for each channel $I_p^{\uparrow\downarrow}$, $I_{up}^{\uparrow\downarrow}$, $I_p^{\uparrow\uparrow}$ and $I_{up}^{\uparrow\uparrow}$ respectively. The uncertainty is determined as the standard error of this average. The calculation of the dichroic XMCD contrast from the four channels follows equivalently to the Gd layer. The procedure can be reread in Subsec. 4.1.1.

6.2 Fit model

Similar to our considerations in Ch. 4 we apply a phenomenological fit model to the data. We start with the sum of an exponential decay with a time constant τ_1 and prefactor M_1 and an exponential recovery function with a time constant of τ_3 and a prefactor of M_3, equivalently to the fit function presented in Subsec. 4.1.2

$$M'(t') = M_1\Theta(-t') + \Theta(t')\left(M_1 \mathrm{e}^{-\frac{t'}{\tau_1}} + M_3(1-\mathrm{e}^{-\frac{t'}{\tau_3}})\right) . \tag{6.1}$$

The Heavyside step function leads to a constant value M_1 before the probe pulse arrives and lets the demagnetization start with its arrival. We convolve $M'(t')$ with a Gaussian function of width $\sigma = 150$ fs to account for broadening effects due to the pulse lengths of the pump and probe pulses, which sets our time resolution. The resulting fit function after normalization is given by

$$\begin{aligned} M(t) = M_0 + \frac{1}{2}\Bigg[& M_1 e^{\frac{\sigma^2}{2\tau_1^2}} e^{-\frac{t}{\tau_1}} \operatorname{Erfc}\left(\frac{\sigma^2 - t\tau_1}{\sigma\sqrt{2}\tau_1}\right) \\ & - M_3 e^{\frac{\sigma^2}{2\tau_3^2}} e^{-\frac{t}{\tau_3}} \operatorname{Erfc}\left(\frac{\sigma^2 - t\tau_3}{\sigma\sqrt{2}\tau_3}\right) \\ & + M_3\left(1 + \operatorname{Erf}\left(\frac{t}{\sigma\sqrt{2}}\right)\right)\Bigg] \\ & + M_1 \frac{1}{2} \operatorname{Erfc}\left(\frac{t}{\sigma\sqrt{2}}\right) . \end{aligned} \tag{6.2}$$

We include a variable offset along the relative magnetization axis M_0. Our normalization thus yields a level of $M_0 + M_1$ before $t = 0$ and of $M_0 + M_3$ as the recovery level reached at long times.

6.3 Pump-probe penetration depth

Similar to the case of the pure Gd film, discussed in Sec. 4.2, we want to analyze the distribution of intensity in the Y/Fe/Gd film for both the pump and probe beams. The situation is complicated by the additional interfaces between the Y and Fe as well as the Fe and Gd layers, at which partial reflection occurs. This leads to interference effects, which change the intensity profile.
We will again start by looking at the IR-pump beam and simulate both the intensity as well as the absorbed intensity as a function of penetration depth. Since the interaction between Fe and Gd is expected to play a crucial role in the magnetization dynamics of the bilayer, it is very useful to see if and where the pump effect can be located.
On a similar notion, we are interested in the sensitivity of the X-ray-probe at different depths in the film. This information is provided by our simulation in the second subsection.

6.3.1 The IR-pump pulse

As we did for the 60 nm Gd film in Subsec. 4.2.1, we would like to quantify the amount of energy that the pump pulse deposits in the different layers of the sample, which will aid us in interpreting our experimental findings. Therefore we want to determine the absorbed fluence by simulating the intensity profile and absorptances within the film using the IMD software of David Windt [79].

The complex index of refraction for our infrared pump pulse is obtained from the "Handbook on optical constants of metals" by Adachi [89]. The Gd index was already used before. The indices for Fe at 300 K were collected by Adachi from several sources to cover a wide wavelength range. Unfortunately the crystallinity is not specified.

With IMD we calculate the field intensity as a function of depth in the Y/Fe/Gd layer for p-polarized light with a wavelength of $\lambda = 800$ nm at an incidence angle of $\theta = 5°$, shown in Fig. 6.3 a). The thickness and roughness of each layer is set according to our findings in Sec. 5.4, while the W(110) substrate is assumed to be semi infinite. Once again we find an exponential decay according to the Lambert-Beer law.

We proceed as in Subsec. 4.2.1 and calculate the absorbed intensity in each layer, by integrating Eq. 4.6 over dz [90]. The field intensity is treated as a continuous function in z and the refractive index is constant within each layer. Interface

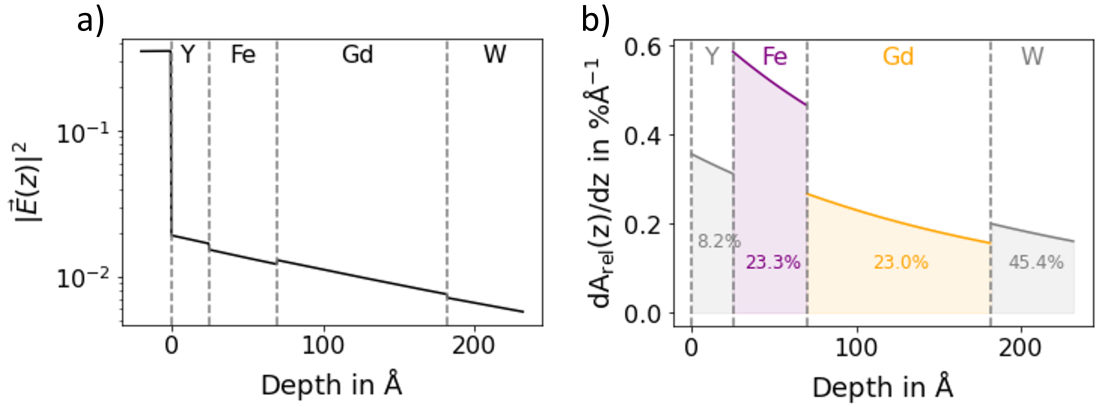

Figure 6.3: *a) Field intensity $|\vec{E}(z)|^2$ as a function of depth in the Y/Fe/Gd film on a semi-infinite W(110) substrate for an incident wavelength of* 800 nm *at an angle of* 5°*. Note the logarithmic scale of the intensity.*
b) Absorption profile in the Y/Fe/Gd film on a semi-infinite W substrate. The total absorption ratio for each layer is given in the shaded area and refers to the total ***absorbed*** *fluence.*

roughnesses were only taken into account for the field intensity calculation with IMD, but neglected in the integration.
For our setup we find that 62.8% of the incident power are absorbed in the sample[1]. The absorption profile within the layer is shown in Fig. 6.3 b). It shows the relative absorption per unit length $dA(z)/dz$, which is proportional to the integrand of Eq. 4.6. The calculation was performed in the same manner as described in Subsec. 4.2.1. Figure 6.3 b) also shows the full value A_i for each sublayer in percent. The higher absorptance of Fe compared to Gd results in an equal total absorption of the pump light in both layers, despite their different thicknesses.

6.3.2 The X-ray-probe pulse

Now, in order to judge the depth sensitivity of the probe pulse, we perform an IMD simulation with the X-ray photon energy and obtain the intensity profile $|\vec{E}(z)|^2$. Note that the profiles differ from those presented in Ch. 5, as the FemtoSpeX setup has a smaller energy resolution. From the energy spectra we recorded, we determined a Gaussian energy broadening with a width of $\sigma = (1.8 \pm 0.1)$ eV at the Gd M_5 edge and $\sigma = (1.55 \pm 0.15)$ eV at the Fe L_3 edge.

Figure 6.4 shows IMD simulations of the field intensity at the Gd M_5 and Fe L_3 absorption edges in a Y/Fe/Gd multilayer film on a semi-infinite W substrate. We performed simulations of the intensity profile for photon energies at the edges of the experimentally used energy range that we discussed earlier to likewise obtain the edges of our penetration depth.
As we saw for the single elemental film, the intensity of X-rays at the M_5 edge within

[1] In absorptances: $a_f = 0.372$ for the Y/Fe/Gd film and $a_s = 0.285$ for the semi-infinite W substrate

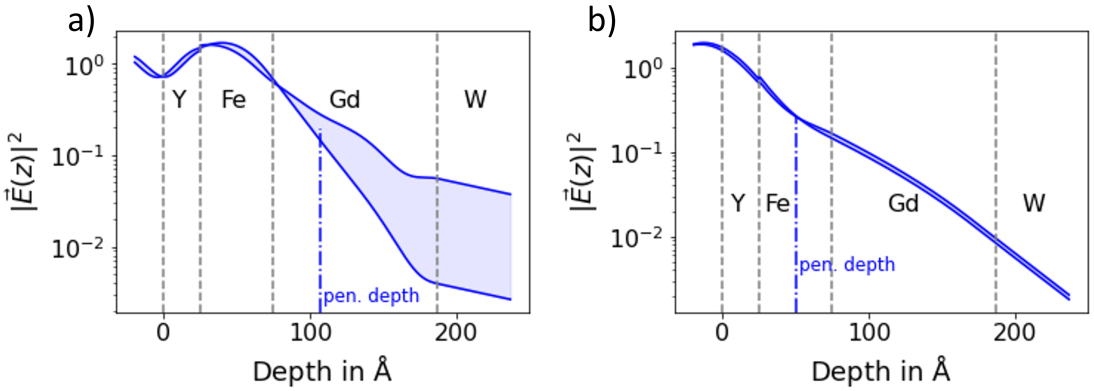

Figure 6.4: *a) Intensity profile of X-ray beams with photon energies in the range of* 1182.6 eV − 1185.4 eV.
b) Intensity profile of X-ray beams with photon energies in the range of 707.4 eV − 708.5 eV.
In both cases the X-ray beam is incident at an angle of $\theta = 5°$ *on a Y/Fe/Gd film on a semi-infinite W substrate. Depth is measured along the surface normal. The penetration depth at which the intensity has dropped by a factor of* $1/e$ *is marked by the dash-dotted lines.*

the Gd layer and at the L_3 edge in the Fe layer decays mostly exponentially with $1/e$ penetration depths of (32 ± 11) Å and (24.8 ± 2.3) Å on average, respectively. But we can see once more e.g. in the Y layer around the M_5 edge that interference effects have a strong influence on the intensity profiles. What we can learn from Fig. 6.4 is that we preferentially probe the vicinity of the Fe-Gd interface in Gd and the Y-Fe interface in Fe, corresponding to the vectors $\vec{M}^I_{Gd}$ and $\vec{M}^{top}_{Fe}$ in Fig. 5.3 b). We will show the temperature dependent orientation of the magnetizations as we go through the time-resolved datasets.

6.4 Temperature dependent magnetization dynamics

6.4.1 Dynamics at T = 300 K

From our simulation of the pump-pulse absorption profile in Subsec. 6.3.1 we can determine that the absorbed fluence in the combined Fe/Gd bilayer is 4.4 $\frac{\text{mJ}}{\text{cm}^2}$ of the incident 15 $\frac{\text{mJ}}{\text{cm}^2}$. I.e. half of this is absorbed in each layer with the exponential profile we have seen in Fig. 6.3. A fluence of 4.3 $\frac{\text{mJ}}{\text{cm}^2}$ is likewise absorbed in the W substrate and only 0.8 $\frac{\text{mJ}}{\text{cm}^2}$ in the Y capping layer.

The time-dependent evolution of the magnetization after excitation with an IR pump pulse at room temperature shows an ultrafast demagnetization of Fe. The Gd layer experiences an ultrafast reduction of the magnetization up to a zero crossing, i.e. a switching around 2 ps after excitation up to a relative reversed

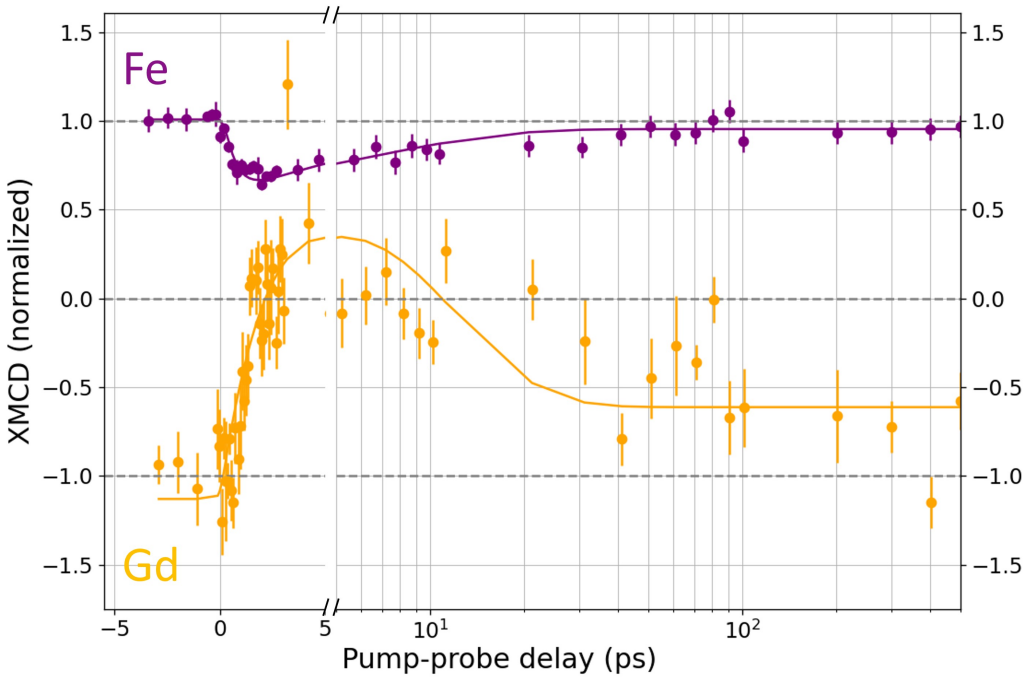

Figure 6.5: *Transient magnetization dynamics of the Y/Fe/Gd film after excitation with a* 1.5 eV *pump pulse. The absorbed fluence in Fe and Gd is* 2.2 $\frac{\text{mJ}}{\text{cm}^2}$ *each, while the W substrate absorbs* 4.3 $\frac{\text{mJ}}{\text{cm}^2}$*. The base temperature is* 300 K*. The normalized Gd magnetization is multiplied by a factor of* -1 *to show the orientation in the external magnetic field.*

magnetization of 25% before relaxation to the initial state. This leads to a transient ferromagnetic like state as seen in Fig. 6.5.
For the fitting we consider the normalized magnetization, without the sign that reflects the orientation in the external field in Fig. 6.5. Because there are strong correlations between the fit parameters, the values of the prefactors $M_{1,3}$ can vary widely. Their range was used to determine the uncertainty intervals of the time constants $\tau_{1,3}$.

	τ_1 (ps)	τ_3 (ps)
Gd	3.4 ± 0.4	7.0 ± 2.4
Fe	0.7 ± 0.3	7.8 ± 3.6

Table 6.1: *Resulting fit parameters for the magnetization dynamics of Fe/Gd at* $T = 300$ K *and an absorbed fluence of* 4.4 $\frac{\text{mJ}}{\text{cm}^2}$ *in the bilayer.*

In contrast to experiments on pure Gd films, the timescale of the Gd magnetization dynamics in our sample only displays a single intermediate timescale. We recall that the magnetization dynamics of a pure 10 nm Gd film exhibit a double-exponential decay both in ARPES and XMCD experiments. On the one

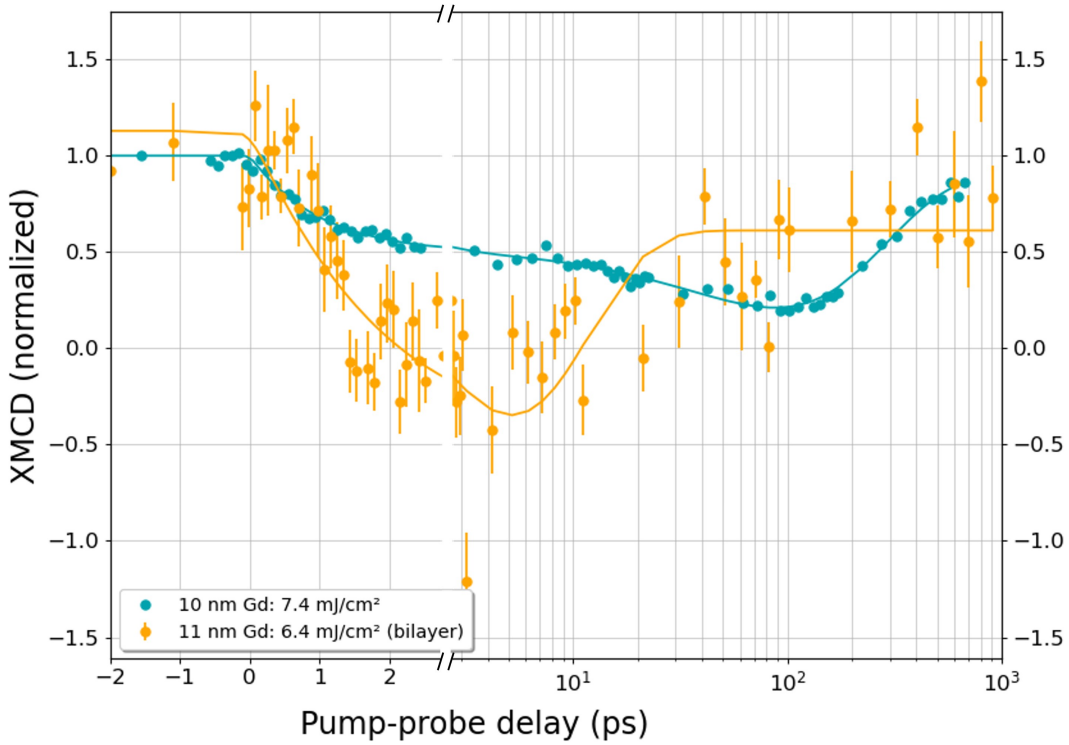

Figure 6.6: *Comparison of the magnetization dynamics of the Gd layer in our bilayer film with the* 10 nm *Gd film investigated by Bobowski et al. [20]. The latter was measured at the M_5 absorption edge at an energy of* 1186.3 eV*. The given fluence is absorbed in Gd and W combined, for both films.*

hand Frietsch [2] and Bobowski [20] observed a fast time constant of 0.8 ps, that they attributed to the itinerant $5d6s$ valence electrons. On the other hand a slow time constant was found, which differs somewhat between methods with 14 ps for ARPES [2] and 26 ps for XMCD in reflection [20]. Our analysis of the magnetization dynamics of a 60 nm Gd film suggests that this timescale corresponds to demagnetization by magnon-driven spin currents that are launched close to the Gd/W interface and carried both by the $5d6s$ and $4f$ electron spins, as discussed in Ch. 4.
The partial switching of our Gd layer is achieved at an absorbed fluence of 2.2 $\frac{\text{mJ}}{\text{cm}^2}$ in Gd. In the work of Bobowski *et al.* [20] full demagnetization was observed for a pure 10 nm Gd film on a W(110) substrate. The incident fluence was 14.1 $\frac{\text{mJ}}{\text{cm}^2}$, which can be translated to a similar absorbed fluence[2] of (2.6 ± 0.2) $\frac{\text{mJ}}{\text{cm}^2}$, with the help of IMD. Equivalently to Ch. 4, we show the comparison between these two experiments in Fig. 6.6. In the figure we look at the combined absorption of Gd and W once more, as Bobowski *et al.* did. It is 7.4 $\frac{\text{mJ}}{\text{cm}^2}$ for the pure Gd film and 6.4 $\frac{\text{mJ}}{\text{cm}^2}$ for Gd in the bilayer.

Fe on the other hand reduces its magnetization by merely 30% on a sub-picosecond timescale.

[2]The absorbtance is 20%.

We can compare this with the MOKE experiments by Carpene *et al.* [104]. They investigated an epitaxially grown Fe(100) film with a thickness of 7 nm grown on MgO(100).

Using an IMD simulation, we can estimate an absorptance of about 34% for this sample, assuming an incidence angle of 40°. At the highest incident fluence of 6 mJ/cm^2, the sample will thus absorb about 2 mJ/cm^2. Carpene *et al.* state a demagnetization time of (75 ± 8) fs for this dataset, one order of magnitude faster than in our experiment. The magnetization quenching of 30% is very similar. This is in line with the equal absorbed fluences in both experiments.

Another close comparison can be drawn to the all-optical switching experiments by Radu *et al.* on the ferrimagnetic alloy GdFeCo [9]. The Fe and Gd magnetic moments in the Fe/Gd bilayer at 300 K are collinear and antiparallel as in [9]. With an incident fluence of 4.4 mJ/cm^2 they observed all-optical switching at 83 K. The time constants of the magnetization dynamics in Fe and Gd show a distinct difference with $\tau_{Fe} = (100 \pm 25)$ fs and $\tau_{Gd} = (430 \pm 100)$ fs, both faster than the timescales we observe in Fe/Gd.

We can summarize that Gd shows a partial magnetization switching at an increased rate compared to the demagnetization of a pure Gd layer. Fe on the other hand demagnetizes more slowly in the bilayer than it does in a pure layer. The comparison to GdFeCo alloys shows that the magnetization dynamics there are faster than in the Fe/Gd bilayer. We may ask how the interaction between the Fe and Gd layers comes into play here and how it differs from the alloy case.
We know that at this temperature, pure Fe retains 98% of its saturation magnetization according to the Weiss model, while pure Gd is already demagnetized, as seen in Fig. 5.1. The proximity of the transition metal causes a proximity magnetization of Gd above the Curie temperature amounting to about 1-2 monolayers [100]. Fe will thus orient itself parallel to the field and the Gd interface layer antiparallel. We have seen this in our analysis in Ch. 5 and illustrate it in panel a) of Fig. 6.7.

Let us assume that the pump pulse excites spin currents between the Fe and Gd layers, in a similar manner as we discussed in Ch. 4 between W and Gd. The antiferromagnetic alignment of the Fe and Gd spins leads to a more efficient demagnetization than in the Gd/W case. The same principle is responsible for the ultrafast spin dynamics observed in antiferromagnets [105]. Even though the overall demagnetization of the Fe layer is relatively small, it cannot be explained fully by the exchange of angular momentum with the Gd layer. Because Gd possesses only a very limited magnetization in the interface region. The area densities of magnetic moments at 300 K are $\Sigma_{mag,Fe} = (8.8 \pm 0.9) \times 10^{14}\ \mu_B/\text{mm}^2$ for the Fe layer and $\Sigma_{mag,Gd} = (0.92 \pm 0.17) \times 10^{14}\ \mu_B/\text{mm}^2$ for the proximity magnetized Gd interface layer. $\Sigma_{mag,Gd}$ amounts to only 10% of $\Sigma_{mag,Fe}$. On top of that the simulation of our probe pulse intensity in Fig. 6.4 shows that we mostly observe the top of the Fe layer in our experiment, far from the Fe/Gd interface. We thus assume that transfer of angular momentum to the Y capping layer and more importantly to the Fe lattice play additional roles for the demagnetization observed in Fe.

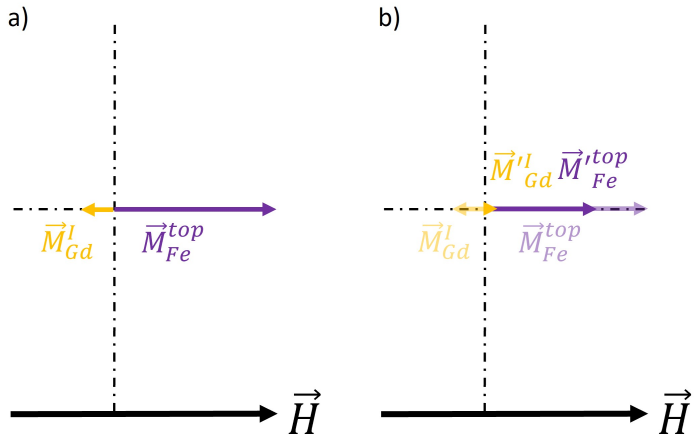

Figure 6.7:* a)** *Configuration of the sublayer magnetizations* $\vec{M}^{top}_{Fe}$ *in Fe and* $\vec{M}^{I}_{Gd}$ *in Gd at* 300 K. *The twist angles are derived from Ch. 5, while the initial state length is arbitrarily chosen.* ***b) *Possible arrangement of the transient sublayer magnetizations at a delay of a few ps. The initial state vectors and components are shown in a lighter shade.*

Both in Fe [104] and Gd (see Ch. 4), ultrafast demagnetization is driven by magnons. The timescale of demagnetization through the exchange of magnetic moments between the layers is therefore given by the ratio of the nm length scale and the nm/ps magnon velocity, as we saw in Ch. 4. The two layers only touch at the interface, so that magnons need to travel through the film to transfer magnetic moments to atomic layers farther away from the interface. We indeed find timescales on the order of picoseconds. The situation is quite different in an GdFeCo alloy, in which the distance between Fe and Gd atoms is always on the order of a few Å. This allows for a more direct and thus faster exchange of magnetic moments, e.g. via electronic exchange scattering.
The comparison with Carpene *et al.* [104] and Radu *et al.* [9] shows that the magnetization dynamics in Fe slow down from 75 fs in pure Fe to 100 fs in GdFeCo to 700 fs in Fe/Gd. It is possible that Fe in the bilayer exhibits faster demagnetization close to the interface, which we are not sensitive to. But the trend suggests that the interaction with Gd may contribute to a slow-down of the magnetization dynamics in Fe.

The transient magnetizations $\vec{M}^{top'}_{Fe}$ and $\vec{M}^{I'}_{Gd}$ are shown in panel b) of Fig. 6.7 together with the initial state magnetizations for comparison. The length of the initial state vectors is arbitrarily chosen, because it cannot be accurately determined. The relative transient change is correct however.
In contrast to our findings, Beens *et al.* [7, 8] describe AOS of a Co/Gd bilayer in which the Gd magnetization similarly stems from the proximity to Co. The difference is that in their model Co demagnetizes completely, unlike our Fe layer. At the interface, exchange of magnetic moments with Gd then nucleates a new magnetic orientation that propagates layer by layer due to the inter-atomic exchange interaction in the Co layer. The relative amount of magnetic moments in both layers is therefore irrelevant for the observation of AOS, as long as the magnetic

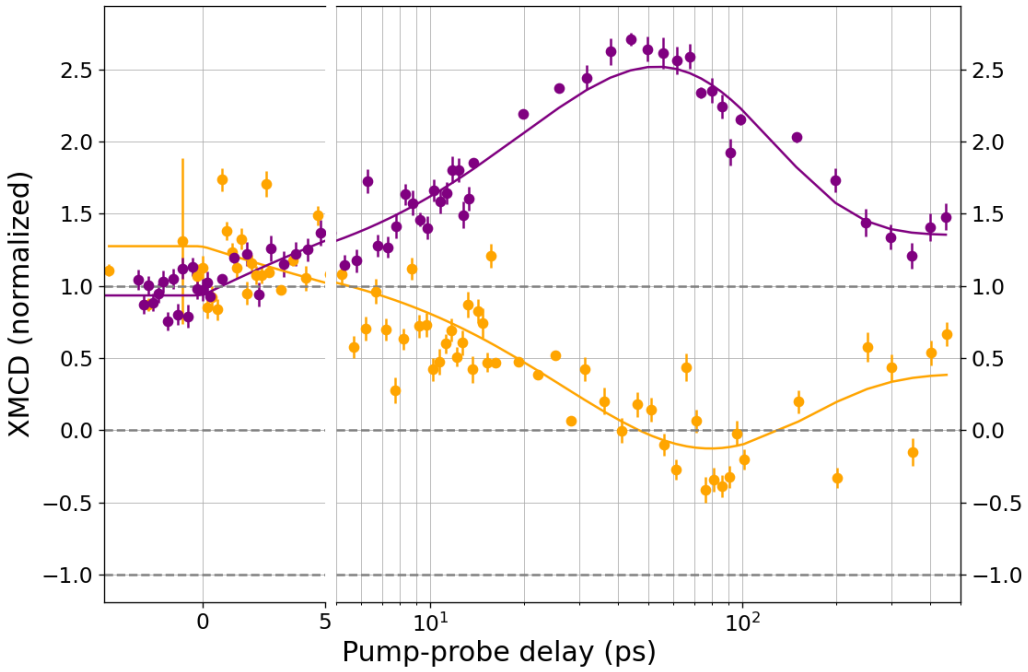

Figure 6.8: *Transient magnetization dynamics of the Y/Fe/Gd film after excitation with a* 1.5 eV *pump pulse. The absorbed fluence in Fe and Gd is* 2.2 $\frac{\text{mJ}}{\text{cm}^2}$ *each, while the W substrate absorbs* 4.3 $\frac{\text{mJ}}{\text{cm}^2}$*. The base temperature is* 100 K.

moments in Gd suffice to switch the Co interface layer.
Using a higher fluence, a full demagnetization of the Fe layer could be reached. It warrants further investigation if all-optical switching of the bilayer follows from this.

6.4.2 Dynamics at T = 100 K

In the next step, the sample was cooled with liquid nitrogen to a base temperature of 100 K, where Gd is strongly magnetized. We have seen in Ch. 5 that Gd is magnetically dominant at this temperature. At 300 K we saw a speed-up of the Gd dynamics compared to single elemental films and a transient ferromagnetic like state. We argued that the small proximity magnetization in Gd lead to a relatively small demagnetization of the Fe layer and possibly inhibited AOS of the film. Thus we are interested in the effects of an increased magnetization in the Gd layer. But we have to take the twisted state into consideration, which we expect from Ch. 5 at this temperature. It is unknown how the twisted arrangement of magnetic moments influences their interaction. On top of this the twisted state is stabilized by the balance of Zeeman energies. And that is prone to change itself due to demagnetization.

The absorbed fluences at $T = 100$ K remain the same as at $T = 300$ K.
In Fig. 6.8 we see a full but slow demagnetization of Gd. Fe does not demagnetize

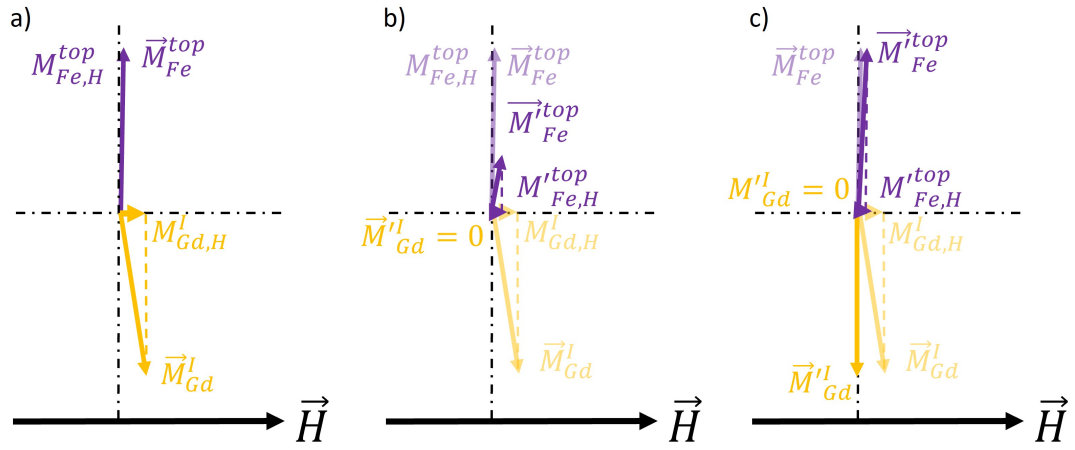

Figure 6.9: ***a)*** *Configuration of the sublayer magnetizations $\vec{M}^{top}_{Fe}$ in Fe and $\vec{M}^{I}_{Gd}$ in Gd at 100 K. The twist angles are derived from Ch. 5, while the initial state length is arbitrarily chosen. The projection $\vec{M}^{top}_{Fe,H}$ is too small to draw it.* ***b)*** *Possible arrangement of the transient sublayer magnetizations after a few ps. $\vec{M}^{I}_{Gd}$ is fully demagnetized, while $\vec{M}^{top}_{Fe}$ is partially demagnetized and tilted towards the external magnetic field.* ***c)*** *An alternative scenario, where the lengths of $\vec{M}^{I}_{Gd}$ and $\vec{M}^{top}_{Fe}$ are constant, but both experience a flop. $\vec{M}^{I}_{Gd}$ away from the external field, $\vec{M}^{top}_{Fe}$ towards it. The initial state vectors and components are shown in a lighter shade.*

at all. Rather, its relative magnetization increases by a factor of 2.6 on a similar timescale as the Gd demagnetization. The enhanced magnetization returns to the initial value within hundreds of picoseconds. To model the behavior we switch the sign of the prefactors to $M_{1,3} < 0$ for Fe.

	τ_1 (ps)	τ_3 (ps)
Gd	45 ± 5	75 ± 15
Fe	31 ± 7	109 ± 50

Table 6.2: *Resulting fit parameters for the magnetization dynamics of Fe/Gd at $T = 100$ K and an absorbed fluence of 4.4 $\frac{\text{mJ}}{\text{cm}^2}$ in the bilayer.*

Going back to Fig. 5.1 and noting the reduced maximum magnetization in Gd, we note that Fe retains its full saturation magnetization at this temperature, while Gd is magnetized to 48% of an ideal Gd layer. If we take the magnetic-moment densities into account and consider the magnetic compensation temperature of (225 ± 15) K, we find that Gd is magnetically dominant. At 100 mT, we measure projections $M^{top}_{Fe,H}$ and $M^{I}_{Gd,H}$ that point along the external magnetic field. But they are small because the magnetization vectors $\vec{M}^{top}_{Fe}$ and $\vec{M}^{I}_{Gd}$ are almost perpendicular to the field, as depicted in Fig. 6.9 a). The twist angles are found to be $\gamma_{Fe}(100\text{ K}) = (89 \pm 1)^\circ$ and $\gamma_{Gd}(100\text{ K}) = -(81 \pm 3)^\circ$.
We note that the twist angle in Subsec. 5.3.3 represents the orientation of the overall Fe magnetization, while the magnetization dynamics are sensitive to the

top Fe layer (cf. Figs. 5.2 and 6.4). The layer by layer twisting towards field alignment we see in Fig. 5.3 then means that the angle between the magnetization that we measure and the magnetic field is smaller in the time-resolved experiment than in the static characterization presented in Ch. 5. We can try to quantify the difference based on the theoretical predictions about the twisted state found in Camley's work [11]. In Subsec. 2.2 we estimated a typical twist length[3] of 100 nm for both layers. We go back to Eqs. 5.10-5.12 and set $x_0 = 100$ nm. Then we simulate the X-ray sensitivity by taking the vector sum of the atomic-layer magnetizations, weighted by the X-ray intensity as given in Fig. 6.4. The result 89° for the entire layer is retained if we set $\gamma_{0,Fe} = 94°$. This fits well with the interface orientation found in Gd. The precise values are not crucial, since we find that the twist angle varies only by 4° over the whole Fe layer and the orientation we are sensitive to in this experiment differs by about 1° from $\gamma_{Fe}(100\,\mathrm{K})$ as found in Ch. 5.

We can argue now that the larger magnetization components of both layers are antiparallel. The magnetic moments may therefore efficiently cancel each other. This is the same argument as for the dynamics at 300 K. However, the larger magnetization component is perpendicular to the field and therefore not detectable to us. We are sensitive only to that component which is parallel for both layers, where the exchange of magnetic moments does not lead to demagnetization.
Instead we see an apparent demagnetization of the Gd layer on a similar timescale as the slow timescale found in the previous investigations of Gd thin films in Refs. [2, 20] and Ch. 4.

There are two explanations for this. The first is, that $\vec{M}^I_{Gd}$ goes to zero, seen in Fig. 6.9 b). Then the balance between the Zeeman energies of both layers changes. The Fe aligned state becomes favorable. The slow timescale of the Fe dynamics indeed matches magnetic field switching and could indicate the transition from the twisted to the Fe aligned state, in which all magnetic moments are collinearly aligned and Fe is rotated in field direction.
Three reasons speak against this picture. Firstly, Gd would exchange magnetic moments with Fe during its demagnetization, leading to demagnetization in Fe as well. On top of that, the larger magnetization in the Gd layer suggests that the demagnetization in Fe should be even stronger than in Gd, given the large magnetic moment per atom in Gd. Secondly, we have seen at 300 K as well as in the literature [2, 20, 104] that Gd tends to demagnetize more slowly than Fe so that the balance of Zeeman energies would transiently rather shift in favor of the Gd aligned state and we should see magnetization dynamics with reversed roles of Gd and Fe. If instead both layers would demagnetize on the same timescale, the twisted state would remain. And thirdly, both Fe and Gd demagnetize on a much faster timescale than the dynamics visible in Fig. 6.8.
This picture therefore seems unlikely.

The second explanation is that $\vec{M}^{top}_{Fe}$ tilts without demagnetizing, as shown in Fig. 6.9 c). We can estimate that an increase of $M^{top}_{Fe,H}$ by a factor of 2.6 from

[3] i.e. to achieve a twist of 180°

a starting angle of $\gamma_{Fe}(100\ \mathrm{K}) = (89 \pm 1)^\circ$ is compatible with a small rotation of $\vec{M}_{Fe}^{top}$ to $\gamma'_{Fe} \approx 87^\circ$. For reasons of angular momentum conservation then, we expect $M_{Gd,H}^{I}$ to go to zero, because $\vec{M}_{Gd}^{I}$ is tilting fully perpendicular to the field. Not because of demagnetization. This picture is compatible with the observed timescales.
One reason speaks against this picture. It seems unlikely that there is no exchange of magnetic moments between Fe and Gd after the excitation. But that process happens on a shorter timescale, as we have seen at 300 K. We have mentioned before that our sensitivity is limited to the small components $M_{Gd,H}^{I}$ and $M_{Fe,H}^{top}$ in which the exchange does not lead to visible changes, because they have the same sign. The perpendicular components, in which we expect an effect, are invisible to us.

A purely thermal heating of the sample could qualitatively explain the observed magnetization flops, because it shifts the balance of magnetic moments further in favor of Fe.

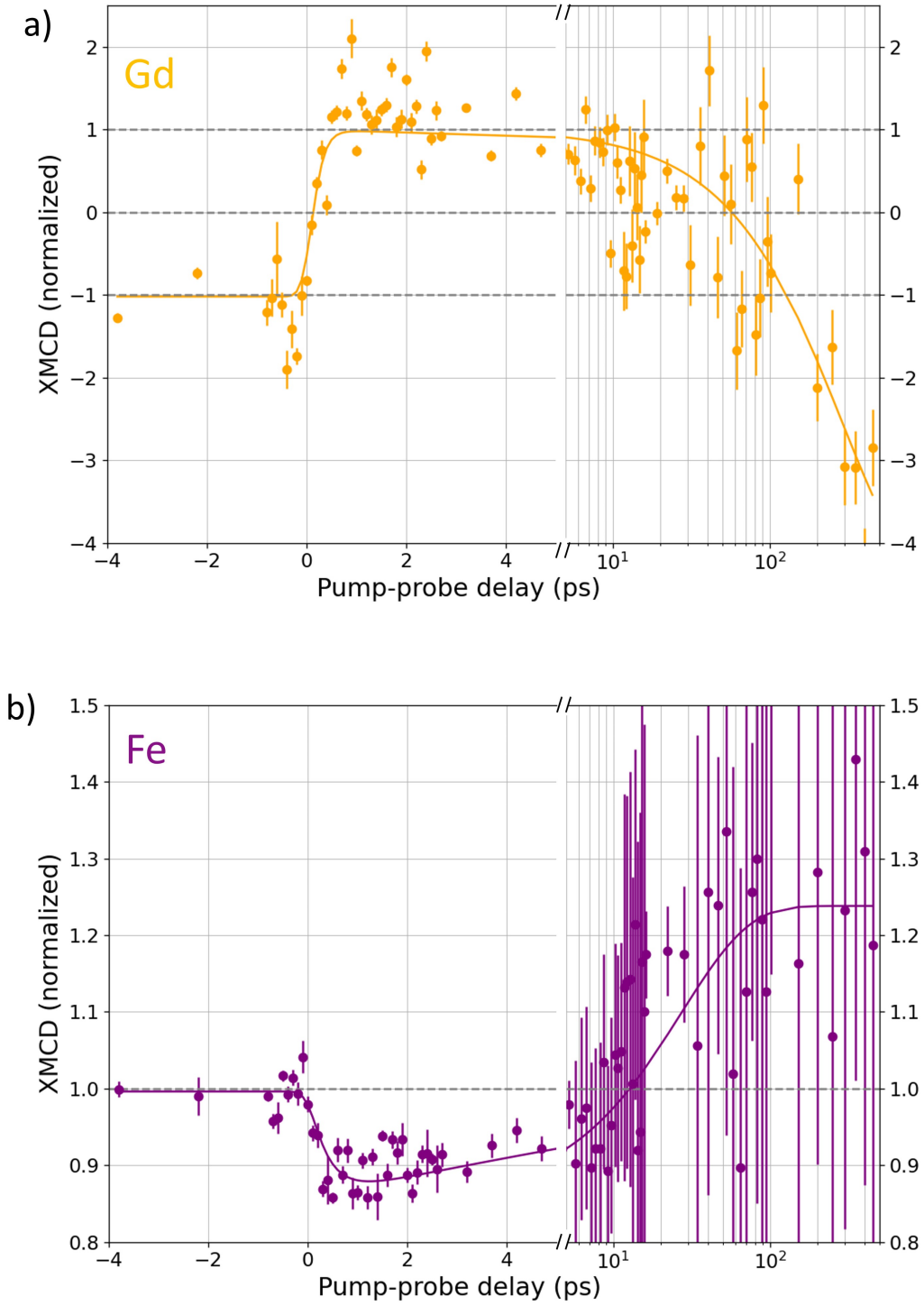

Figure 6.10: *Transient magnetization dynamics of the a) Gd and b) Fe layer of the film after excitation with a 1.5 eV pump pulse. The absorbed fluence in Fe and Gd is 2.9* $\frac{\text{mJ}}{\text{cm}^2}$ *each, while the W substrate absorbs 5.7* $\frac{\text{mJ}}{\text{cm}^2}$*. The base temperature is 235 K. The normalized Fe magnetization is multiplied by a factor of* -1 *to reflect the orientation in the external magnetic field.*

6.4.3 Dynamics at T = 235 K

The final temperature was experimentally chosen to be close to the compensation temperature, where the net magnetization of the bilayer vanishes. Since we are slightly above T_{comp}, Fe is magnetically dominant. More precisely, if we consider Fig. 5.1 and our findings about the reduction of the Gd magnetization once more, we find that Fe is magnetized to 99% of saturation and Gd is already demagnetized down to 31% of the saturation magnetization of an ideal Gd film, at this temperature. Combined with the magnetic moment density of both elements we find very close area densities of magnetic moments of $\Sigma_{mag,Gd} = (8.5 \pm 0.8) \times 10^{14}\ \frac{\mu_B}{mm^2}$ for (11.2 ± 0.2) nm Gd and $\Sigma_{mag,Fe} = (8.9 \pm 0.9) \times 10^{14}\ \frac{\mu_B}{mm^2}$ for (4.8 ± 0.5) nm Fe. In this temperature regime, the twisted state should be even more pronounced than at 100 K [10] and we are interested in whether this changes the effect it has on the dynamic response of the bilayer magnetizations.

The absorption-profile simulation in Subsec. 6.3.1 tells us that the Fe/Gd bilayer absorbs 5.8 $\frac{mJ}{cm^2}$ of the incident fluence of 20 $\frac{mJ}{cm^2}$. As before, half of this is absorbed in each layer and, due to the exponential intensity decay, preferentially in higher atomic layers. The W substrate absorbs 5.7 $\frac{mJ}{cm^2}$ and the Y capping layer 1.0 $\frac{mJ}{cm^2}$.

	τ_1 (ps)	τ_3 (ps)
Gd	0.30 ± 0.15	193 ± 97
Fe	0.36 ± 0.31	27 ± 12

Table 6.3: *Resulting fit parameters for the magnetization dynamics of Fe/Gd at* $T = 235$ K *and an absorbed fluence of* 5.8 $\frac{mJ}{cm^2}$ *in the bilayer.*

The model yields a very rapid time constant for the dynamics. Note, that the relative magnetization of Gd, shown in Fig. 6.10 crosses zero and reaches the full magnitude it had before time zero. It does not demagnetize before remagnetizing in the opposite direction as proposed by Beens *et al.* using the M3TM for Co/Gd bilayers [7, 8].
The orientation and magnitude of the relative magnetization remain constant in this transient ferromagnetic like state for several picoseconds. Around 7.5 ps after the laser excitation, we observe a second zero crossing.

Let us take a look at the Fe dynamics in Fig. 6.10 now. In contrast to the Gd dynamics, no zero crossing can be observed. Instead we merely see a demagnetization by (10 ± 6)%, sustained for 7.5 ps. As in Gd the recovery level appears to be larger than the initial relative magnetization. Statistical scattering of data points is present here as it was in the Gd data. The fit function converges to a recovery level of the relative magnetization of 1.24.

The switching in Gd happens on a sub-ps timescale. As before, we can exclude effects that are related to spin-orbit coupling, because it is negligible in Gd. Only an exchange of magnetic moments between Fe and Gd can explain such

an ultrafast response. Coming from our investigation of Gd in Ch. 4 we further assume that this exchange is mediated via spin currents. And in contrast to the magnetization dynamics at 100 K, the initial state finds Gd and Fe with opposite signs of the magnetization component that we measure. Namely Gd at ca. $\gamma_{Gd}(235\ \mathrm{K}) = -(93 \pm 2)^\circ$ and Fe at ca. $\gamma_{Fe}(235\ \mathrm{K}) = (60 \pm 1)^\circ$ to the external magnetic field. This antiparallel alignment could lead to ultrafast spin current based dynamics in the observed magnetization component. We see the alignment in Fig. 6.11. Again, $\gamma_{Fe}(235\ \mathrm{K})$ corresponds to the twist angle of the entire Fe film, while the relevant orientation is that of the top layer in Fe. But we found in our considerations for the 100 K dataset, that the difference is marginal.

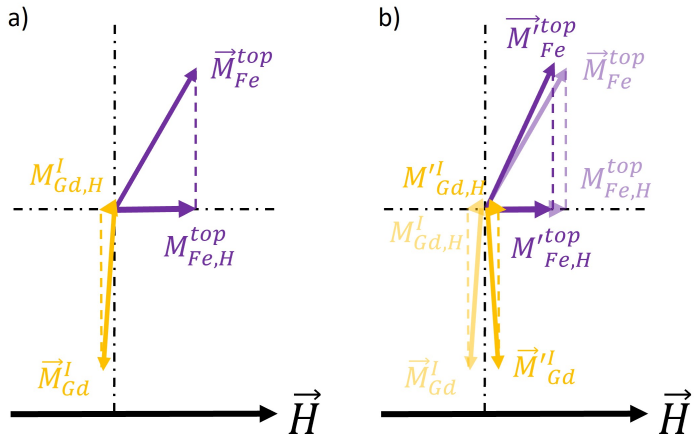

Figure 6.11: a) *Configuration of the sublayer magnetizations $\vec{M}^{top}_{Fe}$ in Fe and $\vec{M}^{I}_{Gd}$ in Gd at 235 K. The twist angles are derived from Ch. 5, while the initial state length is arbitrarily chosen.* ***b)*** *Possible arrangement of the transient sublayer magnetizations after a few ps. The lengths of $\vec{M}^{I}_{Gd}$ and $\vec{M}^{top}_{Fe}$ are constant, but both experience a flop. $\vec{M}^{I}_{Gd}$ towards the external field and $\vec{M}^{top}_{Fe}$ away from it. The initial state vectors and components are shown in a lighter shade.*

Once more, there are two possible pathways for the magnetization vectors in Gd and Fe to explain our observations. There can either be a magnetization flip in which both exchange their magnetic moments and reach a switched state as observed in previous investigations on FeGd alloys [9] or Co/Gd bilayers [7, 8]. Or the magnetization vectors flop by changing their orientation, but not necessarily their length. Because a magnetization flip entails the crossing of zero, it is a possible explanation for the Gd dynamics, but not for the Fe dynamics. Due to the conservation of angular momentum, the two layers may only perform a magnetization flip together, not independently. It is furthermore questionable in how far the exchange of magnetic moments may lead to a magnetization flip in the twisted state, where they are not fully antiparallel. Thus we assume that a magnetization flop occurs. On the one hand, starting at $\gamma_{Gd}(235\ \mathrm{K}) = -(93 \pm 2)^\circ$, the Gd magnetization needs to flop by 6° for the observed change in the magnetization component. We must keep in mind, however, that $\gamma_{Gd}(235\ \mathrm{K})$ is only the orientation of the Gd interface layer. At 235 K we can estimate a twist

by 20° within the Gd layer, according to Eq. 2.1.
For the Fe magnetization on the other hand we can estimate a flop by $3-5°$ from $\gamma_{Fe}(235\ \mathrm{K}) = 60°$ to $\gamma'_{Fe} = 63-65°$, i.e. away from the external field. This follows from the conservation of angular momentum. Due to the high Curie temperature of Fe, its twist length has only a weak temperature dependence and the internal twist at 235 K amounts to ca. 4° just as at 0 K. Thus $\gamma_{Fe}(235\ \mathrm{K})$ is a good representation of the orientation of the magnetization in Fe.

6.5 Conclusion

To conclude this chapter, we have seen that the twisted state that Camley and Tilley proposed [10] has a profound impact on the magnetization dynamics of Fe/Gd bilayers. Table 6.4 shows an overview of the relevant parameters at different temperatures.

	300 K	235 K	100 K
$\tau_{1,Gd}$ (ps)	3.4 ± 0.4	0.30 ± 0.15	45 ± 5
$\tau_{1,Fe}$ (ps)	0.7 ± 0.3	0.36 ± 0.31	31 ± 7
$\tau_{3,Gd}$ (ps)	7.0 ± 2.4	193 ± 97	75 ± 15
$\tau_{3,Fe}$ (ps)	7.8 ± 3.6	27 ± 12	109 ± 50
γ_{Fe} (°)	0	60 ± 1	89 ± 1
γ'_{Fe} (°)	0	64 ± 1	87
γ_{Gd} (°)	-180	-93 ± 2	-81 ± 3
γ'_{Gd} (°)	-180	-87	-90

Table 6.4: *Summary of the temperature dependent values: The demagnetization and recovery times τ_1 and τ_3 and the initial and transient average twist angles γ and γ' of Fe and Gd respectively.*

The magnetization dynamics at 300 K show a demagnetization of Fe with a time constant of (0.7 ± 0.3) ps and a partial switching of Gd with a time constant of (3.4 ± 0.4) ps. While the magnetization dynamics of Gd are significantly faster than in experiments with pure layers on W(110) [2, 20], the Fe magnetization dynamics are slowed down [104].
We explain the behavior with interlayer spin currents, which are highly efficient at demagnetizing the layers due to their antiferromagnetic alignment. Because Gd exhibits only a proximity magnetization close to the Fe-Gd interface at this temperature, it switches partially, but is unable to quench or switch the magnetization in the Fe layer. If Fe were to demagnetize completely, e.g. at larger fluences, we expect that a transport of magnetic moments from the Gd to the Fe interface layer would trigger a layer-by-layer remagnetization to a switched state in Fe, as described for Co/Gd by Beens *et al.* [7, 8].

At 100 K the twisted state arranges the magnetic moments of both layers almost antiparallel to each other and perpendicular to the external magnetic field. We

observe a slow reduction of $M^I_{Gd,H}$ to zero and an increase of $M^{top}_{Fe,H}$ on timescales of (45 ± 5) ps and (31 ± 7) ps, respectively. We believe that, since our observation is limited to the magnetization components $M^I_{Gd,H}$ and $M^{top}_{Fe,H}$ that are parallel to the external field and each other, the exchange of magnetic moments does not lead to demagnetization. The observations can be explained by flops of the magnetization vectors, triggered by thermal heating of the bilayer through the pump pulse. While the Gd magnetization flops to an orientation fully perpendicular to the external field, the Fe magnetization is pulled slightly towards the field direction. This is in line with the temperature dependence of the twisted state.

At 235 K, close to the magnetic compensation temperature around 225 K, the behavior drastically changes. Fe is demagnetized with a time constant of (360 ± 310) fs and $M^I_{Gd,H}$ switches around with a time constant of (300 ± 150) fs. Again, we interpret the behavior as a flop of the magnetization. At this temperature $M^I_{Gd,H}$ and $M^{top}_{Fe,H}$ are sizeable and antiparallel. Thus we are sensitive to the ultrafast exchange of magnetic moments. We believe that it is mediated via spin currents as seen in the pure Gd film in Ch. 4.
Even though we only observe a switching of the component $M^I_{Gd,H}$ due to a magnetization flop, the timescale of that switch is remarkable. Previous investigations of AOS on FeGd alloys [9] and Co/Gd bilayers [7] yielded switching times of several picoseconds. In our Fe/Gd bilayer we are able to observe a switching within 300 fs.

The thicknesses of the Fe and Gd layers play a role here, as well. We have seen that for one orientation, such as at 100 K the ultrafast component of the magnetization dynamics is masked or quenched, while it is present for another. If we reduce the thicknesses of the layers, the twisting is less pronounced. This changes the effective orientation in an experiment in a similar way. We can conclude that the twisted state allows for a multitude of magnetization dynamics, depending on the choice of magnetic field strength, temperature, layer thicknesses and depth sensitivity of the probe. The analysis in this work is a first step. It paves the way for further studies in which the aforementioned parameters are individually varied over a larger range.

Chapter 7

Summary

In the first part of this work in Ch. 4 we shed more light on the ultrafast magnetization dynamics of thin Gd films.
We investigated a 60 nm Gd film in an XMCD in reflection setup and find that it lacks the fast time constant of demagnetization that was observed for 10 nm films in an equivalent setup before [20]. The probe-beam penetration depth in our experiment is ca. 2 nm, while it was ca. 4 nm in the experiment on the much thinner 10 nm film performed by Bobowski *et al.* [20]. Based on this we identify film-substrate interface effects as the driving force behind the fast demagnetization timescale in Gd. We believe that these effects are magnon driven spin currents across the interface, in which unpolarized W $5d6s$ electrons enter the Gd layer. The change of the local spin polarization that they cause triggers the emission of magnons which travel up to the Gd surface. Magnons in Gd can be seen as a coherent superposition of excited $5d$ and $4f$ spin states with a very short coherence time. In this manner the interaction in the W and Gd $5d$ electron systems is imprinted onto the Gd $4f$ spin system which we are sensitive to in XMCD.

The second part of this work is concerned with Fe/Gd bilayers. The ground work for this investigation is laid by our characterization of the material in an equilibrium experiment in Ch. 5. Our findings show clear signs of the so called twisted state, as proposed by Camley and Tilley [10, 11]. In this phase, the magnetic moments of both sublayers are tilted almost perpendicular to the external magnetic field at the interface and show an internal layer-by-layer twisting towards the field with growing distance from the interface.
Hysteresis measurements of Fe/Gd have proven an effect of the interaction between Fe and Gd that can be explained with this twisted state very well. From these data we could extract the twist angles of the overall sublayer magnetizations. We can also clearly see that Gd retains a magnetization well above its Curie temperature when in proximity to Fe, as established in the literature [98–101].
Furthermore we have performed an XRMR study of the structural and magnetic depth profile of the bilayer to uncover the microscopic structure of the twisted state. This method has proven very precise for the determination of the structural parameters of the sample. The magnetic structure could not be resolved due to an

insufficient match between the optical coefficients used for our simulations and the coefficients of the investigated material. Nevertheless, our analysis suggests the presence of sublayer magnetizations both parallel and antiparallel to the external magnetic field in Gd, hinting at the twisted state. Obtaining a more detailed spatial image of the twisted state is one of the most interesting goals for the future.

Finally in Ch. 6 of this work we have studied the magnetization dynamics of Fe/Gd bilayers at different temperatures in a time-resolved XMCD experiment in reflection. In contrast to many experiments that use MOKE to investigate all-optical switching, our experiment is element-specific. We can therefore get a much more in-depth picture of the dynamics within the sample. Interestingly, the twisted state causes quite diverse responses to the ultrafast stimulus of an IR laser pulse depending on temperature and we have seen that the analysis and interpretation of these dynamics are rather complex.
At 300 K, where the Fe and Gd layers are still collinearly aligned, both Fe and Gd show dynamics on timescales of 0.7 ps and 3.4 ps respectively. It is noteable that the Gd dynamics show an intermediate picosecond timescale between the fast subpicosecond and slow, tens of picoseconds, timescales of pure Gd films. Furthermore we observe a partial switching of the Gd layer and demagnetization of the Fe layer by 30%, leading to a transient ferromagnetic like state. We attribute this behavior to the exchange of magnetic moments between Fe and Gd via spin currents similar to, but more efficient than, the magnetization dynamics of the 60 nm Gd film. Because the proximity magnetization of Gd at the interface amounts to only 10% of the magnetization in the Fe layer, a switching of Fe is not possible. We predict that all optical switching becomes possible at higher absorbed laser fluences in the Fe film.
At 100 K the twisted state is well established. Both layers have an almost perpendicular alignment to the external magnetic field. The layer-by-layer tilting towards field alignment leads to components in field direction for both layers. Because our experiment is only sensitive to these components, an exchange of magnetic moments does not lead to demagnetization or switching here. Instead we see the effect of thermal heating by the IR pulse. As the sample temperature increases, we move towards the Fe aligned state in the phase diagram. The Fe magnetization therefore tilts by a small amount of 2° further towards the external field. The Gd magnetization tilts away from the field accordingly and reaches a perpendicular alignment. We observe that the Fe magnetization component increases with a time constant of 31 ± 7 ps, while the Gd component vanishes with a time constant of 45 ± 5 ps.

Finally at 235 K, close to the magnetic compensation point of $T_{comp} = 225$ K, we do observe a full switching of the Gd XMCD contrast with a time constant of 300 fs. The Fe signal however demagnetizes only by around 15% with a time constant of 360 fs and does not switch. The similarly element-specific experiments by Radu *et al.* on FeGd [9] have shown that the magnetizations of both elements switch, and on a timescale of several picoseconds. The different behavior of our

bilayer is understandable in the context of the twisted state.
As before, we find an initial state in which both magnetization vectors are oriented almost perpendicular to the external field. The small components along the field, which we observe, exhibit opposite signs. Upon excitation, the exchange of magnetic moments leads to a very efficient change of both components. Once more we believe that the magnetization vectors themselves change their orientation, but not necessarily their length. In this picture, Gd flops towards the external field and Fe away from it.
The switching of only a component of the magnetization proves to be much faster than the switching of the overall magnetization that was observed in FeGd [9] and Co/Gd [7]. And it requires less transfer of angular momentum. Furthermore, we see that Fe/Gd and similar synthetic ferrimagnets offer a unique possibility to tune the magnetization dynamics *in situ*. By changing the temperature or external magnetic field strength, we change the twisted state. Thereby we change the orientation of the magnetization vectors in Fe and Gd, which has dramatic effects on the transient exchange of magnetic moments between them.

Appendix A

Energetic broadening

In Chs. 4 and 6 we investigated the magnetization dynamics of Gd and Fe/Gd in an X-Ray scattering setup. To resolve ultrafast processes, the setup is located at the FemtoSpeX facility. We saw in 3.1.1 that we obtain a suitable time resolution at the cost of our energy resolution. This will in turn influence our simulation of the X-ray penetration depth. Since the exact energy resolution varies with the chosen photon energy as well as the size of the monochromator exit slit, it needs to be determined on a case by case basis.
In the following we will go through the necessary steps to determine the energy broadening and apply it to the optical coefficients that are used to simulate the X-ray intensity in the film. We will do so on the example of the 60 nm Gd film presented in Ch. 4.

A.1 Energy spectrum

In each experiment, we have recorded energy spectra of the sample. In the case of Gd these are the $M_{4,5}$ edges, in Fe the $L_{2,3}$ edges. The energy broadened spectrum I_b is given as a convolution of the form

$$I_b(E) = \frac{1}{\sigma\sqrt{2\pi}} \mathrm{e}^{-\frac{1}{2}\frac{x^2}{\sigma^2}} * I_n(E) \ . \tag{A.1}$$

$I_n(E)$ is the energy spectrum with the natural line width. It is convoluted with a Gaussian of width σ. We use the DYNA software to simulate I_n for the sample structure at hand. This is shown in Fig. A.1 for the M_5 edge of Gd in the 60nm film investigated in Ch. 4.

The experimentally observed energy spectrum is shown in black. In green we see the simulated spectrum I_n with the natural linewidth. We obtain a good agreement between the simulated spectrum I_b and the experimental one, if we apply a broadening of $\sigma = (2.0 \pm 0.1)$ eV. This is done in a Python code using the function "broadGaussFast" of the "PyAstronomy" package. It requires the

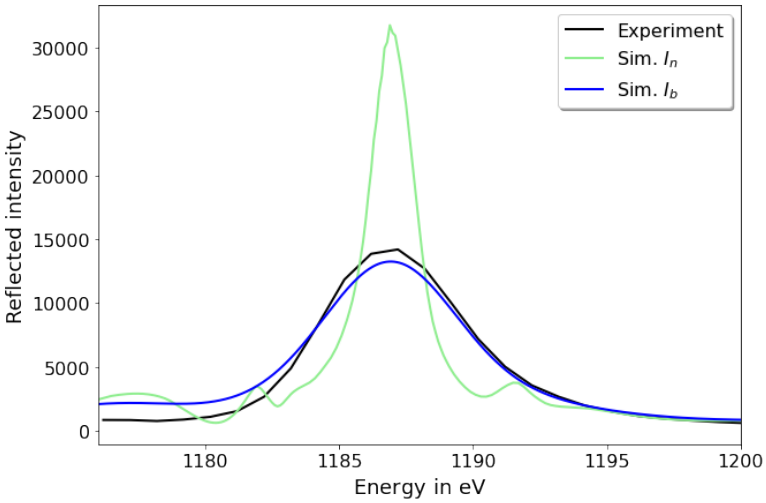

Figure A.1: *The simulated M_5 reflection spectrum of a 60 nm Gd film on a W substrate (green) compared to the experimentally observed reflection spectrum (black) at the FemtoSpeX slicing facility. Broadening the simulated spectrum by (2.0 ± 0.1) eV results in a good match to the experimental data.*

data points to be strictly equidistant, which is generally not the case. But it is readily accomplished with a linear interpolation of the datasets with the function "interp1d" from the "Scipy.interpolate" package. Artefacts are not to be expected, because we only interpolate betweeen the very tightly spaced points of the original dataset.
Figure A.1 also illustrates how the absorption in the resonance is reduced due to the energetic broadening. This affects the penetration depth of the X-ray probe pulse.

A.2 Optical coefficients

In the next step we need to apply an equivalent broadening to the optical coefficients as a function of wavelength, as they are used in the IMD software. We take the peak energy of $E = 1185.5$ eV that was used for the measurements in Ch. 4 and the broadening of $\sigma = 2$ eV that we found earlier. The resolving power is $R = E/\sigma$. For a wavelength λ we obtain a resolution of $\Delta\lambda = \lambda/R$. Equivalently to Subsec. A we apply a Gaussian convolution to the optical coefficients, i.e. the real and imaginary part of the refractive index, with a Gaussian width of $\Delta\lambda$ this time. The result is shown in Fig. A.2. The real part of the refractive index is treated equivalently, but for X-ray energies is always almost 1 with some noise in the data. It is therefore not instructive to plot it.

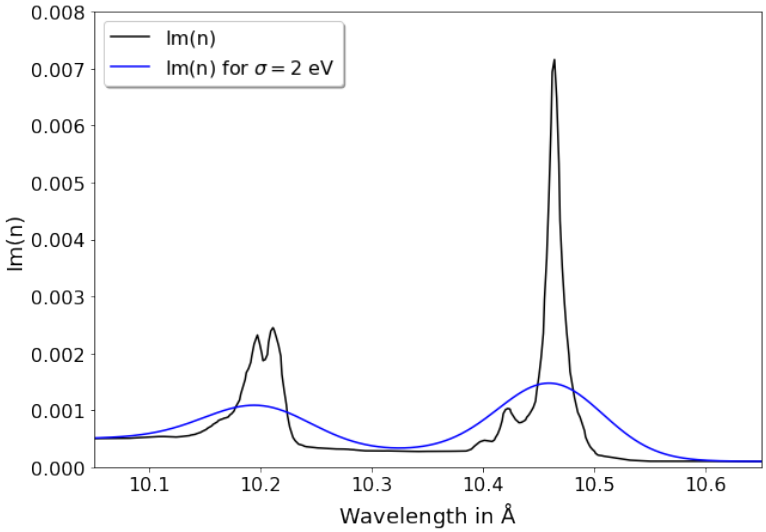

Figure A.2: *The tabulated imaginary part of the refractive index (black) as well as the convolution with a Gaussian function of width* $\sigma = 2$ ev.

Appendix B

Magnetization dynamics of 10 nm and 60 nm Gd films

In Ch. 4 we discussed the lack of an ultrafast timescale in a 60 nm Gd sample on a W(110) substrate as compared to a 10 nm Gd sample as investigated by Bobowski *et al.* [20]. Fig. 4.9 shows a comparison between the two experiments for an absorbed fluence of 7.4 mJ/cm^2 in the Gd/W sample. Here we present further comparisons for absorbed fluences of 3.9 mJ/cm^2 and 5.4 mJ/cm^2 in the Gd/W sample[1]. These data were presented in Bobowski's PhD thesis [91].

[1]Denoted as 3.6 mJ/cm^2 and 5.0 mJ/cm^2 in Ch. 4, referring to the absorbed fluence in Gd only.

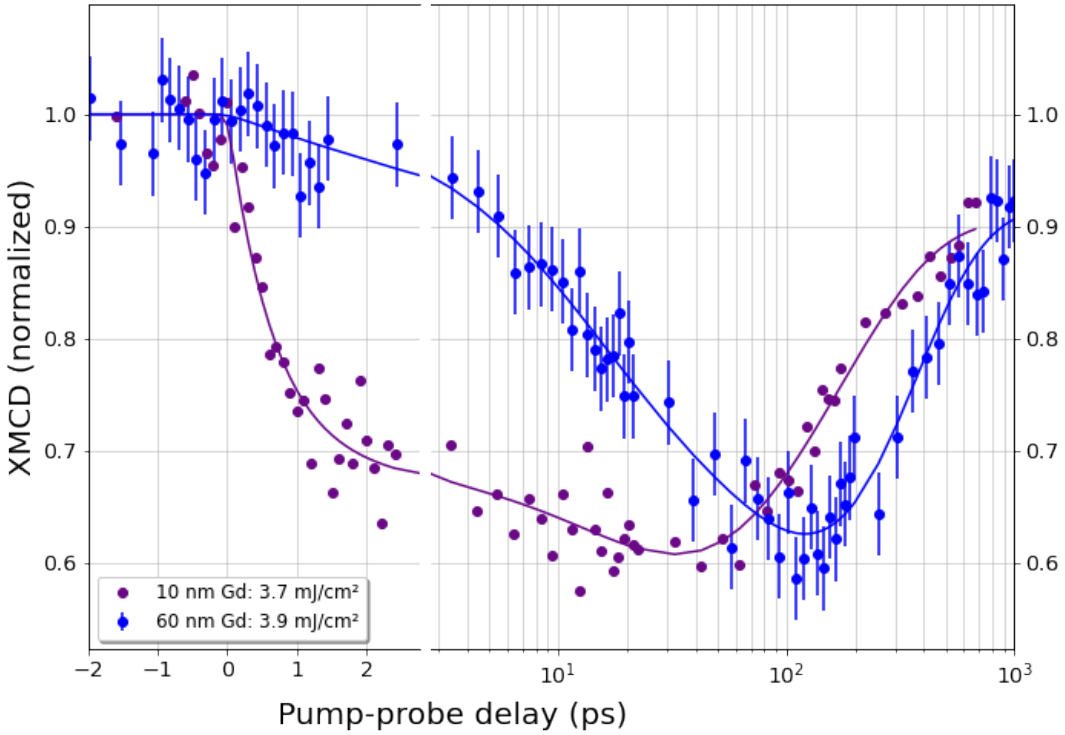

Figure B.1: *Comparison of the magnetization dynamics of our* 60 nm *Gd film with the* 10 nm *Gd film investigated by Bobowski et al. [20]. The latter was measured at the M_5 absorption edge at an energy of* 1186.3 eV*. The given fluences here are those absorbed in Gd and W for both layers. In Fig. 4.8 and Tab. 4.1 this is the* 3.6 mJ/cm^2 *dataset of the* 60 nm *film. Despite uncertainties in the comparability of the two fluence values, the maximum demagnetization levels are comparable and thus the total energy intake per probed volume of both films.*

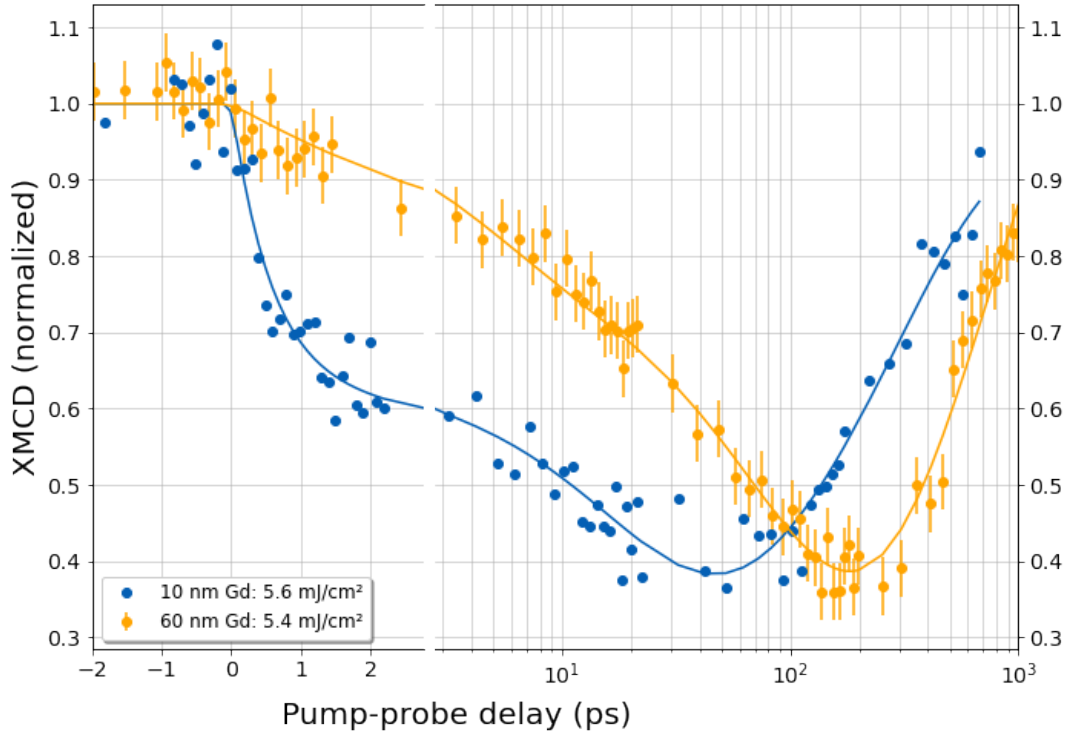

Figure B.2: *Comparison of the magnetization dynamics of our* 60 nm *Gd film with the* 10 nm *Gd film investigated by Bobowski et al. [20]. The latter was measured at the* M_5 *absorption edge at an energy of* 1186.3 eV*. The given fluences here are those absorbed in Gd and W for both layers. In Fig. 4.8 and Tab. 4.1 this is the* 5.0 mJ/cm^2 *dataset of the* 60 nm *film. Despite uncertainties in the comparability of the two fluence values, the maximum demagnetization levels are comparable and thus the total energy intake per probed volume of both films.*

Publications

[I] K. Bobowski, X. Zheng, B. Frietsch, D. Lawrenz, W. Bronsch, C. Gahl, B. Andres, C. Strüber, M. Weinelt, R. Carley, M. Teichmann, A. Scherz, S. Molodtsov, C. Cacho, R. Chapman and E. Springate *"Ultrafast interface spin transfer and its impact on the electronic structure"*, Sci. Adv. (2024) – **under review**.

[II] N. Thielemann-Kühn, D. Lawrenz, K. Bobowski, C. Krohn, M. Gleich, T. Amrhein, X. Zheng, W. Bronsch, U. Atxitia, N. Pontius, C. Schüssler-Langeheine and M. Weinelt *"The role of magnon driven spin currents in the magnetization dynamics of Gd"*, – **in preparation**.

[III] D. Lawrenz, T. Amrhein, N. Thielemann-Kühn, J. Weber, N. Pontius, C. Schüssler-Langeheine and M. Weinelt *"Interplay of magnetic structure and magnetization dynamics in the synthetic ferrimagnet Fe/Gd"*, – **in preparation**.

Bibliography

[1] E. Beaurepaire, J.-C. Merle, A. Daunois, and J.-Y. Bigot. "Ultrafast Spin Dynamics in Ferromagnetic Nickel". In: *Phys. Rev. Lett.* **76** (1996), 4250.
(Cit. on pp. 1, 4–6, 13, 18, 20.)

[2] B. Frietsch, J. Bowlan, R. Carley, M. Teichmann, S. Wienholdt, D. Hinzke, U. Nowak, K. Carva, P. M. Oppeneer, and M. Weinelt. "Disparate ultrafast dynamics of itinerant and localized magnetic moments in gadolinium metal". eng. In: *Nature communications* **6** (2015), 8262.
(Cit. on pp. 1, 4, 7, 11, 12, 49, 60, 62–64, 98, 103, 108, 133, 135.)

[3] S. Wienholdt, D. Hinzke, K. Carva, P. M. Oppeneer, and U. Nowak. "Orbital-resolved Spin Model for Thermal Magnetization Switching in Rare-earth-based Ferrimagnets". In: *Phys. Rev. B* **88** (2013), 020406.
(Cit. on pp. 1, 6, 11, 20, 21, 65.)

[4] R. Gómez-Abal and W. Hübner. "The Role of Spin orbit Coupling in Optically Induced Ultrafast Magnetic Dynamics". In: *Journal of Physics: Condensed Matter* **15** (2003), S709.
(Cit. on pp. 2, 13.)

[5] C. D. Stanciu, F. Hansteen, A. V. Kimel, A. Kirilyuk, A. Tsukamoto, A. Itoh, and T. Rasing. "All-optical Magnetic Recording with Circularly Polarized Light". In: *Phys. Rev. Lett.* **99** (2007), 047601.
(Cit. on pp. 2, 14.)

[6] M. L. M. Lalieu, M. J. G. Peeters, S. R. R. Haenen, R. Lavrijsen, and B. Koopmans. "Deterministic All-optical Switching of Synthetic Ferrimagnets using Single Femtosecond Laser Pulses". In: *Phys. Rev. B* **96** (2017), 220411.
(Cit. on pp. 2, 16, 21.)

[7] M. Beens, M. L. M. Lalieu, A. J. M. Deenen, R. A. Duine, and B. Koopmans. "Comparing All-optical Switching in Synthetic-ferrimagnetic Multilayers and Alloys". In: *Phys. Rev. B* **100** (2019), 220409.
(Cit. on pp. 2, 21, 64, 92, 100, 106–109, 113.)

[8] M. Beens, M. L. M. Lalieu, R. A. Duine, and B. Koopmans. "The role of intermixing in all-optical switching of synthetic-ferrimagnetic multilayers". In: *AIP Advances* **9** (2019), 125133.
(Cit. on pp. 2, 100, 106–108.)

[9] I. Radu, K. Vahaplar, C. Stamm, T. Kachel, N. Pontius, H. A. Dürr, T. A. Ostler, J. Barker, R. F. L. Evans, R. W. Chantrell, A. Tsukamoto, A. Itoh, A. Kirilyuk, T. Rasing, and A. V. Kimel. "Transient Ferromagnetic-like State mediating Ultrafast Reversal of Antiferromagnetically Coupled Spins". In: *Nature* **472** (2011), 205.
(Cit. on pp. 2, 15, 18, 92, 99, 100, 107, 109, 112, 113.)

[10] R. E. Camley and D. R. Tilley. "Phase transitions in magnetic superlattices". In: *Phys. Rev. B* **37** (1988), 3413.
(Cit. on pp. 2, 8–11, 68, 69, 72, 75, 85, 87, 89, 106, 108, 111, 133, 135.)

[11] R. E. Camley. "Properties of magnetic superlattices with antiferromagnetic interfacial coupling: Magnetization, susceptibility, and compensation points". In: *Phys. Rev. B* **39** (1989), 12316.
(Cit. on pp. 2, 8–11, 68, 75, 87, 90, 103, 111, 133, 135.)

[12] W. Lowrie. *Fundamentals of geophysics*. Cambridge: Cambridge Univ. Press, 2007.
(Cit. on p. 3.)

[13] K. Shinagawa. "Faraday and Kerr Effects in Ferromagnets". In: *Magneto-Optics*. Ed. by S. Sugano and N. Kojima. Berlin, Heidelberg: Springer Berlin Heidelberg, 2000, 137.
(Cit. on p. 4.)

[14] M. Hennecke, D. Schick, T. Sidiropoulos, F. Willems, A. Heilmann, M. Bock, L. Ehrentraut, D. Engel, P. Hessing, B. Pfau, M. Schmidbauer, A. Furchner, M. Schnuerer, C. von Korff Schmising, and S. Eisebitt. "Ultrafast element- and depth-resolved magnetization dynamics probed by transverse magneto-optical Kerr effect spectroscopy in the soft x-ray range". In: *Phys. Rev. Res.* **4** (2022), L022062.
(Cit. on p. 4.)

[15] J. Kirschner and R. Feder. "Spin Polarization in Double Diffraction of Low-Energy Electrons from W(001): Experiment and Theory". In: *Phys. Rev. Lett.* **42** (1979), 1008.
(Cit. on p. 4.)

[16] B. Andres, P. Weiss, M. Wietstruk, and M. Weinelt. "Spin-dependent lifetime and exchange splitting of surface states on Ni(1 1 1)". In: *Journal of Physics: Condensed Matter* **27** (2014), 015503.
(Cit. on p. 4.)

[17] A. Winkelmann, D. Hartung, H. Engelhard, C.-T. Chiang, and J. Kirschner. "High efficiency electron spin polarization analyzer based on exchange scattering at FeW(001)." eng. In: *The Review of scientific instruments* **79** (2008), 083303.
(Cit. on p. 4.)

[18] B. Andres, M. Weinelt, H. Ebert, J. Braun, A. Aperis, and P. Oppeneer. "Strong momentum-dependent electron-magnon renormalization of a surface resonance on iron". In: *Applied Physics Letters* **120** (2022), 202404.
(Cit. on p. 4.)

[19] J. Stöhr. "X-ray magnetic circular dichroism spectroscopy of transition metal thin films". In: *Journal of Electron Spectroscopy and Related Phenomena* **75** (1995). Future Perspectives for Electron Spectroscopy with Synchrotron Radiation, 253.
(Cit. on p. 4.)

[20] K. Bobowski, M. Gleich, N. Pontius, C. Schüßler-Langeheine, C. Trabant, M. Wietstruk, B. Frietsch, and M. Weinelt. "Influence of the pump pulse wavelength on the ultrafast demagnetization of Gd(0 0 0 1) thin films". In: *Journal of Physics: Condensed Matter* **29** (2017), 234003.
(Cit. on pp. 4, 7, 8, 49, 53, 57, 59, 61–64, 98, 103, 108, 111, 118–120, 133, 135.)

[21] I. A. Zaliznyak and S. H. Lee. *Magnetic Neutron Scattering*. Tech. rep. United States, 86.
(Cit. on p. 4.)

[22] M. W. Klein, C. Enkrich, M. Wegener, and S. Linden. "Second-Harmonic Generation from Magnetic Metamaterials". In: *Science* **313** (2006), 502.
(Cit. on p. 4.)

[23] A. Vaterlaus, D. Guarisco, M. Lutz, M. Aeschlimann, M. Stampanoni, and F. Meier. "Different spin and lattice temperatures observed by spin-polarized photoemission with picosecond laser pulses". In: *Journal of Applied Physics* **67** (1990), 5661.
(Cit. on p. 5.)

[24] A. Vaterlaus, T. Beutler, and F. Meier. "Spin-lattice relaxation time of ferromagnetic gadolinium determined with time-resolved spin-polarized photoemission". In: *Phys. Rev. Lett.* **67** (1991), 3314.
(Cit. on p. 5.)

[25] R. J. Elliott. "Theory of the Effect of Spin-Orbit Coupling on Magnetic Resonance in Some Semiconductors". In: *Phys. Rev.* **96** (1954), 266.
(Cit. on p. 5.)

[26] Y. Yafet. *g Factors and Spin-Lattice Relaxation of Conduction Electrons*. Vol. 14. Academic New York, 1963.
(Cit. on p. 5.)

[27] B. Koopmans, G. Malinowski, F. Dalla Longa, D. Steiauf, M. Fähnle, T. Roth, M. Cinchetti, and M. Aeschlimann. "Explaining the paradoxical diversity of ultrafast laser-induced demagnetization". In: *Nature Materials* **9** (2010), 259.
(Cit. on pp. 5, 8, 19.)

[28] M. Battiato, K. Carva, and P. M. Oppeneer. "Superdiffusive Spin Transport as a Mechanism of Ultrafast Demagnetization". In: *Phys. Rev. Lett.* **105** (2010), 027203.
(Cit. on p. 5.)

[29] K. Kimura. "Magnetic properties of iron: from clusters to bulk". In: *Physics Letters A* **158** (1991), 85.
(Cit. on p. 6.)

[30] H. C. S. J. Stöhr. *Magnetism: From Fundamentals to Nanoscale Dynamics*. Ed. by M. Cardona, P. Fulde, K. von Klitzing, R. Merlin, H.-J. Queisser, and H. Störmer. Springer, 2006.
(Cit. on pp. 6, 13, 28, 30, 36–40, 66, 71.)

[31] O. Haglund. "Curie temperature of alloys, its measurement and technical importance". In: *Journal of thermal analysis* **25** (1982), 21.
(Cit. on p. 6.)

[32] R. Gort, K. Bühlmann, S. Däster, G. Salvatella, N. Hartmann, Y. Zemp, S. Holenstein, C. Stieger, A. Fognini, T. U. Michlmayr, T. Bähler, A. Vaterlaus, and Y. Acremann. "Early Stages of Ultrafast Spin Dynamics in a 3*d* Ferromagnet". In: *Phys. Rev. Lett.* **121** (2018), 087206.
(Cit. on p. 6.)

[33] L. W. Roeland, G. J. Cock, F. A. Muller, A. C. Moleman, K. A. McEwen, R. G. Jordan, and D. W. Jones. "Conduction electron polarization of gadolinium metal". In: *Journal of Physics F: Metal Physics* **5** (1975), L233.
(Cit. on p. 6.)

[34] M. A. Ruderman and C. Kittel. "Indirect Exchange Coupling of Nuclear Magnetic Moments by Conduction Electrons". In: *Phys. Rev.* **96** (1954), 99.
(Cit. on p. 7.)

[35] T. Kasuya. "A Theory of Metallic Ferro- and Antiferromagnetism on Zener's Model". In: *Progress of Theoretical Physics* **16** (1956), 45.
(Cit. on p. 7.)

[36] K. Yosida. "Magnetic Properties of Cu-Mn Alloys". In: *Phys. Rev.* **106** (1957), 893.
(Cit. on p. 7.)

[37] H. E. Nigh, S. Legvold, and F. H. Spedding. "Magnetization and Electrical Resistivity of Gadolinium Single Crystals". In: *Phys. Rev.* **132** (1963), 1092.
(Cit. on p. 7.)

[38] M. Sultan, A. Melnikov, and U. Bovensiepen. "Ultrafast magnetization dynamics of Gd(0001): Bulk versus surface". In: *physica status solidi (b)* **248** (2011), 2323.
(Cit. on p. 7.)

[39] R. Carley, K. Döbrich, B. Frietsch, C. Gahl, M. Teichmann, O. Schwarzkopf, P. Wernet, and M. Weinelt. "Femtosecond Laser Excitation Drives Ferromagnetic Gadolinium out of Magnetic Equilibrium". In: *Phys. Rev. Lett.* **109** (2012), 057401.
(Cit. on p. 7.)

[40] M. Wietstruk, A. Melnikov, C. Stamm, T. Kachel, N. Pontius, M. Sultan, C. Gahl, M. Weinelt, H. A. Dürr, and U. Bovensiepen. "Hot-Electron-Driven Enhancement of Spin-Lattice Coupling in Gd and Tb $4f$ Ferromagnets Observed by Femtosecond X-Ray Magnetic Circular Dichroism". In: *Phys. Rev. Lett.* **106** (2011), 127401.
(Cit. on p. 8.)

[41] R. E. Camley. "Surface spin reorientation in thin Gd films on Fe in an applied magnetic field". In: *Phys. Rev. B* **35** (1987), 3608.
(Cit. on p. 8.)

[42] P. Bauer, M. Sajieddine, C. Dufour, K. Cherifi, G. Marchal, and P. Mangin. "Direct Evidence of the Twisted State in Ferrimagnet Gd/Fe Multilayers by Moessbauer Spectroscopy". In: *EPL* **16** (1991), 307.
(Cit. on pp. 8, 12.)

[43] C. Dufour, K. Cherifi, G. Marchal, P. Mangin, and M. Hennion. "Polarized neutron scattering from Gd/Fe multilayers: Twisted phase and spin-flip scattering". In: *Physical Review. B Condensed Matter* **47** (1993), 14572.
(Cit. on pp. 8, 12.)

[44] A. Drovosekov, A. Savitsky, D. Kholin, N. Kreines, V. Proglyado, M. Makarova, E. Kravtsov, and V. Ustinov. "Twisted magnetization states and inhomogeneous resonance modes in a Fe/Gd ferrimagnetic multilayer". In: *Journal of Magnetism and Magnetic Materials* **475** (2019), 668.
(Cit. on p. 12.)

[45] J. Hintermayr, A. Ullrich, and M. Albrecht. "Structure and magnetic properties of ferrimagnetic $(Gd/Fe)_n$ multilayer and Gd_xFe_{100-x} thin films". In: *AIP Advances* **11** (2021), 095214.
(Cit. on p. 12.)

[46] Y. Kamiguchi, Y. Hayakawa, and H. Fujimori. "Anomalous field dependence of magnetoresistance in Fe/Gd multilayered ferrimagnets". In: *Applied Physics Letters* **55** (1989), 1918.
(Cit. on p. 12.)

[47] H. Kiriake, F. Kato, M. Nawate, and S. Honda. "Magnetic Property of Gd/Fe Multilayers". In: *IEEE Translation Journal on Magnetics in Japan* **8** (1993), 537.
(Cit. on p. 12.)

[48] K. H. J. Buschow. "Intermetallic compounds of rare-earth and 3d transition metals". In: *Reports on Progress in Physics* **40** (1977), 1179.
(Cit. on p. 12.)

[49] R. Gómez-Abal, O. Ney, K. Satitkovitchai, and W. Hübner. "All-optical Subpicosecond Magnetic Switching in NiO(001)". In: *Phys. Rev. Lett.* **92** (2004), 227402.
(Cit. on p. 13.)

[50] K. Vahaplar, A. M. Kalashnikova, A. V. Kimel, D. Hinzke, U. Nowak, R. Chantrell, A. Tsukamoto, A. Itoh, A. Kirilyuk, and T. Rasing. "Ultrafast Path for Optical Magnetization Reversal via a Strongly Nonequilibrium State". In: *Phys. Rev. Lett.* **103** (2009), 117201.
(Cit. on pp. 14, 20.)

[51] A. R. Khorsand, M. Savoini, A. Kirilyuk, A. V. Kimel, A. Tsukamoto, A. Itoh, and T. Rasing. "Role of Magnetic Circular Dichroism in All-optical Magnetic Recording". In: *Phys. Rev. Lett.* **108** (2012), 127205.
(Cit. on p. 16.)

[52] T. A. Ostler et al. "Ultrafast Heating as a Sufficient Stimulus for Magnetization Reversal in a Ferrimagnet". In: *Nature Communications* **3** (2012), 666.
(Cit. on pp. 16, 18.)

[53] Y. L. W. van Hees, P. van de Meugheuvel, B. Koopmans, and R. Lavrijsen. "Deterministic All-optical Magnetization Writing facilitated by Non-local Transfer of Spin Angular Momentum". In: *Nature Communications* **11** (2020), 3835.
(Cit. on p. 16.)

[54] F. Cheng, Z. Du, X. Wang, Z. Cai, L. Li, C. Wang, A. Benabbas, P. Champion, N. Sun, L. Pan, and Y. Liu. "All-Optical Helicity-Dependent Switching in Hybrid Metal-Ferromagnet Thin Films". In: *Advanced Optical Materials* **8** (2020), 2000379.
(Cit. on p. 16.)

[55] C. E. Graves et al. "Nanoscale Spin Reversal by Non-local Angular Momentum Transfer following Ultrafast Laser Excitation in Ferrimagnetic GdFeCo". In: *Nature Materials* **12** (2013), 293.
(Cit. on pp. 16, 20.)

[56] F. Jakobs, T. A. Ostler, C.-H. Lambert, Y. Yang, S. Salahuddin, R. B. Wilson, J. Gorchon, J. Bokor, and U. Atxitia. "Unifying Femtosecond and Picosecond Single-pulse Magnetic Switching in Gd-Fe-Co". In: *Phys. Rev. B* **103** (2021), 104422.
(Cit. on p. 16.)

[57] W. A. Challener, C. Peng, A. V. Itagi, D. Karns, W. Peng, Y. Peng, X. Yang, X. Zhu, N. J. Gokemeijer, Y.-T. Hsia, G. Ju, R. E. Rottmayer, M. A.

Seigler, and E. C. Gage. "Heat-assisted Magnetic Recording by a Near-field Transducer with Efficient Optical Energy Transfer". In: *Nature Photonics* **3** (2009), 220.
(Cit. on p. 17.)

[58] T.-M. Liu, T. Wang, A. H. Reid, M. Savoini, X. Wu, B. Koene, P. Granitzka, C. E. Graves, D. J. Higley, Z. Chen, G. Razinskas, M. Hantschmann, A. Scherz, J. Stöhr, A. Tsukamoto, B. Hecht, A. V. Kimel, A. Kirilyuk, T. Rasing, and H. A. Dürr. "Nanoscale Confinement of All-Optical Magnetic Switching in TbFeCo - Competition with Nanoscale Heterogeneity". In: *Nano Lett.* **15** (2015), 6862.
(Cit. on p. 17.)

[59] L. Le Guyader, M. Savoini, S. El Moussaoui, M. Buzzi, A. Tsukamoto, A. Itoh, A. Kirilyuk, T. Rasing, A. V. Kimel, and F. Nolting. "Nanoscale sub-100 picosecond all-optical magnetization switching in GdFeCo microstructures". In: *Nature Communications* **6** (2015), 5839.
(Cit. on p. 17.)

[60] R. F. L. Evans, R. W. Chantrell, U. Nowak, A. Lyberatos, and H. Richter. "Thermally induced error: Density limit for magnetic data storage". In: *Applied Physics Letters* **100** (2012), 102402.
(Cit. on p. 17.)

[61] R. F. L. Evans, T. A. Ostler, R. W. Chantrell, I. Radu, and T. Rasing. "Ultrafast thermally induced magnetic switching in synthetic ferrimagnets". In: *Applied Physics Letters* **104** (2014), 082410.
(Cit. on p. 17.)

[62] J. H. Mentink, J. Hellsvik, D. V. Afanasiev, B. A. Ivanov, A. Kirilyuk, A. V. Kimel, O. Eriksson, M. I. Katsnelson, and T. Rasing. "Ultrafast Spin Dynamics in Multisublattice Magnets". In: *Phys. Rev. Lett.* **108** (2012), 057202.
(Cit. on p. 18.)

[63] U. Atxitia, P. Nieves, and O. Chubykalo-Fesenko. "Landau-Lifshitz-Bloch equation for ferrimagnetic materials". In: *Phys. Rev. B* **86** (2012), 104414.
(Cit. on pp. 19, 64.)

[64] U. Atxitia, T. Ostler, J. Barker, R. F. L. Evans, R. W. Chantrell, and O. Chubykalo-Fesenko. "Ultrafast Dynamical Path for the Switching of a Ferrimagnet After Femtosecond Heating". In: *Phys. Rev. B* **87** (2013), 224417.
(Cit. on p. 19.)

[65] A. J. Schellekens and B. Koopmans. "Microscopic Model for Ultrafast Magnetization Dynamics of Multisublattice Magnets". In: *Phys. Rev. B* **87** (2013), 020407.
(Cit. on pp. 19–21, 64.)

[66] S. Gerlach, L. Oroszlany, D. Hinzke, S. Sievering, S. Wienholdt, L. Szunyogh, and U. Nowak. "Modeling ultrafast all-optical switching in synthetic ferrimagnets". In: *Phys. Rev. B* **95** (2017), 224435.
(Cit. on pp. 20, 21, 64.)

[67] F. R. Elder, A. M. Gurewitsch, R. V. Langmuir, and H. C. Pollock. "Radiation from Electrons in a Synchrotron". In: *Physical Review* **71** (1947), 829.
(Cit. on p. 24.)

[68] T. Kachel. "The PM3 beamline at BESSY". In: *Journal of large-scale research facilities* (2016).
(Cit. on pp. 24, 25.)

[69] T. Kachel, F. Eggenstein, and R. Follath. "A soft X-ray plane-grating monochromator optimized for elliptical dipole radiation from modern sources." eng. In: *Journal of synchrotron radiation* **22** (2015), 1301.
(Cit. on p. 24.)

[70] A. A. Zholents and M. S. Zolotorev. "Femtosecond X-Ray Pulses of Synchrotron Radiation". In: *Phys. Rev. Lett.* **76** (1996), 912.
(Cit. on p. 25.)

[71] K. Holldack et al. "FemtoSpeX: a versatile optical pump-soft X ray probe facility with 100 fs X-ray pulses of variable polarization." eng. In: *Journal of synchrotron radiation* **21** (2014), 1090.
(Cit. on pp. 25–27.)

[72] S. Khan, K. Holldack, T. Kachel, R. Mitzner, and T. Quast. "Femtosecond Undulator Radiation from Sliced Electron Bunches". In: *Phys. Rev. Lett.* **97** (2006), 074801.
(Cit. on p. 26.)

[73] S. W. Lovesey and S. P. Collins. *X-Ray scattering and Absorption by Magnetic Materials*. Ed. by J. Chikawa, J. R. Helliwell, and S. W. Lovesey. Clarendon Press Oxford, 1996.
(Cit. on p. 28.)

[74] H.-J. Eichler, M. Freyberger, H. Fuchs, F. Haug, H. Kaase, J. Kross, H. Lang, H. Lichte, H. Niedrig, T. Pfau, H. Rauch, W. P. Schleich, G. Schmahl, E. Sedlmayr, F. Serick, K. Vogel, H. Weber, and K. Weber. *Bergmann Schaefer: Lehrbuch der Experimentalphysik Band 3, Optik: Wellen- und Teilchenoptik*. Ed. by H. Niedrig. Vol. 10. Walter de Gruyten, 2004.
(Cit. on p. 29.)

[75] S. Blügel, M. Giesen, B. Hillebrands, H. Hillmer, H. Ibach, R. Kassing, H. von LÃ¶hneysen, P. Luger, J. Salbeck, U. Scherz, W. Schilling, and L. K. Thomas. *Bergmann Schaefer: Lehrbuch der Experimentalphysik - Festkörper*. Vol. 2. Walter de Gruyter, Rainer Kassing, 2005.
(Cit. on p. 29.)

[76] B. L. Henke, E. M. Gullikson, and J. C. Davis. "X-Ray Interactions: Photoabsorption, Scattering, Transmission, and Reflection at E = 50-30,000 eV, Z = 1-92". In: *Atomic Data and Nuclear Data Tables* **54** (1993), 181.
(Cit. on p. 30.)

[77] C. T. Chantler, K. Olsen, R. A. Dragoset, J. Chang, A. R. Kishore, S. A. Kotochigova, and D. S. Zucker. *NIST Standard Reference Database 66*. 2005.
(Cit. on pp. 30, 36, 41.)

[78] J. Als-Nielsen and D. McMorrow. *Elements of Modern X-Ray Physics*. 2nd ed. Wiley, 2011.
(Cit. on pp. 31, 32.)

[79] D. Windt. "IMD - Software for modeling the optical properties of multilayer films". In: *Computers in Physics* **12** (1998), 360.
(Cit. on pp. 33, 54, 94.)

[80] O. S. Heavens. *Optical properties of thin solid films*. New York: Dover Publications, 1991.
(Cit. on pp. 34–36.)

[81] M. Elzo, E. Jal, O. Bunau, S. Grenier, A. Y. Ramos, H. Tolentino, Y. Joly, J.-M. Tonnerre, and N. Jaouen. "X-ray Resonant Magnetic Reflectivity of Stratified Magnetic Structures: Eigenwave Formalism and Application to a W/Fe/W Trilayer". In: *Journal of Magnetism and Magnetic Materials* **324** (2012), 105.
(Cit. on p. 41.)

[82] S. Nepijko, M. Getzlaff, R. Pascal, C. Zarnitz, M. Bode, and R. Wiesendanger. "Lattice relaxation of Gd on W(110)". In: *Surface Science* **466** (2000), 89.
(Cit. on pp. 43, 44.)

[83] M. R. Andrews. "Diffusion of Carbon through Tungsten and Tungsten Carbide". In: *J. Phys. Chem.* **29** (1925), 462.
(Cit. on p. 43.)

[84] B. Andres. *Spin and Magnetization Dynamics Studied by Spin-Resolved Photoemission*. PhD Thesis. 2016.
(Cit. on pp. 44, 61.)

[85] R. Cortenraad, S. N. Ermolov, A. W. Denier van der Gon, V. G. Glebovskii, H. H. Brongersma, A. Manenschijn, G. Gartner, and E. V. Belozerov. "Cleaning Procedure for Single-Crystal Tungsten Substrates". In: *Inorganic Materials* **37** (2001), 673.
(Cit. on p. 44.)

[86] K. Zakeri, T. Peixoto, Y. Zhang, J. Prokop, and J. Kirschner. "On the preparation of clean tungsten single crystals". In: *Surface Science* **604**

(2010), L1.
(Cit. on p. 44.)

[87] A. Aspelmeier, F. Gerhardter, and K. Baberschke. "Magnetism and structure of ultrathin Gd films". In: *Journal of Magnetism and Magnetic Materials* **132** (1994), 22.
(Cit. on p. 45.)

[88] M. S. del Río and R. J. Dejus. "XOP v2.4: recent developments of the x-ray optics software toolkit". In: *Advances in Computational Methods for X-Ray Optics II*. Ed. by M. S. del Rio and O. Chubar. Vol. 8141. International Society for Optics and Photonics. SPIE, 2011, 814115.
(Cit. on p. 54.)

[89] S. Adachi. *The handbook on optical constants of metals*. World Scientific Publishing Co. Pte. Ltd., 2012.
(Cit. on pp. 54, 94.)

[90] A. Khorsand, M. Savoini, A. Kirilyuk, and T. Rasing. "Optical excitation of thin magnetic layers in multilayer structures." In: *Nature materials* **13(2)** (2014), 101.
(Cit. on pp. 54, 94.)

[91] K. Bobowski. *Magnetization Dynamics in the Lanthanide Metal Gadolinium*. PhD Thesis.
(Cit. on pp. 59, 118.)

[92] B. Frietsch, A. Donges, R. Carley, M. Teichmann, J. Bowlan, K. Döbrich, K. Carva, D. Legut, P. M. Oppeneer, U. Nowak, and M. Weinelt. "The role of ultrafast magnon generation in the magnetization dynamics of rare-earth metals". In: *Science Advances* **6** (2020), eabb1601.
(Cit. on p. 61.)

[93] N. Thielemann-KÃ¼hn et al. "Optical control of 4f orbital state in rare-earth metals". In: *Science Advances* **10** (2024), eadk9522.
(Cit. on p. 61.)

[94] J. Jensen and A. R. Mackintosh. *Rare Earth Magnetism*. Ed. by J. Birman, S. F. Edwards, C. H. Llewellyn Smith, and M. Rees. Clarendon Press Oxford, 1991.
(Cit. on p. 62.)

[95] T. A. Ostler, R. F. L. Evans, R. W. Chantrell, U. Atxitia, O. Chubykalo-Fesenko, I. Radu, R. Abrudan, F. Radu, A. Tsukamoto, A. Itoh, A. Kirilyuk, T. Rasing, and A. Kimel. "Crystallographically amorphous ferrimagnetic alloys: Comparing a localized atomistic spin model with experiments". In: *Phys. Rev. B* **84** (2011), 024407.
(Cit. on p. 64.)

[96] J. Barker, U. Atxitia, T. A. Ostler, O. Hovorka, O. Chubykalo-Fesenko, and R. W. Chantrell. "Two-magnon bound state causes ultrafast thermally

induced magnetisation switching". In: *Scientific Reports* **3** (2013), 3262.
(Cit. on p. 64.)

[97] S. Blundell. *Magnetism in Condensed Matter*. Oxford University Press, 2001.
(Cit. on pp. 65, 66.)

[98] M. Taborelli, R. Allenspach, G. Boffa, and M. Landolt. "Magnetic coupling of surface adlayers: Gd on Fe(100)". In: *Phys. Rev. Lett.* **56** (1986), 2869.
(Cit. on pp. 67, 85, 111.)

[99] N. Ishimatsu, H. Hashizume, S. Hamada, N. Hosoito, C. S. Nelson, C. T. Venkataraman, G. Srajer, and J. C. Lang. "Magnetic structure of Fe/Gd multilayers determined by resonant x-ray magnetic scattering". In: *Phys. Rev. B* **60** (1999), 9596.
(Cit. on pp. 67, 85, 111.)

[100] D. Haskel, G. Srajer, J. C. Lang, J. Pollmann, C. S. Nelson, J. S. Jiang, and S. D. Bader. "Enhanced Interfacial Magnetic Coupling of Gd/Fe Multilayers". In: *Phys. Rev. Lett.* **87** (2001), 207201.
(Cit. on pp. 67, 71, 73, 85, 99, 111.)

[101] Y. Choi, D. Haskel, R. E. Camley, D. R. Lee, J. C. Lang, G. Srajer, J. S. Jiang, and S. D. Bader. "Temperature evolution of the Gd magnetization profile in strongly coupled Gd/Fe multilayers". In: *Phys. Rev. B* **70** (2004), 134420.
(Cit. on pp. 67, 85, 111.)

[102] J. E. Prieto, F. Heigl, O. Krupin, G. Kaindl, and K. Starke. "Magneto-optics of Gd and Tb in the soft x-ray resonance regions". In: *Phys. Rev. B* **68** (2003), 134453.
(Cit. on pp. 79, 84, 88.)

[103] C. T. Chen, Y. U. Idzerda, H.-J. Lin, N. V. Smith, G. Meigs, E. Chaban, G. H. Ho, E. Pellegrin, and F. Sette. "Experimental Confirmation of the X-Ray Magnetic Circular Dichroism Sum Rules for Iron and Cobalt". In: *Phys. Rev. Lett.* **75** (1995), 152.
(Cit. on p. 79.)

[104] E. Carpene, E. Mancini, C. Dallera, M. Brenna, E. Puppin, and S. De Silvestri. "Dynamics of electron-magnon interaction and ultrafast demagnetization in thin iron films". In: *Phys. Rev. B* **78** (2008), 174422.
(Cit. on pp. 99, 100, 103, 108.)

[105] B. A. Ivanov. "Spin Dynamics for Antiferromagnets and Ultrafast Spintronics". In: *Journal of Experimental and Theoretical Physics* **131** (2020), 95.
(Cit. on p. 99.)

Appendix C

Deutsche Kurzfassung

Diese Arbeit befasst sich mit der ultraschnellen Magnetisierungsdynamik in Seltenerd- und Übergangsmetallen. Im ersten Teil untersuchten wir mittels XMCD in Reflexion die Magnetisierungsdynamik von 60 nm Gd(0001) auf W(110). Unsere Analyse zeigt, dass die ultraschnelle Zeitskala der Entmagnetisierung, die von früheren Autoren in 10 nm dicken Gd-Schichten [2, 20] gefunden wurde, auf Effekte an der Gd/W-Grenzfläche zurückzuführen ist, die wir als magnonengetriebene Spinströme interpretieren.
Im zweiten Teil der Arbeit wandten wir sowohl XRMR als auch XMCD in Reflexion an, um die magnetische Struktur des synthetischen Ferrimagneten Fe/Gd, gewachsen auf W(110), zu untersuchen. Wir finden deutliche Anzeichen für einen verdrehten Magnetisierungszustand, wie er von Camley und Tilley [10, 11] vorhergesagt wird. In diesem Zustand bilden beide Schichten eine domänenwandartige Struktur, wobei die magnetischen Momente fast senkrecht zum Feld an der Fe/Gd-Grenzfläche ausgerichtet sind und sich in beiden Schichten schrittweise in Richtung Feldausrichtung neigen.
Wir finden weiterhin sehr unterschiedliche Magnetisierungsdynamiken in XMCD in Reflexion, die von einem Anstieg der detektierten Magnetisierungskomponente auf einer langsamen ps-Zeitskala bis hin zu einem rein optischen Umschalten der Gd-Komponente innerhalb von weniger als 1 ps reichen. Die Unterschiede werden durch die temperaturabhängige Magnetisierungsorientierung im verdrehten Zustand verursacht. Da diese Orientierung ebenfalls durch die äußere Magnetfeldstärke manipuliert werden kann, bieten synthetische Ferrimagnete eine herausragende Kontrollierbarkeit ihrer Magnetisierungsdynamik.

Appendix D

Abstract

This work is concerned with the ultrafast magnetization dynamics found in rare-earth and transition metals. In the first part, we have investigated the magnetization dynamics of 60 nm Gd(0001) grown on W(110) in XMCD in reflection. Our analysis shows that the ultrafast timescale of demagnetization, which was found by previous authors in 10 nm thick Gd films [2, 20] can be attributed to effects at the Gd/W interface, which we interpret as magnon driven spin currents.
In the second part of the work, we have applied both XRMR and XMCD in reflection to study the magnetic structure of the synthetic ferrimagnet Fe/Gd grown on W(110). We find clear signs of a twisted magnetization state, as proposed by Camley and Tilley [10, 11] in which both layers form a domain-wall-like structure with the magnetic moments being aligned almost perpendicular to the field at the Fe/Gd interface and tilting stepwise towards field-aligned throughout both layers. We further find very diverse magnetization dynamics in XMCD in reflection, ranging from an increase of the detected magnetization component on a slow ps-timescale to all-optical switching of only the Gd component within less than 1 ps. The differences are caused by the temperature dependent orientation of the magnetization in the twisted state. As it can likewise be manipulated by the external magnetic field strength, synthetic ferrimagnets offer a great amount of controllability of their magnetization dynamics.

Appendix E

Selbstständigkeitserklärung

Ich erkläre gegenüber der Freien Universität Berlin, dass ich die vorliegende Dissertation selbstständig und ohne Benutzung anderer als der angegebenen Quellen und Hilfsmittel angefertigt habe. Die vorliegende Arbeit ist frei von Plagiaten. Alle Ausführungen, die wörtlich oder inhaltlich aus anderen Schriften entnommen sind, habe ich als solche kenntlich gemacht. Diese Dissertation wurde in gleicher oder ähnlicher Form noch in keinem früheren Promotionsverfahren eingereicht.
Mit einer Prüfung meiner Arbeit durch ein Plagiatsprüfungsprogramm erkläre ich mich einverstanden.

Datum: 28.03.2024
Dominic Lawrenz

Appendix F

Danksagung

Ich danke Prof. Dr. Martin Weinelt dafür, dass er mich in seine Arbeitsgruppe aufgenommen und mir somit die Möglichkeit zur Anfertigung einer Doktorarbeit gegeben hat. Darüber hinaus nahm er an Messzeiten teil, führte Korrekturlesungen durch und unterstützte mich durch seine wissenschaftliche Expertise mit wertvollem Input und Diskussionen, die erst zur jetzigen Form der physikalischen Interpretationen geführt haben. Ich danke Martin Weinelt auch für seine freundliche, geduldige und respektvolle Art und sein kulinarisches Gespür, von dem ich bei vielen Gruppenaktivitäten profitieren konnte.
Ich danke außerdem den zahlreichen Kollegen, die nicht nur in ebenso zahlreichen Messzeiten und Laboreinsätzen an meiner Seite standen, sondern auch durch hilfreiche Diskussionen sowie menschlich und privat. Als da wären: Kamil Bobowski, Markus Gleich, Jonathan Weber, Jan Böhnke, Xinwei Zheng, Robert Carley, Martin Teichmann, Daniel Przyrembel und Björn Frietsch. Durch diese Menschen war die AG Weinelt für mich wie eine zweite Familie.
Wibke Bronsch, Cornelius Gahl, Tim Amrhein und Nele Thielemann-Kühn gehören ebenfalls in diese Liste. Ich möchte ihnen aber gesondert danken, weil sie durch Korrekturlesungen, technische Ratschläge und wissenschaftliche Diskussionen auch zum unmittelbaren Entstehen der Dissertation beigetragen haben.
Die experimentellen Daten wären niemals zustande gekommen ohne die tatkräftige Unterstützung von Christian Schüssler-Langeheine und Niko Pontius vom BESSY II. Auch lange nach Feierabend und mitunter selbst mitten in der Nacht konnte man auf ihre Hilfe setzen. Auch an den wissenschaftlichen Diskussionen der Ergebnisse waren sie stets mit Interesse und wertvollem Input beteiligt. Jeder Nutzer kann sich über solche Betreuung glücklich schätzen.
Am allermeisten danke ich Beatrice Andres. Trotzdem die Fertigstellung dieser Arbeit deutlich länger gedauert hat, als zunächst gedacht, stand sie immer unbeirrt hinter mir. Sie hielt mir den Rücken frei, nahm das gros der familiären Lasten auf sich um mir diesen Schritt zu ermöglichen und führte nebenbei auch noch Korrekturlesungen durch. Und das über mehrere Jahre hinweg, auch während der Coronapandemie und trotz eigener, hoher Arbeitsbelastung. Sie hat einen Orden verdient.